Electrodeposition of Alkali Group I Metals from Room Temperature Ionic Liquids

Rahmat Wibowo

St. John's College

University of Oxford

DPhil Thesis

Trinity Term 2011

Physical and Theoretical Chemistry Laboratory

Electrodeposition of Alkali Group I Metals from Room Temperature Ionic Liquids

A Thesis Submitted for the Degree of DPhil in Physical and Theoretical Chemistry

by Rahmat Wibowo
St. John's College, University of Oxford
Trinity Term 2011

The work presented in this thesis involves the utility of room temperature ionic liquids (RTILs) as solvents in electrodeposition of Alkali Group I metals (excluding Fr). The first two chapters present fundamentals of electrochemistry which is the basis of this work followed by an overview of RTILs and a brief introduction to X-ray photoelectron spectroscopy. The results of five original studies are then presented as follows:

- The deposition and stripping of Li/Li^+ couple in several RTILs is studied in detail on Pt and Ni microelectrodes and the results are simulated using a mathematical model developed by the Compton Group
- The study is then continued for Na/Na^+ in several ionic liquids on a Ni microelectrode and the results are compared to that of Li/Li^+ couple
- The remaining members down the Group (K/K^+, Rb/Rb^+ and Cs/Cs^+) are studied in ionic liquid *N*-butyl-*N*-methyl-pyrrolidinium bis(trifluoromethylsulfonyl)imide ($[C_4mpyrr][NTf_2]$) on a Ni microelectrode allowing comparison of electrode potentials throughout Group in the IL to be deduced.
- The novel development of *in situ* electrochemical-X-ray photoelectron spectroscopy for monitoring the potassium deposition is reported
- Electrochemical-XPS is used for monitoring rubidium deposition in competition with RTIL solvent breakdown

The results presented show that several RTILs are able to support the electrodeposition of Alkali Group I metals due to their wide electrochemical windows and electrochemical stability. The simulation of the results allows thermodynamic and kinetic parameters such as the electrochemical rate constant (k^0), diffusion coefficient (D), and formal potential (E_f^0) and transfer coefficient (α) to be extracted. The trend in electrode potentials of the Group in $[C_4mpyrr][NTf_2]$ is also presented and compared to that of in other solvents. The near zero vapour pressure property of the RTILs is also exploited for the development of *in situ* electrochemical-XPS; a new branch of spectroelectrochemistry.

Acknowledgements

AlhamduliLlahi Rabbil ‘Alamiin.

First and foremost, I would like to thank Professor Richard G. Compton for having me to work in his research group for three years in my DPhil study. It has been a pleasure to work with such a motivating supervisor. I believe ‘his treatment’ during the process will influence my academic career as well as my life in general.

I would also like thank to Dr. Leigh Aldous; a ‘shadowed supervisor’ who gives me valuable knowledge in the world of room temperature ionic liquids and practical electrochemistry. To Robert Jacobs at Chemistry Research Laboratory for training me to use XPS and giving me some advices for the cell design. To Mr. C. Jones at the Student workshop for helping me constructing the cell for XPS measurements

I would also like to thank the Compton Group members 2008-2011 for all their help in research as well as friendship during my studies. Particularly to: Neil V Rees, Barbara Kozub, Ian Cutress, Edmund Dickinson, Christopher Batchelor, Stephen Belding, Sven Ernst, Yao Meng and Chaopeng Fu.

I would like to thank to my family especially my son Harits, my daughters Sawsan and Tsurayya. To my parents, I would like to say thank you for taking care of your beloved grandchildren.

Finally, I would like to thank The Directorate of Higher Education The Ministry of National Education and Universitas Indonesia for funding.

Contents

List of Publications

The results presented in Chapter 4 to 7 and Chapter 8 of this thesis have been published and accepted respectively in the following journals:

1. Wibowo, R., Ward-Jones, S. E., Compton, R. G., *Journal of Physical Chemistry B* **2009**, 113 (36), pp. 12293-12298
2. Wibowo, R., Ward-Jones, S. E., Compton, R. G., *Journal of Chemical and Engineering Data* **2010**, 55 (3), pp. 1374-1376
3. Wibowo, R., Aldous, L., Rogers, E.I., Ward-Jones, S. E., Compton, R. G., *Journal of Physical Chemistry C* **2010**, 114 (8), pp. 3618-3626
4. Wibowo, R., Aldous, L., Ward-Jones, S. E., Compton, R. G., *Chemical Physics Letters* **2010**, 492 (4-6), pp. 276-280
5. Wibowo, R., Aldous, L., Ward-Jones, S. E., Compton, R. G., *ECS Transaction* **2010**, 33 (7), pp. 523-535
6. Wibowo, R., Aldous, L., Jacobs, R. M. J., Manan, N. S. A., Compton, R. G., *Chemical Physics Letters* **2011**, 509 (1-3), pp. 72-76
7. Wibowo, R., Aldous, L., Jacobs, R. M. J., Manan, N. S. A., Compton, R. G., *Chemical Physics Letters*, **accepted**.

Chapter 1

Introduction: Fundamentals of Electrochemistry

In this chapter, fundamentals of electrochemistry, the basis of the work in this thesis are presented. This chapter discusses the basics of equilibrium electrochemistry, the processes in dynamic electrochemistry, microelectrodes and overviews of the simulation of metal deposition and stripping processes.

1.1 Equilibrium Electrochemistry

1.1.1 Electrode Potential

In order to understand the potential developed at the metal/solution interface, consider the processes happening when a metal (M) is inserted in the solution containing a metal ion (M^+). As the metal functions as an 'electron source or sink' the equilibrium below is established at the metal/solution interface:

$$M^+(s) + e^- \rightleftharpoons M(m) \tag{1.1}$$

At equilibrium, the reactants and products must have identical chemical potentials, so that

$$\begin{aligned} &\tilde{A}\text{f}\text{Æ}'\tilde{A} \dagger \hat{a}\text{€}^{\text{™}}\tilde{A}\text{f}\hat{a}\text{€}\text{¦}\tilde{A},\hat{A}\text{½}\tilde{A}\text{f}\text{Æ}'\tilde{A}\text{¢}\hat{a},\neg\text{Å}\text{¡}\tilde{A}\text{f}\hat{a}\text{€}\check{\text{S}}\tilde{A},\hat{A}\text{¼}_{M^+} \\ &+ \tilde{A}\text{f}\text{Æ}'\tilde{A} \dagger \hat{a}\text{€}^{\text{™}}\tilde{A}\text{f}\hat{a}\text{€}\text{¦}\tilde{A},\hat{A}\text{½}\tilde{A}\text{f}\text{Æ}'\tilde{A}\text{¢}\hat{a},\neg\text{Å}\text{¡}\tilde{A}\text{f}\hat{a}\text{€}\check{\text{S}}\tilde{A},\hat{A}\text{¼}_{e^-} \\ &= \tilde{A}\text{f}\text{Æ}'\tilde{A} \dagger \hat{a}\text{€}^{\text{™}}\tilde{A}\text{f}\hat{a}\text{€}\text{¦}\tilde{A},\hat{A}\text{½}\tilde{A}\text{f}\text{Æ}'\tilde{A}\text{¢}\hat{a},\neg\text{Å}\text{¡}\tilde{A}\text{f}\hat{a}\text{€}\check{\text{S}}\tilde{A},\hat{A}\text{¼}_{M} \end{aligned} \tag{1.2}$$

For the electrochemical process, the electrochemical potential of a species i would be the sum of both chemical and electrical energies:

$$\begin{aligned} &\overline{\tilde{A}\text{f}\text{Æ}'\tilde{A}\ldots\hat{A}\text{½}\tilde{A}\text{f}\hat{a}\text{€}\check{\text{S}}\tilde{A},\hat{A}\text{¼}_i} \\ &= \tilde{A}\text{f}\text{Æ}'\tilde{A}\ldots\hat{A}\text{½}\tilde{A}\text{f}\hat{a}\text{€}\check{\text{S}}\tilde{A},\hat{A}\text{¼}_i + z_i F\tilde{A}\text{f}\text{Æ}'\tilde{A},\hat{A}\ \ \tilde{A}\text{f}\hat{A}\text{¢}\tilde{A}\text{¢}\hat{a}\text{€}\check{\text{S}}\hat{A}\neg\tilde{A},\hat{A}\text{¢} \end{aligned} \tag{1.3}$$

The chemical energy (potential) can be defined as

$$\tilde{A}\check{\text{Z}}\hat{A}\text{¼}_i = \tilde{A}\check{\text{Z}}\hat{A}\text{¼}^0 + RTlna_i \tag{1.4}$$

so that the electrochemical potential consists of standard chemical potential, activity, a_i, and phase potential (electrode-solution interface), ϕ, according to the following equation:

$$\overline{\mu_i} = \mu^0 + RTlna_i + z_iF\phi \qquad (1.5)$$

where R is the universal gas constant (8.314 J mol^{-1} K^{-1}), T is temperature in K and F is Faraday constant (96485 C mol^{-1}). For all the species in equation 1.1, the electrochemical potentials are:

ÃƒÆ'Ã † â€™Ãƒâ€¦Ã‚½ÃƒÆ'Ã¢â‚¬Å¡Ãƒâ€šÃ‚¼$_{M^+}$ = ÃƒÆ'Ã

$+ RTlna_{M^+} + F$

ÃƒÆ'Ã † â€™Ãƒâ€šÃ‚ ÃƒÆ'Ã‚¢ÃƒÂ¢Ã¢â‚¬Å¡Ã‚¬Ãƒâ€šÃ‚

$\hat{I}\grave{1}\!\!\!/_{e^-} = \hat{I}1\!\!\!/_{e^-}^{0} - F\ddot{I}\bullet_m$

ÃƒÆ'Ã † â€™Ãƒâ€¦Ã‚½ÃƒÆ'Ã¢â‚¬Å¡Ãƒâ€šÃ‚¼$_M$ = ÃƒÆ'Ã †

At equilibrium, the total electrochemical potential of reactants is equal to that of the products, therefore:

$$\hat{I}1\!\!\!/_{M^+}^{0} + RTln\, a_{M^+} + F\ddot{I}\bullet_s + \hat{I}1\!\!\!/_{e^-}^{0} - F\ddot{I}\bullet_m = \hat{I}1\!\!\!/_M^0 \qquad (1.9)$$

Rearrangement of this equation leads to the equation for the difference between the potential of the metal phase, $\ddot{I}\bullet_m$, and the potential of the solution phase, $\ddot{I}\bullet_s$,

$$\Delta\phi = \phi_m - \phi_s = \frac{1}{F}\left(\mu_{M^+}^{0} + \mu_{e^-}^{0} - \mu_M^0\right) + \frac{RT}{F}lna_{M^+} \qquad (1.10)$$

The first term in the equation is the standard potential difference, $\hat{I}''\ddot{I}\bullet^0$, so that the equation can be rewritten as

$$\Delta\phi = \Delta\phi^0 + \frac{RT}{F}ln\,a_{M^+} \qquad (1.11)$$

Equation 1.11 is known as Nernst equation which relates the equilibrium potential to the activities of the species present. The general Nernst equation uses *E* for the potential difference in a cell containing two electrodes rather than $\Delta\phi$ because it cannot be measured directly. So the Nernst equation for the general reaction $O + e^- \tilde{A}f\text{Æ}'\tilde{A},\hat{A}\cent\tilde{A}f\hat{A}\cent\tilde{A}\cent\hat{a}\euro\check{s}\hat{A}\neg\tilde{A},\hat{A}\textexclamdown\tilde{A}f\hat{a}\euro\textexclamdown\tilde{A}\cent\hat{a},\neg\hat{a},\cent R$ would be

$$E = E^0 + \frac{RT}{F} ln\left(\frac{a_O}{a_R}\right) \tag{1.12}$$

where both O and R are solution phase species.

The Nernst equation relates changes in Gibbs energy. For the one electron transfer reaction above, the associated Gibbs energy change can be expressed as

$$\Delta G = - nFE \tag{1.13}$$

and

$$\Delta G = \Delta G^0 + RT ln \frac{a_R}{a_O} \tag{1.14}$$

In practice, the concentration of the electroactive species is often used rather than its activity because in electrolysis the current is proportional to the concentration and not activity. Therefore the term formal potential, E_f^0 , is introduced to relate the potential to the concentration

$$E = E_f^0 + \frac{RT}{F} ln \frac{[O]}{[R]} \tag{1.15}$$

Considering the relation between activity, *a*, and concentration, *c*, in equation

$$a = \tilde{I}^3 c \tag{1.16}$$

where γ is activity coefficient, it is seen that the formal potential can be formulated as

$$E_f^0 = E^0 + \frac{RT}{F} ln \frac{\tilde{A}f\text{Å}½\tilde{A},\hat{A}^3{}_O}{\tilde{A}f\text{Å}½\tilde{A},\hat{A}^3{}_R} \tag{1.17}$$

The formal potential in one medium is different to the others depending upon the interactions of ions in the solution. However the difference is often insignificant and the value will approximately the same as standard potential.

1.1.2 Electrical Double Layer

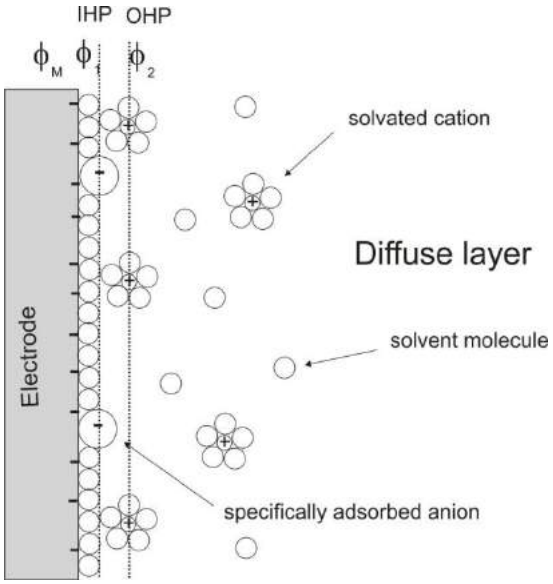

Figure 1. 1 : model for the structure of electrode/solution interface

The structure of electrode/solution interface is depicted in Figure 1. 1. The structure was first proposed by Helmholtz[1]. When a potential is applied on the electrode, the ions and the solvent molecules respond to the charge of the electrode surface in order to achieve electro-neutrality across the interface. The interface solution is thought to be made up of several layers. The Inner Helmholtz Plane (IHP) consists of solvent molecules and specifically adsorbed ions. Solvated ions can only approach to the electrode up to the region near the specifically adsorbed ions through long-range electrostatic interactions. This region is defined by the Outer Helmhotz Plane (OHP) which passes through the center of solvated non-specifically adsorbed ions. The non-adsorbed ions are distributed to bulk solution which is known as the diffuse layer. The thickness of the diffuse layer depends on the total ionic concentration in the solution

and typically is less than 300 Å (for 0.1 M and 10^{-3}M ionic concentration the thickness of diffusion layer are ~10 Å and ~100 Å respectively). In addition, the electroactive active species must enter the interfacial region in order to allow the electron transfer process via electron tunelling mechanisms which takes place over a distance within 10-20 Å from the electrode surface.[1] The potential drops between the electrode and the bulk solution ($\phi_m - \phi_s$) must occur within the similar distance. In practice, this can be achieved by adding an excess amount of supporting electrolyte to compress the potential drop to this distance. Typically, the concentration of the supporting electrolyte is > 10^{-1} M. The chosen supporting electrolyte must be inert chemically and electrochemically in the range of potential where experiments were performed. In the case for an experiment which is conducted in poorly conducting media, Frumkin corrections[1] should be performed to account for the potential drop over large distances.

1.2 Dynamic Electrochemistry

1.2.1 Faradaic and Non-Faradaic Processes

There are two types of processes take place on the electrode surface; these are Faradaic and non-Faradaic processes. The Faradaic process which is named after Sir Michael Faraday relates to the electron transfer process on the electrode surface. The charge passed during the process is proportional to the amount of material being converted and the resulting current, If, is given by the equation:

$$I_f = nFJA \tag{1.18}$$

where *n* is the number of electrons transferred per molecule, *J* is the flux which is the number of moles of reacting electroactive species passing through a unit area per unit time, *A* is the area of the electrode surface and *F* is the Faraday constant (96486 C mol^{-1}).

Meanwhile, non-faradaic processes relate to the changes in the structure of the double layer caused by the adsorption or desorption of ions when a potential is applied to the electrode. The current produced in this process is capacitive as the electrodes behave like a capacitor where the charge stored, Q, in the capacitor follows the equation :

$$Q = C_d A \Delta \emptyset \tag{1.19}$$

C_d is the capacitance (Farads), $\Delta \emptyset$ is the potential difference across the double layer and A is the area. The capacitive charging current when the potential is applied at υ constant scan rate, is given by the equation:

$$I_c = \frac{dQ}{dt} = C_d A v \tag{1.20}$$

The non-faradaic current becomes significant at a high scan rate and distortion to observed faradaic processes may occur.

1.2.2 Mass Transport

The electroactive species are transported to and from electrode surface by means of three modes of mass transport. These are diffusion, migration and convection. Knowledge of mass transport is essential in electrochemistry because mass transport can be a limiting factor in the overall rate of an electrochemical reaction.[1-3]

1.2.2.1 Diffusion

Diffusion is a spontaneous movement of species driven by the concentration gradient in a solution. This process occurs from high to low concentration in order to equilibrate the system. A concentration gradient is formed when the electroactive species near the electrode surface is depleted, forcing the fresh material to replenish the exhausted region. The flux of material diffusing, *j*, is expressed by Fick's first Law:

$$J = -D\frac{\partial c}{\partial x} \tag{1.21}$$

where D is the diffusion coefficient ($m^2\ s^{-1}$) and $\partial c / \partial x$ is the concentration gradient in the x direction. Typical values of D in aqueous solution are in the range of 10^{-5} to 10^{-6} $cm^2\ s^{-1}$. The negative sign is to emphasize that the concentration gradient is in the opposite direction to the diffusion.

To understand the variation of concentration with time, we should consider the diffusion in one dimension as described in the scheme in Figure 1. 2

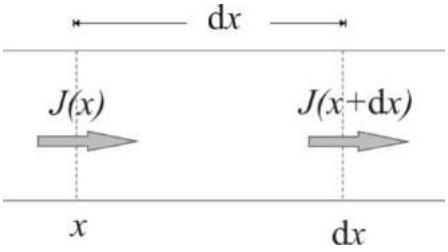

Figure 1. 2 : Schematic diagram of the flux of species in and out of a zone at thickness *dx*

The change in concentration with time can be expressed in equation 1.22:

$$\frac{\hat{a}^{\wedge},c}{\hat{a}^{\wedge},t} = \frac{J(x) - J(x+dx)}{dx} \tag{1.22}$$

considering that

$$J(x+dx) = J(x) + \frac{\hat{a}^{\wedge},J(x)}{\hat{a}^{\wedge},x}dx = J(x) - \frac{\hat{a}^{\wedge},}{\hat{a}^{\wedge},x}D\frac{\hat{a}^{\wedge},c}{\hat{a}^{\wedge},x}dx = J(x) - D\frac{\hat{a}^{\wedge},^2c}{\hat{a}^{\wedge},x^2} \tag{1.23}$$

Since D is constant, substituting equation 1.23 leads to Fick's second law :

$$\frac{\hat{a}^{\wedge},c}{\hat{a}^{\wedge},t} = D\frac{\hat{a}^{\wedge},^2c}{\hat{a}^{\wedge},x^2} \tag{1.24}$$

In three dimensions this equation can be expressed as equation 1.25 below

$$\frac{\partial c}{\partial t} = D\left(\frac{\partial^2 c}{\partial x^2} + \frac{\partial^2 c}{\partial y^2} + \frac{\partial^2 c}{\partial z^2}\right) \tag{1.25}$$

1.2.2.2 Migration

Migration is the movement of species under the influence of an electric field. The migratory flux, j_m, can be quantified by using the equation:

$$j_m \propto - uc\frac{d\phi}{dx} \tag{1.26}$$

where u is ionic mobility, c is concentration and $d\phi/dx$ is the potential gradient (electric field). Because of the complexity of the interface, migration is often hard to calculate accurately. To minimise the effect of migration in voltammetry, in practice a large excess of supporting electrolyte, which should be inert both chemically and electrochemically, is introduced in the solution. The concentration of the supporting electrolyte must at least 30 times higher than the concentration of the electroactive species if migration is to be neglected compared to diffusion.

1.2.2.3 Convection

Convection can be described as a movement of species because of the mechanical forces working on the solution and can be divided into two types. The first is natural convection which results from differences in temperature or density within the solution. The presence of natural convection is unpredictable and this should be taken into account when slow voltage scan rate is applied. The second type is forced convection which occurs under the influence of an external force such as stirring, motion of electrodes or bubbling of gas through the solution. Compared to natural convection, forced convection is predictable and bigger by several orders of magnitude. Forced convection may be introduced to overcome the natural convection to improve the reliability and reproducibility of experimental results.

1.2.3 Heterogeneous Electron Transfer

To explain the Butler –Volmer model, a simple one electron transfer reaction where O is reduced to form R should be considered:

$$O + e^- \underset{k_b}{\overset{k_f}{\rightleftharpoons}} R \tag{1.27}$$

where k_f and k_b are the forward and backward rate constants for the heterogeneous electrochemical reaction respectively. The current flow in the electrode depends on the rate constants and the concentrations of species O and R at the electrode surface. At a given potential, the overall current can be expressed as the sum of the currents for the forward and reverse processes:

$$i = i_b + i_f = FAk_b[R]_0 - FAk_f[O]_0 \tag{1.28}$$

where F is Faraday constant, A is the area of electrode and $[R]_0$ and $[O]_0$ are the concentrations of species R and O at the electrode surface. The two rate constants, k_f and k_b, can be expressed as follows:

$$k_f = k^0 exp\left[\frac{-\alpha F}{RT}(E - E_f^0)\right] \tag{1.29}$$

$$k_b = k^0 exp\left[\frac{(1-\alpha)F}{RT}(E - E_f^0)\right] \tag{1.30}$$

where k_0 is the standard electrochemical rate constant, $(E - E_f^0)$ is the overpotential (the difference between the potential and the formal potential) and α is the transfer coefficient (a measure of the symmetry of the energy barrier for electron transfer). The equality $k_f = k_b$ is reached when no overpotential $E - E_f^0$ is applied. The value of α lies between 0 to 1 and is usually close the value of 0.5 which means that the transition state is in intermediate between O and R.

If equation (1.29) and (1.30) are substituted in equation (1.28), the resulting equation (eq. 1.31) describes the dependency of the current on the overpotential for a process which is controlled by electrode kinetics. This equation is known as the Butler-Volmer

equation and predicts the electrical current variation as a result of variation in electrode potential.

$$i = FAk^0\left([R]_0 exp\left(\frac{(1-\hat{I}\pm)F(E-E_f^0)}{RT}\right) - [O]_0\left(-\frac{\hat{I}\pm F(E-E_f^0)}{RT}\right)\right) \quad (1.31)$$

1.3Microelectrodes

Microelectrodes can be defined as electrodes that have dimensions up to tens of micrometers. The geometry can be disks, hemispheres, bands or rings. As a consequence, the current measured at microelectrode is very small (usually in the order of nano amperes or below) compared to that of macroelectrodes. Such a small dimension also alters the diffusional behaviour of material to the electrode surface. In macroelectrodes generally, the electroactive species diffuse linearly to the surface of electrode. As the size of the electrode becomes smaller and smaller, the effect of the diffusion at the edge of electrode surface becomes greater due to convergent diffusion. The current density increases as a result of the increase of the rate of mass transport. In addition, at such small dimensions, only a tiny amount of material is electrolyzed resulting in a small diffusion layer and high concentration gradients.

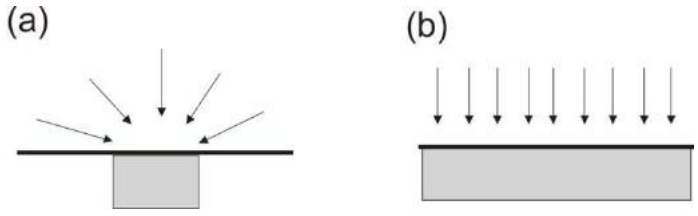

Figure 1. 3: Convergent diffusion in (a) microdisc electode and (b) planar diffusion in macroelectrode

The characteristic of the convergent diffusion in microelectrodes brings many consequences to its properties. Firstly, a steady state for a faradaic process is reached very rapidly. This steady state current for a disk microelectrode is independent of scan rate, n, as described mathematically in the equation:

$$I_{ss} = 4nFDc_{bulk}r_d \tag{1.32}$$

where r_d is the radius of the microdisk electrode. Secondly, as the non-faradaic current is proportional to the area, the non-faradaic current becomes insignificant compared to the faradaic current resulting in an improved ratio of faradaic to non-faradaic currents. As such condition, the applied potential can be scanned very rapidly without distorting the steady state current. For a practical reason, the signal to noise ratio is also improved. Thirdly, the ohmic drop of potential, *IR*, is suppressed since only a small amount of current is measured.

1.4 Voltammetric Methodology

Voltammetry is the electroanalytical method which concerns the measurement of current as a function of the applied potential. Basically, this technique requires three electrodes which are the working, reference and auxiliary (counter) electrodes. The applied potential, *E*, between the working and reference electrode is mathematically expressed by the equation:

$$E = (\tilde{A}\ \hat{a}\text{€}\text{¢}_m - \tilde{A}\ \hat{a}\text{€}\text{¢}_s) + iR + (\tilde{A}\ \hat{a}\text{€}\text{¢}_s - \tilde{A}\ \hat{a}\text{€}\text{¢}_{ref}) \tag{1.33}$$

where $(\phi_m - \phi_s)$ is the potential drop between the working electrode and the solution, $(\ddot{I}\bullet_s - \ddot{I}\bullet_{ref})$ is the potential drop at reference electrode/solution interface and iR is the potential drop between the two electrodes. When the current resulting from the faradaic and non-faradaic processes is very small, the iR drop can be neglected. This is for the case when a microelectrode is used.

1.4.1 Linear Sweep Voltammetry

Linear sweep voltammetry (LSV) is generally performed in a static solution so that the mass transport of electroactive species to the electrode surface is controlled by diffusion. In LSV, the potential is applied from E_1 to E_2 linearly with time during the measurement as depicted in Figure 1. 4a. It is clear that the slope of the line is the value for the scan rate which can vary from a few millivolt per second up to a million volts per second. However, applying such a low scan rate is restricted by the influence of natural convection while high scan rate measurement will be distorted by the high capacitive charging effect.

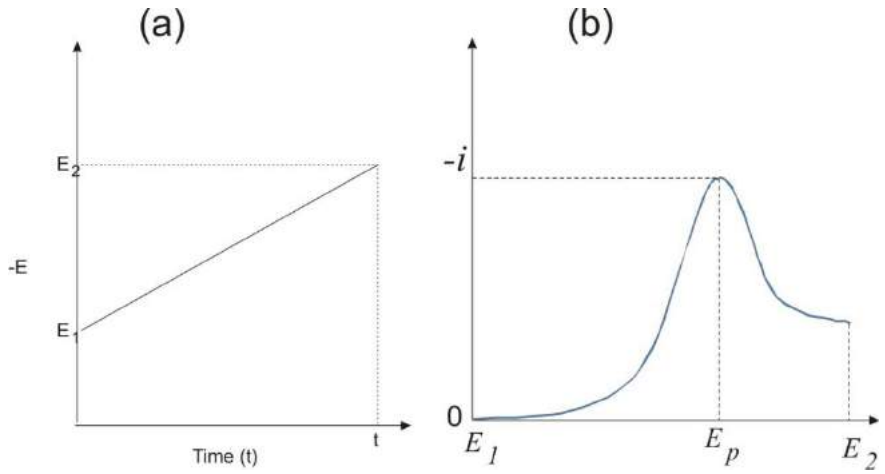

Figure 1. 4: The potential sweep and current-voltage curve in linear sweep voltammetry

Figure 1. 4b displays the current-voltage curve produced in LSV. The starting potential, E_1, is applied to the working electrode where initially non-faradaic processes only occur. After this have decreased, the potential is swept at a constant rate to a more negative potential, the faradaic process becomes favourable once the potential is negative enough to induce the electron transfer of the reaction $O + e^- \rightleftharpoons R$ (k^0 is increased). Consequently, the current increases and reaches to its maximum (I_p) at the potential E_p. At potentials more than E_p, the process is controlled by the rate of diffusion to the electrode where the surface concentration drops effectively to zero. The current is a balance between the electrode kinetics (k^0) and the surface concentration of O. The flux of fresh material to the electrode surface is eventually compromised by

gradual depletion of avaliable species within the diffusion layer resulting in a decline the observed current. This explains the appearance of a peak in the voltammogram.

1.4.2 Cyclic Voltammetry

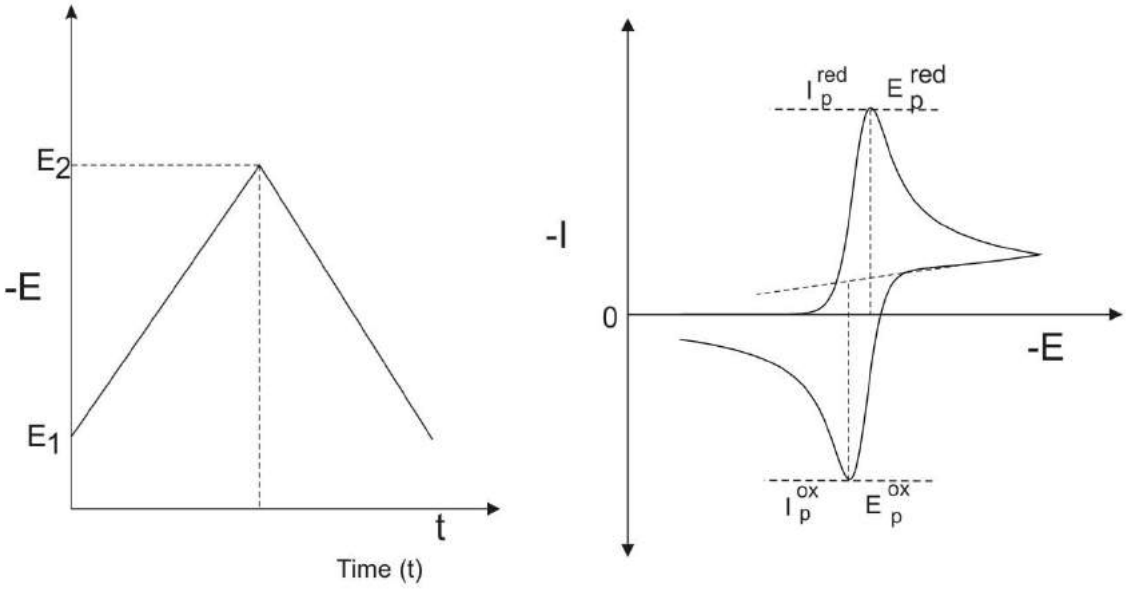

Figure 1. 5: The triangular waveform in cyclic voltammetry experiment

Cyclic voltammetry is an extension of the linear sweep technique. In cyclic voltammetry, after reaching the potential E_2, the potential is swept back to the original value, E_1, forming the triangular waveform as shown in Figure 1. 5. The cycle can be done in more than once depending upon the system under investigation. The current-voltage plot resulting from this technique gives qualitative and quantitative information to characterise the system of interest such as thermodynamics, kinetics, the effect of solvent media, as well as chemical or physical processes occurring.

1.4.2.1 Cyclic Voltammetry at Macroelectrodes

The shape of the forward scan in the current-voltage plot is similar to that of LSV. The backward scan, where the potential is swept positively from E_2 to E_1, induces the reverse reaction ($R \rightarrow O + e^-$) and gives current of opposite sign to the forward scan. In

other words, the product of the reduction, R, is oxidized back to O and the current related to this process is an anodic current. The initial anodic current is relatively high due to the high concentration of R in the diffusion layer. As potential is swept positively, the kinetics for the oxidation reaction increases and the conversion of R to O becomes favourable resulting in the current increase. After reaching a maximum (at E_p^{ox}, i_p^{ox}) the current starts to decay as concentration of R is depleted creating a diffusion layer and mass transport process controls the process. The voltammogram produced depends on the electrochemical rate constant (k^0), the formal potential of the redox couple, the diffusion coefficient of each species O and R as well as the scan rate (ν). The sweep rate controls the time scale of electrolysis and hence determines the diffusion layer thickness. At higher scan rates, a relatively short time is required for electrolysis resulting in relatively thin diffusion layer. Consequently, the flux of material to the electrode surface is higher (Fick's first law) producing a relatively high peak current. For a fully reversible one-electron redox reaction (characterized by large k^0 value) the peak current flows at a macroelectrode follows the Randles-Sevčik equation:

$$i_p = (2.69\tilde{A}f\text{Æ}'\tilde{A} \dagger \hat{a}\text{€}\text{™}\tilde{A}f\hat{a}\text{€}\,\tilde{A}\text{¢}\hat{a},\neg\hat{a},\text{¢}\tilde{A}f\text{Æ}'\tilde{A},\hat{A}\text{¢}\tilde{A}f\hat{A}\text{¢}\tilde{A}\text{¢}\hat{a},\neg\text{Å}\text{¡}\tilde{A},\hat{A}$$
$$)AD^{\frac{1}{2}}\tilde{A}f\text{Æ}'\tilde{A} \dagger \hat{a}\text{€}\text{™}\tilde{A}f\hat{a}\text{€}\text{¦}\tilde{A},\hat{A}\text{½}\tilde{A}f\text{Æ}'\tilde{A}\text{¢}\hat{a},\neg\text{Å}\text{¡}\tilde{A}f\hat{a}\text{€}\text{š}\tilde{A},\hat{A}\text{½}^{\frac{1}{2}}c_{bulk}$$

where n is the number of electrons, A is the area of the electrode, D is the diffusion coefficient, υ is the scan rate and c_{bulk} is the concentration of the electroactive species in bulk solution. In the case of irreversible reaction, the peak current can be calculated according to equation 1.35:

$$i_p = (2.99 \times 10^5)\alpha^{\frac{1}{2}} A D^{\frac{1}{2}} \nu^{\frac{1}{2}} c_{bulk} \tag{1.35}$$

where α is the transfer coefficient and n =1 is assumed.

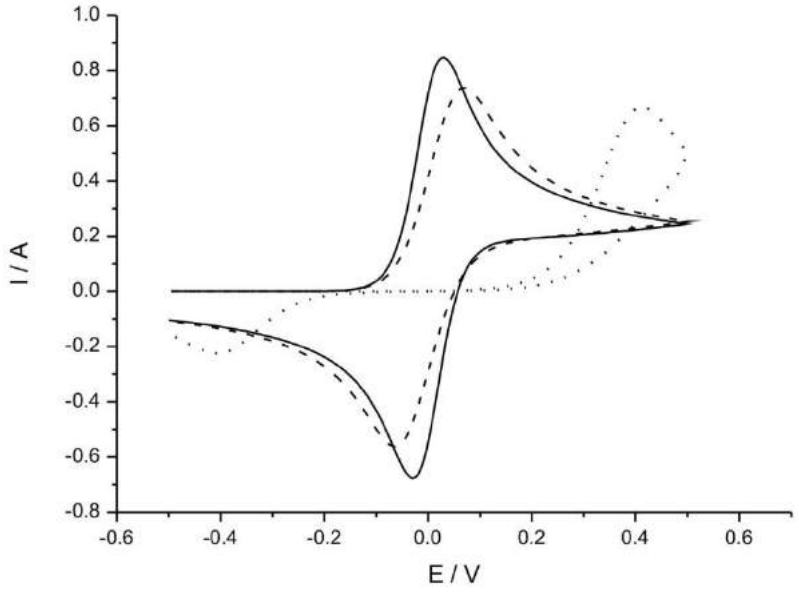

Figure 1. 6 The cyclic voltammogram at macroelecrodes for reversible (solid line) quasi-reversible (dashed line) and irreversible (dotted line)

The voltage-current curve (voltammogram) produced can give information about the reversibility of the electron transfer reaction. Figure 1. 6 above displays reversible (solid line), quasi reversible (dashed-line) and irreversible (dotted-line) voltammograms. A reaction is said to be reversible if it has fast electron kinetics (characterized by k^0), while the irreversible reaction has slow electron kinetics. The terms of 'fast' and 'slow' are always compared to the rate of mass transport which is measured by the mass transport coefficient, m_T,

$$m_T \sim \sqrt{\frac{DF\nu}{RT}} \tag{1.36}$$

Using the mathematical notation, therefore:

$k^0 \gg m_T$ For reversible

$k^0 \ll m_T$ For irreversible

Matsuda and Ayabe[1] introduce a dimensionless parameter Λ, a ratio between standard rate constant and mass transport coefficient, according to equation

$$\Lambda = \frac{k^0}{\left(DFv/RT\right)^{1/2}} \tag{1.37}$$

This parameter is used to differentiate three types of electron transfer reaction at stationary macroelectrode measured at 298 K and assuming α value to be 0.5 as presented in Table 1.1[1]

Table 1.1 Classification limits for reversible, quasi-reversible and irreversible processes.

	Λ value	k^0 value (cm s^{-1})
Reversible	≥ 15	$\geq 0.3\,v^{1/2}$
Quasi-reversible	between 10^{-3} and 15	between $2 \times 10^{-5}\,v^{1/2}$ and $0.3\,v^{1/2}$
Irreversible	$\leq 10^{-3}$	$\leq 2 \times 10^{-5}\,v^{1/2}$

1.4.2.2 Cyclic Voltammetry at Microelectrodes

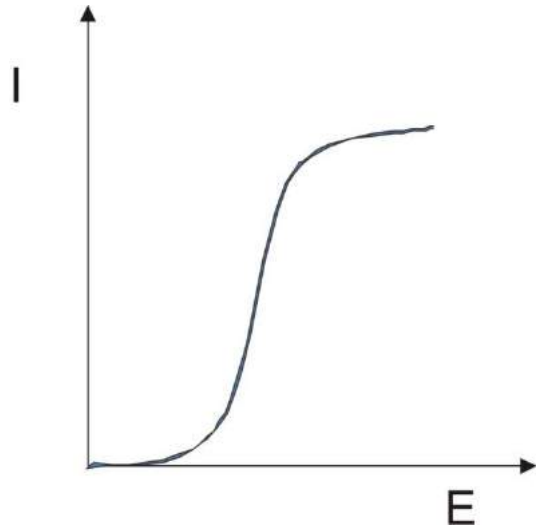

Figure 1. 7 Typical cyclic voltammogram at microelectrodes

Figure 1. 7 displays the typical voltammogram for microelectrodes. Unlike the voltammogram for macroelectrode where the appearance of peaks are observed, the voltammogram for microelectrode is a sigmoidal shape. The sigmoidal shape arrises from the convergent diffusion and this is called steady-state voltammetry. At enough slow scan rate, the steady state behaviour occurs since the rate of mass transport to the electrode surface is fast and this makes the continuous replenishment of electroactive species to the electrode surface happen over the potential range. The limiting current which is the characteristic of the voltamogram is proportional to the diffusion coefficient and can be calculated using the equation 1.32. This equation can be used to electrochemically calibrate the radius of the electrode as well as to determine the diffusion coefficient of electroactive species. Another characteristic of the volatmmogram is the half wave potential, $E_{1/2}$. The formal potential for fast electrode kinetics process falls close to $E_{1/2}$, whereas slow electrode kinetics deviate the $E_{1/2}$ from the formal potential.

1.4.3 Chronoamperometry

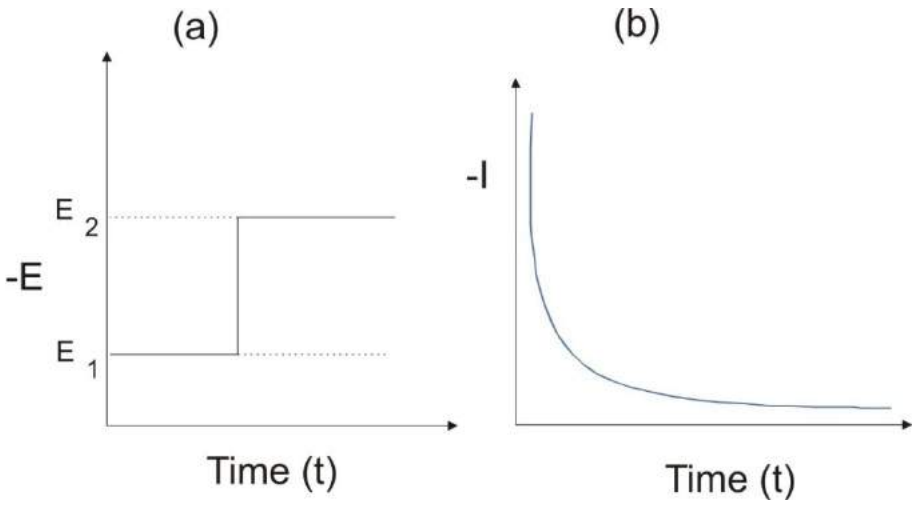

Figure 1. 8 The potential versus time plot (a) and the current response in chronoamperometry experiment

In this technique, initially the working electrode is held at a potential E_1 where no electrolysis occurs and suddenly the potential is stepped to a value of E_2 where the conversion of O to R is transport controlled. The waveform for this technique is depicted in Figure 1. 8a. As a result of this potential step, a rapid increase in the current is observed followed by decrease steadily over-time. The rapid increase of the current comes from the fact that at such a rapid change in the potential results in high concentration gradient. As the electrolysis occurs over time, the diffusion layer thickness increases and the current gradually decreases (Figure 1. 8b).

At a macroelectrodes, where planar diffusion dominates, the decrease in the current follows the Cottrell equation

$$i = \frac{nFAD_0^{\frac{1}{2}}c_{bulk}}{\pi^{\frac{1}{2}}t^{\frac{1}{2}}} \tag{1.38}$$

If the area of the electrode (A) and the bulk concentration of species (c_{bulk}) are known, for a simple electron transfer reaction where the number of electron is known, the

diffusion coefficient of a species can be determined using this equation from the linear relationship between *i* vs $^{1}/_{\sqrt{t}}$

In the case where convergent diffusion dominates (at microelectrodes), more complex processes happen at longer time as current is reaching steady state behaviour. In this case, two factors must be taken into account. First, at a very short time, the planar diffusion dominates so that the current is proportional to the square root of diffusion coefficient and Cottrell equation is followed. However, at longer times, the convergent diffusion replaces the planar diffusion so that the Cottrell equation is not obeyed. The current decays to its limiting value and is proportional to the diffusion coefficient. The full time current-time transient has been calculated as a function of dimensionless time, τ[1]:

$$i = 4nFcDr_e f(\tau) \tag{1.39}$$

with τ

$$\ddot{I}_{„} = \frac{4Dt}{r_e^2} \tag{1.40}$$

where *n* is the number of electron transferred, *F* is the Faraday constant, *D* is the diffusion coefficient, *c* is the initial concentration of the target analyte, r_e is the radius of the electrode and t is the time. For short times, when $\tau < 1$

$$f(\tau) = \left(\frac{\pi}{4\tau}\right)^{1/2} + \frac{\pi}{4} + 0.094\tau^{1/2} + ..., \tag{1.41}$$

and at long times, $\tau > 1$

$$f(\tau) = 1 + 0.7185\tau^{-1/2} + 0.005626\tau^{-3/2} - 0.00646\tau^{-5/2} + ..., \tag{1.42}$$

Shoup and Szabo derived a single expression for an entire time with a maximum error of less than 0.6% :

$$f(\tau) = 0.7854 + 0.8863\tau^{-1/2} + 0.2146exp(-0.7823\tau^{-\frac{1}{2}}) \quad (1.43)$$

1.4.4 Stripping Voltammetry

Stripping voltammetry is very important in the detection of traces of metal ions in solution. In this method, the material under investigation is deposited on the electrode surface followed by stripping off the deposit from the surface. The deposition can be performed through faradaic (reductive or oxidative deposition) or non-faradaic (adsorptive) processes. The stripping off process employs the linear sweep method and this can also be done either in oxidative or reductive direction. Depending upon the stripping process, this technique can be categorised as anodic stripping voltammetry (ASV) and cathodic stripping voltammetry (CSV).

Anodic stripping voltammetry (ASV) commonly employs mercury electrodes which can be in the form of static drop, hanging drop or thin layer film.[4] This technique is powerful to determine traces amount (sub-ppb level) of heavy metals such as copper,[5,6] lead,[7] cadmium[8] and zinc[9]. The scheme below illustrates the process in ASV :

Accumulation (preconcentration step): $M^{n+}(aq) + ne^- \rightarrow M$ (electrode)

Stripping (determination step): M (electrode) $\rightarrow M^{n+} + ne^-$

Cathodic stripping voltammetry (CSV) is the inverse of ASV. The material under determination is oxidised at the electrode surface in the preconcentration step prior to reduction in the determination step. Metal ions that can form oxides on the electrode surface such as Pb^{2+} ion[10] or Mn^{2+} ion[11] are commonly determined using CSV. The scheme below illustrates the processes in CSV:

Preconcentration: $aM^{n+}(aq) + bH_2O + (an-2b)e^- \rightarrow M_aO_b$ (electrode) $+ 2bH^+$

Stripping: M_aO_b (electrode) $+ 2bH^+ \rightarrow aM^{n+}(aq) + bH_2O + (an-2b)e^-$

1.5 Simulation for deposition and stripping processes

A large part of this thesis concerns the simulation of deposition and stripping process for the Group I Alkali Metals on microelectrode studies. The mathematical model to run the simulation is developed by Dr. Sarah E Ward-Jones[12] and has been applied first to study the Li/Li^+ couple in THF[13] and for the study of the Ag/Ag^+ couple in ionic liquid[14]. This model and the associated computer programs were developed from the "thick layer" model for stripping voltammetry reported in reference[15]. This model is designed to simulate the stripping of bulk metal from a surface of bulk metal and has a characteristic sharp drop at the end of the stripping peak. A summary of the mathematical model is provided below.

The electrode reaction of interest for the deposition and stripping of metal (M) under cyclic voltammetry conditions is assumed to follow a one-electron transfer mechanism:

$$M^+(sol) + e^- \underset{k_d}{\overset{k_a}{\rightleftharpoons}} M(electrode) \tag{1.44}$$

where the M^+ ions are in solution and M is a bulk solid on the electrode surface. The process is assumed to display Butler-Volmer kinetics[2,16] according to the equations below. k_a is the rate constant for addition to the surface and k_d is the rate constant for dissolution:

$$k_a = k^0 exp\left[\frac{-\alpha F}{RT}(E - E_f^0)\right]$$

$$k_d = k^0[M^+]^* exp\left[\frac{(1-\alpha)F}{RT}(E - E_f^0)\right]$$

where k^0 is rate constant (units of cm s^{-1}) for the M^+/M couple, α is the transfer coefficient and E_f^0 is the formal potential. $[M^+]^*$ is the standard concentration equal to 1×10^{-3} mol cm^{-3} and is included to reflect the different standard states of M and M^+. *R*

is the ideal gas constant (8.314 J K^{-1} mol^{-1}), F is Faraday constant (96485 C mol^{-1}) and T is the absolute temperature in K.

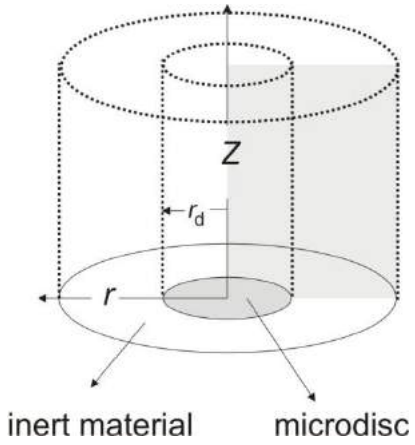

Figure 1. 9: The cylindrical coordinate system used in the simulation for a microdisc electrode

The electrode is modelled as a microdisk with radius r_d which gives cylindrical symmetry to the system (Figure 1. 9). The problem can therefore be considered as two dimensional with the r coordinate axis running parallel to the electrode surface from the centre of the electrode out into the solution and the z coordinate axis being perpendicular to the electrode surface, with $z = 0$ being the electrode surface. The maximum distance simulated is set to be $6\sqrt{Dt}$ from the electrode surface. The height of any metal deposit formed is ignored and as such the microdisk and the metal deposit are always approximately modeled as a flat disk.

The diffusion behaviour of M^+ within the solution is given by Fick's second law using cylindrical coordinates[1]:

$$\frac{\partial[M^+]}{\partial t} = D\left(\frac{\partial^2[M^+]}{\partial r^2} + \frac{1}{r}\frac{\partial[M^+]}{\partial r} + \frac{\partial^2[M^+]}{\partial z^2}\right) \tag{1.47}$$

The position dependent surface coverage, $\tilde{A}f\text{Æ}'\tilde{A}...\hat{A}½\tilde{A}f\hat{A}¢\tilde{A}¢â€šÂ¬\tilde{A}...â€œ_M$, is described by the following rate equation:

$$\frac{\hat{a}^{\wedge},\hat{I}^{\prime\prime}_{M}}{\hat{a}^{\wedge},t} = k_a[M^+]_{surf} - k_d \tag{1.48}$$

This model assumes that the rate of dissolution of metal from the electrode surface is independent of the coverage of metal, Γ_M, whereas the rate of deposition is dependent on the solution concentration of M^+. The value of Γ is not permitted to go below zero, therefore k_d is set equal to zero once $\Gamma_M = 0$. If $\tilde{A}\cent\ddot{E}\dagger\hat{a}\in\check{s}\tilde{A}\check{Z}\hat{a}\in\text{œ}_M < -k_d dt$ for any time step, dt, in the simulation, the value of k_d is adjusted so that $k_d dt = -d\hat{I}^{\prime\prime}_M dt$.

Initially, it is assumed that there are only M^+ species in the solution, therefore the initial condition (t=0) for the species taking part in the reaction are:

$$\begin{aligned}
&[M^+] = [M^+]_{bulk} \quad \text{for} \quad 0\tilde{A}\cent\hat{a}\in^{\circ}\hat{A}\text{¤}r\tilde{A}\cent\hat{a}\in^{\circ}\hat{A}\text{¤}\tilde{A}\cent\ddot{E}\dagger\mathring{A}¾ \quad \text{and} \\
&0 \le z \le \infty \\
&\Gamma_M = 0 \quad \text{for} \quad 0 \le r \le r_d \ \text{and} \ z = 0
\end{aligned} \tag{1.49}$$

The following equations relates to the boundary condition at t > 0 considering a bulk concentration of M^+ at the semi-infinite boundaries and a non-flux boundary condition on the symmetry axis and on the inert material surrounding the microdisc.

$[M^+] = [M^+]_{bulk}$ for $0 \le r \le r_{max}$ and $z = z_{max}$

$\tilde{A}f\text{Æ}'\tilde{A}\dagger\hat{a}\text{€™}\tilde{A}f\hat{a}\in\check{s}\tilde{A},\hat{A}\cent\tilde{A}f\text{Æ}'\tilde{A}\cent\hat{a},\neg\hat{A}^1\tilde{A}f\hat{A}\cent\tilde{A}\cent\hat{a}\in\check{s}\hat{A}\neg\tilde{A},\hat{A}\ \tilde{A}f\text{Æ}'\tilde{A},\hat{A}\cent\tilde{A}f\hat{A}\cent$
$= 0$

for $r = 0$ and $0\tilde{A}f\text{Æ}'\tilde{A},\hat{A}\cent\tilde{A}f\hat{A}\cent\tilde{A}\cent\hat{a}\in\check{s}\hat{A}\neg\tilde{A},\hat{A}^{\circ}\tilde{A}f\hat{a}\in\check{s}\tilde{A},\hat{A}\text{¤}z\tilde{A}f\text{Æ}'\tilde{A},\hat{A}\cent\tilde{A}f\hat{A}\cent\tilde{A}\cent\hat{a}\in\check{s}\hat{A}\neg\tilde{A},\hat{A}^{\circ}$

$\hat{a}^{\wedge},[M^+]/\hat{a}^{\wedge},r = 0$ for $r = r_{max}$ and $0\tilde{A}f\text{Æ}'\tilde{A}\dagger\hat{a}\text{€™}\tilde{A}f\hat{a}\in\check{s}\tilde{A},\hat{A}\cent\tilde{A}f\text{Æ}'\tilde{A}\dagger\hat{a}\text{€™}\tilde{A}f\hat{a}\in\check{s}\tilde{A},\hat{A}\cent\tilde{A}f\text{Æ}'\tilde{A},\hat{A}z_{max}$

$\tilde{A}f\text{Æ}'\tilde{A}\dagger\hat{a}\text{€™}\tilde{A}f\hat{a}\in\check{s}\tilde{A},\hat{A}\cent\tilde{A}f\text{Æ}'\tilde{A}\cent\hat{a},\neg\hat{A}^1\tilde{A}f\hat{A}\cent\tilde{A}\cent\hat{a}\in\check{s}\hat{A}\neg\tilde{A},\hat{A}\ \tilde{A}f\text{Æ}'\tilde{A},\hat{A}\cent\tilde{A}f\hat{A}\cent$
$= 0$

r_dÃƒÆ’Ã
† â€™Ãƒâ€šÃ,Â¢ÃƒÆ’Ã,Â¢ÃƒÂ¢Ã¢â,¬Å¡Ã,Â¬Ãƒâ€šÃ,Â°ÃƒÆ’Ã¢â,–
†
â€™Ãƒâ€šÃ,Â¢ÃƒÆ’Ã,Â¢ÃƒÂ¢Ã¢â,¬Å¡Ã,Â¬Ãƒâ€šÃ,Â°ÃƒÆ’Ã¢â,¬Å
for r_{max}

At the electrode surface, where

0ÃƒÆ’Ã
† â€™Ãƒâ€šÃ,Â¢ÃƒÆ’Ã,Â¢ÃƒÂ¢Ã¢â,¬Å¡Ã,Â¬Ãƒâ€šÃ,Â°ÃƒÆ’Ã¢â,¬Å¡Ãƒâ€šÃ
†
â€™Ãƒâ€šÃ,Â¢ÃƒÆ’Ã,Â¢ÃƒÂ¢Ã¢â,¬Å¡Ã,Â¬Ãƒâ€šÃ,Â°ÃƒÆ’Ã¢â,¬Å¡Ãƒâ€šÃ,Â
r_d

and $z = 0,$ the boundary conditions are given by equations below:

$$\frac{\text{ÃƒÆ’Ã,Â¢Ãƒâ€¹Ã¢â,¬Â ÃƒÂ¢Ã¢â€šÂ¬Ã…Â¡ ÃƒÆ’Ã…Â½ÃƒÂ¢Ã¢â€šÂ¬Ã…â€œ}_M}{\text{ÃƒÆ’Ã,Â¢Ãƒâ€¹Ã¢â,¬Â ÃƒÂ¢Ã¢â€šÂ¬Ã…Â¡}t} = D\left(\frac{\text{ÃƒÆ’Ã,Â¢Ãƒâ€¹Ã¢â,¬Â ÃƒÂ¢Ã¢â€šÂ¬Ã…Â¡}[M^+]}{\text{ÃƒÆ’Ã,Â¢Ãƒâ€¹Ã¢â,¬Â ÃƒÂ¢Ã¢â€šÂ¬Ã…Â¡}z}\right) = k_a[M^+]_{surf} - k_d \qquad (1.51)$$

for $0\text{ÃƒÂ¢Ã¢â,¬Â°Ã,Â¤}r\text{ÃƒÂ¢Ã¢â,¬Â°Ã,Â¤}r_d$ and $z = 0$

$$k_d\partial t =- \partial\Gamma_M + k_a[M^+]_{z=0}\partial t \quad \text{if} \frac{\text{âˆ‚Î“}_M}{\text{âˆ‚}t} > k_a[M^+]_{z=0} - k_d$$

The system of partial differential equations that define this model are solved using a fully implicit finite difference scheme[17] combined with Newton’s method and an extended version of the Thomas algorithm[18,19]. The simulation space is covered with a grid that expands exponentially from the singularity (the electrode/inert material boundary) and the electrode surface [20]. Once the system of equations has been solve the current flowing at the electrode surface can be calculated using the following equation:

$$I =- 2\pi F\int_0^{r_d}\frac{\partial\Gamma_M}{\partial t}r dr \qquad (1.52)$$

1.6 Thesis Overview

The work in thesis is a fundamental study of deposition and stripping Group I Alkali metals in room temperature ionic liquids. The works includes the extracting kinetic and thermodynamic parameters such as $E_f^0, k^0, D,$ Î ± for M/M$^+$ redox couple (M = Li, Na, K, Rb, and Cs) from the experimental data by means of mathematical modelling developed previously by the group. In addition, this thesis also includes a novel work

on *in situ* electrochemical-X-ray photoelectron spectroscopy to study the electrodeposition process of K and Rb.

In Chapter 4, the study of Li/Li^+ redox couple in several room temperature ionic liquids is described. The cyclic voltammetry of the system using platinum and nickel electrodes also discussed. From this, we then move on to study the Na/Na^+ couple in several ionic liquids using only the nickel electrode (since it shows no alloy formation with Lithium metals from the previous study) which is described in Chapter 5. The result from this chapter is compared to that with in Chapter 4. The rest of the alkali metal redox couples (K/K^+, Rb/Rb^+ and Cs/Cs^+) and the general trend in formal potential down the Group I in selected ionic liquid $[C_4mpyrr][NTf_2]$ is discussed in Chapter 6. Chapter 7 and Chapter 8 discuss the novel work on *in situ* electrochemical-X-ray photoelectron spectroscopy to study the electrodeposition process of K and Rb. This Chapter also includes the description of novel electrochemical cell which enables such a combined technique to be performed.

In this Chapter, the fundamentals of electrochemistry which is the basis of this work was presented. The next Chapter, an overview of the room temperature ionic liquids and a brief introduction to X-ray photoelectron spectroscopy are presented.

References

(1) Compton, R. G.; Banks, C. E. *Understanding Voltammetry*, World Scientific, Singapore, 2007.

(2) Bard, A. J.; Faulkner, L. R. *Electrochemical Methods: Fundamentals and Applications*; John Wiley & Sons, Inc., New York, USA, 2001.

(3) Brett, C. M. A.; Brett, C. M. A. *Electrochemistry: Principles, Methods, and Application*; Oxford University Press, Oxford, UK, 1993.

(4) Brett, C. M. A.; Brett, A. M. O. *Electroanalysis*; Oxford University Press Inc.: New York, 1998.

(5) Rodrigues, J. A.; Rodrigues, C. M.; Almeida, P. J.; Valente, I. M.; Goncalves, L. M.; Compton, R. G.; Barros, A. A. *Analytica Chimica Acta* **2011**, *701*, 152-6.

(6) Opoka, W.; Bas, B.; Reczynski, W.; Plonka, M.; Drozdowicz, D.; Sliwowski, Z.; Brzozowski, T. *Acta Poloniae Pharmaceutica* **2011**, *68*, 481-92.

(7) Prabakar, S. J. R.; Sakthivel, C.; Narayanan, S. S. *Talanta* **2011**, *85*, 290-297.

(8) Siriangkhawut, W.; Grudpan, K.; Jakmunee, J. *Talanta* **2011**, *84*, 1366-1373.

(9) Gholivand, M. B.; Azadbakht, A.; Pashabadi, A. *Electroanalysis* **2011**, *23*, 364-370.

(10) Miwa, T.; Motosugi, H.; Mizuike, A. *Japan Analyst* **1971**, *20*, 846-&.

(11) Ghoneim, E. M. *Talanta* **2010**, *82*, 646-652.

(12) Ward-Jones, S. E. PhD thesis, University of Oxford, 2008.

(13) Paddon, C. A.; Jones, S. E. W.; Bhatti, F. L.; Donohoe, T. J.; Compton, R. G. *J. Phys. Org. Chem.* **2007**, *20*, 677-684.

(14) Rogers, E. I.; Silvester, D. S.; Jones, S. E. W.; Aldous, L.; Hardacre, C.; Russell, A. J.; Davies, S. G.; Compton, R. G. *J. Phys. Chem. C* **2007**, *111*, 13957-13966.

(15) Jones, S. E. W.; Chevallier, F. G.; Paddon, C. A.; Compton, R. G. *Anal. Chem.* **2007**, *79*, 4110-4119.

(16) Bard, A. J.; Stratmann, M.; Scafer, J. H. In *Encyclopedia of Electrochemistry, Volume 8, Organic Electrochemistry*; Wiley: New York, 2004.

(17) Strikwerda, J. C. *Finite Difference Schemes and Partial Differential Equations*; Wadsworth & Brookes/Cole: Pacific Grove, CA, 1989.

(18) Kreiszig, E. *Advanced Engineering Mathematics*; John Wiley & Sons: New York, 1962.

(19) Svir, I. B.; Klymenko, O. V.; Compton, R. G. *Radiotekhnika* **2001**, *118*, 92.

(20) Gavaghan, D. J. *J. Electroanal. Chem.* **1998**, *456*, 1-12.

Chapter 2

Introduction to Room Temperature Ionic Liquids and X-Ray Photoelectron Spectroscopy

The work described in this thesis employs room temperature ionic liquids (RTILs) as solvents for studying the deposition and stripping process of Alkali Group I metals. RTILs are a group of solvent which are composed entirely with ions. They possess both distinctive physical and chemical properties compared to traditional molecular solvents. These properties include intrinsic conductivity, electrochemical stability, thermal stability, non-volatility as well as often high viscosity. Such properties offer advantages for their use as solvents in electrochemical measurements. Numerous publications in this area have been reported since their discovery with increasing numbers every year. Moreover, this class of solvent has been utilised in a wide range of research namely energy storage and devices, catalysis, organic synthesis as well as for medical purposes.[1-4]

This chapter aims to introduce briefly room temperature ionic liquids and their physical properties which relate to their use as electrochemical solvents, particularly in electrodeposition as well as the possibility of their use in ultra-high vacuum conditions. A short section in this chapter describes the fundamentals of X-ray photoelectron spectroscopy.

2.1 Introduction

Room temperature ionic liquids can be defined as liquids which are composed entirely of ions and exist in the liquid form at room temperature. One may also say that RTILs are 'ambient temperature molten salts'. These liquids are composed of large unsymmetrical organic cations and weakly-coordinated inorganic anions. This combination makes the Coulombic interaction between the cations and anions low, so decreasing the lattice energy of the salts. Since they are composed entirely of ions, theoretically they possess intrinsic conductivities which remove the need for supporting electrolyte. It is reported that in 1914 Walden[2] is the first one to synthesise an ionic liquid namely ethylammonium nitrate which has a melting point of 12.5^{o}C.

The first generation ionic liquid was based on the haloaluminate such as $[AlCl_4]^-$.[5] It was first reported by Hurley and Wier[5] that mixtures of ethylpyridinium chloride and aluminium chloride are molten at room temperature. Aluminium electrodeposition was conducted using this ionic liquid. Haloaluminate based ionic liquids are not stable in air since they undergo hydrolysis in the presence of water. Therefore they have to be contained in an inert atmosphere environment such as a glove box. The second generation involves the usage of the anions tertrafluoroborate $[BF_4]^-$ and hexafluorophosphate $[PF_6]^-$ which are more stable in air and moisture.[6,7] However, at high temperature, in the presence of water, both anions are hydrolysed releasing the toxic gas HF. The third generation ionic liquids utilise the hydrophobic anions such as bis(trifluoromethylsulfonyl)imide ($[NTf_2]^-$) and perfluoroalkylphosphate ($[FAP]^-$) which are yet more stable in air and moisture. Recent developments in chemical synthesis have introduced the so called 'task-specific ionic liquids' which have the capability to act as catalysts or reagents for specific reactions.[8]

2.1.1 Properties of RTILs

Understanding the properties of RTILs is of importance if we want to exploit them as electrochemical solvents. Generally, RTILs have higher viscosity compared to molecular solvents, good conductivities, negligible vapour pressures and wide electrochemical windows.

Table 2. 1 presents some commonly used room temperature ionic liquids and molecular solvents together with their electrochemical-related properties such as viscosity (η), density (ρ), conductivity (κ) and electrochemical window (EW).

Table 2. 1 A list of commonly used room temperature ionic liquids and organic solvents together with their properties for electrochemical solvents

Ionic Liquid or Molecular Solvent	η at 293 K / cP	ρ at 293 K / g cm^{-3}	κ at 293 K / mS cm^{-1}	EW at 298 / V
[C_2mim][NTf_2]	34[9]	1.53[15]	8.8[9]	4.3[21]
[C_4mim][NTf_2]	52[9]	1.44[15]	3.9[9]	4.8[21]
[C_4dmim][NTf_2]	105[10]	1.42[15]	2.0[18]	5.2[21]
[C_6mim][FAP]	74[11]	1.56[15]	1.3[11]	5.3[21]
[C_4mpyrr][NTf_2]	89[10]	1.40[15]	2.2[19]	5.2[21]
[C_4mim][OTf]	90[9]	1.30[9]	3.7[9]	4.9[21]
[C_4mim][BF_4]	112[10]	1.21[13]	1.7[20]	4.7[21]
[$N_{6,2,2,2}$][NTf_2]	167[12]	1.27[12]	0.67[19]	5.4[21]
[C_4mim][PF_6]	371[13]	1.37[13]	1.5[20]	4.7[21]
[$P_{14,6,6,6}$][NTf_2]	450[14]	1.07[15]	-	5.0[21]
[$P_{14,6,6,6}$][FAP]	464[15]	1.18[15]	-	5.6[21]
[C_4mim]I	1110[16]	1.49[15]	-	2.1[21]
Acetonitrile	0.34[17]	0.79[17]	7.6[17]	5.0[22]*
Dichloromethane	0.44[17]	1.33[17]	1.33[17]	3.5[22]*
N,N-Dimethylformamide	0.92[17]	0.94[17]	4.0[17]	4.3[22]*
Dimethylsulfoxide	1.99[17]	1.10[17]	2.7[17]	4.4[22]*
Propylene Carbonate	2.5[17]	1.21[17]	1.21[17]	4.7[22]*

* Containing 0.1 M TBAP at 295 K

2.1.1.1 Viscosity

Viscosity can be defined as a measure of liquid's resistance to flow. This property is essential in an electrochemistry experiment since it indirectly effects the mass-transport of electroactive species to and from electrode surface. High viscosities slow down the rate of diffusion contolled chemical reactions and limit some applications.[3] Generally, the viscosities of ionic liquids are higher than the viscosity of other molecular solvents by a factor of 10 to 100 times. At room temperature, the viscosities of ionic liquids typcally fall in the range between 10 to 500 cP.[23] Table 2.1 lists the viscosities of some ionic liquids and aprotic solvents.

The structure of the constituent cations and anions determine the viscosity of the ionic liquids.[16,21,24] This is because the difference in the chemical structures results in the difference of intra-molecular as well as inter-molecular forces such as van der Waals forces, coulombic interaction and hydrogen bonding.[16] The stronger the forces, the less mobile the ionic liquid becomes. In general, low molecular mass, small size and symmetrical cations produce more viscous ionic liquids.[2,25] The addition of alkyl side chains in immidazolium rings increases the viscosity of the ionic liquids. This is because longer alkyl chains increase the dispersion forces. This is evident if we compare the viscosity of C_4mimNTf_2 and C_2mimNTf_2 which have viscosities of 52 and 34 cP respectively at 293 K respectively.[9]

The characteristics of the anions also impacts on the viscosity of the ionic liquids in respect to the relative basicity and hydrogen bonding. Symmetrical anions such as $[PF_6]^-$ and $[BF_4]^-$ form more viscous ionic liquids due to the symmetrical charge distribution which in turn increases the coulombic interactions with the cations.[3] In contrast, weak coordinating base anion such as $[NTf_2]^-$ produce less viscous ionic liquids because of the delocalisation of negative charge electron through S-N-S bonds.[26,27]

The viscosity of ionic liquids is temperature dependent. Generally, with increasing temperature, the viscosity decreases. Okoturo and vanderNoot[10] investigated the viscosities of 23 room temperature ionic liquids over the temperature range 283 to 343 K. It was reported that the RTILs with asymmetrical cations without functional groups on the alkyl chain (for example $[C_4mim][BF_4]$, $[C_4dmim][NTf_2]$, $[C_4mpyrr][NTf_2]$ and $[C_4mim][OTf]$) follow the Arrhenius relationship (Equation 2.1) :

$$ln(\eta) = ln(\eta_\infty) + \frac{E_\eta}{RT} \tag{2.1}$$

where η_∞ is the viscosity at infinite temperature, and E_η is the activation energy for viscous flow, R is the universal gas constant and T is temperature.

Other RTILs, in general those with small, symmetrical and low molecular mass cations, more closely follow the Vogel-Tammann-Fulcher (VTF)[10,28,29] relationship, shown in equation

$$\tilde{A}\check{Z}\hat{A}\cdot = \left(A_{\tilde{A}\check{Z}\hat{A}\cdot}\sqrt{T}\right)exp\left(-\frac{k_{\tilde{A}\check{Z}\hat{A}\cdot}}{(T - T_g)}\right) \tag{2.2}$$

where $A_{\hat{I}\cdot}$ and $k_{\hat{I}\cdot}$ are constans, T is the temperature and T_g is the glass transition temperature. Generally, RTILs with small, symmetrical and low molecular mass cations give higher T_g values than RTILs with larger and higher molecular mass.

2.1.1.2 Conductivity

In electrochemistry experiments, the conductivity of the solvent is important as this property relates to the ability of the solvent to conduct electricity. Judging from their definition alone, ionic liquids that consist entirely of ions should have high conductivity. However their conductivities which depend on the availability of charge

carriers and their mobility are less than the conductivities of concentrated aqueous electrolyte solutions.[29] This may be due to the reduction of the number of the charge carriers as result of ion-pairing and ion aggregration.[30] In addition, the large size of the constituent ions and especially the high viscosities in ILs may also reduce their mobilties.[3] Fortunately, compared to organic solvents, ionic liquids possess advantages since their conductivities are intrinsic so that the need for supporting electrolyte in electrochemical practice is removed. As can be seen from

Table 2. 1, the trend in conductivity for a given anion decreases in the order of imidazolium > pyrrolidinium > ammonium and has been correlated to the decrease in the planarity of the cationic core.[21] The planarity of the imidazolium seems to allow higher conductivity compared to that of the bulky tetrahedral shape of the ammonium salt, while the pyrrolidinium resembles the intermediate geometry. [25] It is also noted that the viscosity plays a very important role in the conductivity as conductivity is inversely proportional to the viscosity.[31] As a result, a less viscous ionic liquids such as C_2mimNTf_2 has a significantly high conductivity of 8.8 mS cm^{-1} as compared to more viscous C_4mpyrrNTf_2 having the conductivity of 2.9 mS cm^{-1}. Remarkebly, the conductivity of C_2mimNTf_2 is also higher than the conductivity of electrolyte solution of 0.1 M TBAP in acetonitrile (7.6 mS cm^{-1}).

Since the viscosity is influenced by temperature, the conductivity of ionic liquids is also temperature dependent. Generally, at increased temperature the conductivity of ionic liquids increases because of the increased mobility as a result of a decrease in viscosity. The tempearture dependency of the ionic liquids viscosity theoretically follows the Vogel-Tamman-Fulcher[28,29] relationship given below:

$$\hat{I}^{o} = A_{l}\sqrt{Te^{-B_{l}}}(T - T_{g}) \qquad (2.3)$$

where κ is conductivity, A and B are empirically derived constants, and T_g is the ideal glass temperature at which the conductivity drops to zero.

2.1.1.3 Vapour Pressure

One of the important and most exploited properties of ionic liquids is the near zero vapour pressure at ambient temperature. This makes the ionic liquids possible to be used in liquid-liquids extractions with theortically 100% recyclability as well as being free from volatile organic compound pollutants.[32,33] The very low vapour pressure up to the decomposition temperature arises from the strong coulombic interactions between ions in the liquids.[3,34] Therefore, it is often noted that ionic liquids do not evaporate in the reaction vessel at room temperature. However, Robelo and co-workers[35] reported that long alkyl chain imidazolium based ionic liquids ($[C_{10}mim][NTf_2]$ and $[C_{12}mim][NTf_2]$) can be distilled at 70 ^oC and extremely low pressure without any sign of decomposition. Long alkyl chain cation and quite bulky with electron delocalisation anion result in low coulombic interactions hence lower the boiling point and increased vapour pressure. Meanwhile, MacFarlane and co-workers[36] also reported that certain ionic liquids such as $[P_{6,6,6,14}]Cl$ behave as intermediate between molecular solvent and true ionic liquids. Such behaviour leads to high vapour pressures so that experimentally it is possible to evaporate the ionic liquid at 0.1 Torr and 353 K.[36]

2.1.1.4 Density

Generally, ionic liquids are denser than many organic solvents and water. The magnitude of the density usually lies between 1.00 to 1.6 g cm^{-3} depending upon the structure.[37] The side alkyl chain length on cations contributes to the difference in the densities. Generally, increasing the length of alkyl chain on immidazolium cations

decreases the density.[16,37] The decrease is also observed for ammonium and sulfonium salts. Aromatic onium based ionic liquids usually have densities higher than that of aliphatic ammonium salts and the trend in density usually follows the sequence: pyridinium salts > imidazolium salts > aliphatic ammonium salts ≈ piperidinium salts.[38] Anions also affect the density of the RTILs. Similar to cations, the density decreases with increasing alkyl chain length. Addition of fluorine atoms in the anion structures which results in the increased molecular weight increases the density. For example, for the density of 1-ethyl-3-methylimidazolium salts increases with the following anion species: $CH_3SO_3^-$ < BF_4^- and CF_3COO^- < $CF_3SO_3^-$ < $(CF_3SO_2)_2N^-$ < $(C_2F_5SO_2)_2N^-$.[39] As with many other materials, the density of ionic liquids decreases with increasing temperature (Ï â^ $1/T$)[40].

2.1.1.5 Electrochemical Window

One important property of RTILs to be used as electrochemical media is their electrochemical windows. Electrochemical windows of RTILs are usually wider than the electrochemical windows of molecular solvent but exceedingly larger than that for the aqueous electrolytes.[9] It has been reported that the typical electrochemical windows for some RTILs are in the range of 4.5 to 5 V.[25]

The electrochemical windows can be described as the potential ranges over which the RTILs are stable toward electrochemical oxidation and reduction. Usually, cyclic voltammetry is applied to determine the potential range. The working electrode is scanned in both directions anodic and cathodic. A large increase in oxidation and

reduction currents implies a signal for their decomposition. Typically, a current density of 1 mA cm^{-2} or 5 mA cm^{-2} is high enough to be used as a limit.[21] However, comparing the electrochemical windows for RTILs is rather difficult because many factors influence the determination such as purity and the electrode used.[3] As explained in the next section, the presence of impurities shrinks the electrochemical windows. Moreover, the material used for working electrode may alter the decomposition of the RTILs. It is reported that due to the catalytic activity of platinum electrode, the electrochemical window of $[C_4mim][CF_3COO]$ is shorter with platinum than that of with glassy carbon.[41] A recent study by Rogers et al.[42] also suggests that it is also important to consider the oxidation of the working electrode which may narrow the anodic limit.

The electrochemical window is dictated by the nature of the cations and anions comprising the RTILs. Quartenary ammonium and pyrrolidinium salts are found to be quite stable towards reduction as compared to imidazolium salts.[3,9,19] For example the electrochemical windows for $[N_{6,2,2,2}][NTf_2]$ and $[C_4mpyrr][NTf_2]$ are 5.4 and 5.2 V respectively which are wider than that for $[C_4mim][NTf_2]$ (4.8 V). It is suggested that the C_2-H proton is vulnerable to reduction to form a carbine due to its acidity.[9,43] This was confirmed by the observation that when one of the C_2-H protons is substituted with an alkyl chain, it becomes weaker and less prone to reduction resulting in a wider electrochemical window; for example the potential window for $[C_4dmim][NTf_2]$ is 5.2 V. A wider potential window is also reported by Buzzeo et. al[44] for the phosphonium class of RTILs. For a given anion, the general trend in increasing the electrochemical window follows the order $[C_nmim]^+ < [C_nmpyrr]^+ < [N_{a,b,c,d}]^+ < [P_{a,b,c,d}]^+$.[44]

For the oxidative limit, the identity of anions plays an important role. Halide anions are easily oxidised at relatively less positive potential releasing halogen gas. This fact

makes the halide based RTILs possess narrow electrochemical windows. Fluorinated anions on the other hand such as $[PF_6]^-$, $[BF_4]^-$, $[NTf_2]^-$ and $[FAP]^-$ stabilise the RTILs towards oxidation. The $[FAP]^-$ anion is found to be the very stable and enhancing the anodic limit.[44] The widely used anion $[NTf_2]^-$ is also known to be stable to oxidation. Recent study[45] suggests that it could undergo reduction involving the S-N bond cleavage which can limit the reductive window according to the reaction below:

$$(CF_3SO_2)_2N^- + e^- \rightarrow \bullet NSO_2CF_3^- + SO_2CF_3^-$$

Finally, $[PF_6]^-$ and $[BF_4]^-$ are susceptible to undergo hydrolysis releasing toxic HF gas.[46] The approximate trend in decreasing the anodic limit follows the order: $[FAP]^- > [NTf_2]^- > [BF_4]^- > [PF_6]^- > X^-$ (where X = halide) .[25]

2.1.2 The Effect of Impurities

The purity of RTILs should be considered when they are used as electrochemical solvents. Any presence of impurities in the RTILs affects the physical properties and has significant influence to the electrochemical signal of a system under investigation. Three main impurities that usually present in RTILs are water, dissolved gases and residues from the synthesis such as halide.[44]

The RTILs used for the work in this thesis are considered to be air and water stable. This means that they do not undergo hydrolysis with water unlike their haloaluminate relatives which make them difficult to handle. However, moisture from air still can be absorbed by even hydrophobic RTILs such as $[P_{14,6,6,6}][FAP]$ and $[C_4mpyrr][NTf_2]$.[21,47,48] The presence of water in the RTILs is found to decrease the viscosity[24,49], to increase the conductivity and to reduce electrochemical windows quite significantly.[3]

Widegreen et. al.[49] studied the effect of dissolved water on the viscosities of three hydrophobic RTILs. The viscosities of all RTILs decrease dramatically with increasing water content. $[C_4mim][PF_6]$ experiences a large change with a 17% decrease in its viscosity when 0.19% water is added. The change in viscosity in turn leads to a change in other properties such as conductivity and diffusivity of dissolved species under investigation. Schrőder et. al[50] have investigated the effect of water content on ion diffusivity in RTILs. The diffusion coefficient of *N,N,N',N'*-tetramethyl-paraphenylenediamine (TMPD) and methylviologen were investigated under water-saturated RTILs. The results show that the diffusion coefficient of TMPD is doubled in RTILs containing approximately 5% water. Dramatic changes in diffusion coefficient are also reported with an order of magnitude increase for methylviologen.[50]

The effect of water on the electrochemical window of RTILs was also studied.[21,24,50] It is reported that the addition of more than 3% of water to both $[C_4mim][PF_6]$ and $[C_4mim][BF_4]$ shrinks their electrochemical windows up to 2 V. An in depth study regarding this topic was conducted by O'Mahony et. al.[21] Current densities of 1 mA cm^{-2} and 5 mA cm^{-2} were applied to define the limit for the electrochemical window. For all twelve RTILs under investigation, the presence of water narrowed their cathodic and anodic limits. The variation of water uptake determined by Karl-Fisher titration was influenced by the identity of anions and the hydrophobicity following the trend: $[FAP]^- > [NTf_2]^- > [PF_6]^- > [BF_4]^- > [OTf]^-$ > halides.[21] This report also suggests the importance of purging the ionic liquids under vacuum prior to electrochemical use to remove the water content.

Together with water, oxygen gas can also be absorbed by RTILs from air. Oxygen is electrochemically active and can be reduced to superoxide at -1.5 V (vs Ag).[51,52] Its presence obviously will distort the electrochemical signal[44,51-54] of systems that appear

at relatively more negative potentials such as deposition and stripping processes of alkali metal redox couples. Therefore it is necessary to remove the gas prior to electrochemical measurements. Methods of oxygen removal include inert gas bubbling or blanketing (N_2 or Ar)[55] as well as purging under vacuum.[50,56] However, recent studies also conducted by the Compton Group suggest that the presence of 1 atm argon increases the diffusion coefficient of ferrocene due to the decrease in the viscosity of RTILs.[57] Therefore, purging under vacuum prior to electrochemical measurement is effective in removing oxygen and water from RTILs whilst maintaining the electrochemical properties of RTILs. This method of removing water and oxygen impurities applies a novel specially designed T-Cell which requires only a small amount of RTILs allowing purification in a reasonable time.[50,56]

The other major impurities which can be present are halide impurities. They arise in RTILs from the preparation which involves halide precursors. Often organic chlorides or bromides salts (alkyl halides) are used in alkylation to form the precursor. The presence of halide impurities is found to increase the viscosity[47] as well as narrowing the electrochemical window of RTILs. A report suggests that chloride impurities can decrease the anodic limit of RTILs up to 0.9 V.[58] In addition, chloride and bromide are easily oxidised at low potential a process which could interfere the electrochemical signal of system under investigation. The ease of chloride and bromide oxidation becomes a potential method to remove them from the RTILs. [46,59,60]

2.1.3 Electrodeposition in Ionic Liquids

2.1.3.1 Reactive Metals

Reactive metals such as Alkali Group I metals cannot be electrodeposited from aqueous solution. These metals have very negative electrode potentials, for example -3.04 V [61]

and -2.71 V[61] versus SHE for lithium and sodium respectively. Lithium and sodium industrially are produced through electrolysis of their molten salts. This method of production requires a lot of energy since it is performed at high temperature. It also produces harmful by products such as chlorine gas.

In order to reduce the cost of production, scientists have proposed methods to electrodeposit the reactive metals by using haloaluminate based ionic liquids and relatively mild conditions. Haloaluminate based ionic liquids are the first generation of ionic liquids.[2] They are easy to synthesize, usually by addition of the Lewis acid $AlCl_3$ to an organic salt such 1,3-dialkyl imidazolium, alkyl-pyrridinium or quaternary ammonium salt under an inert atmosphere.[62] The acidity of this ionic liquid can be adjusted according to the molar ratio of $AlCl_3$ and the organic salt (Lewis base). Moreover, addition of neutral salt (NaCl) to the composition buffers the liquids.

Lipsztajn and Osteryoung first demonstrated the electrodeposition of lithium from $[C_2mim][Cl]/AlCl_3$ ionic liquid.[62] They used LiCl as a source of lithium and dissolved it in slightly neutral acidic $[C_2mim][Cl]/AlCl_3$ to form $LiAlCl_4$ in a neutral melt. These neutral ionic liquids provide a wider electrochemical window compared to the acidic one so that lithium metal could be electrodeposited on tungsten, glassy carbon and aluminium electrodes. It is also reported that the diffusion coefficient of Li^+ in $[C_2mim][Cl]/AlCl_3$ ionic liquid was determined using a W-rotating disk electrode with the value of $8.6 \pm 0.3 \times 10^{-7}$ cm^2 s^{-1}. The ability of the haloaluminate system as a medium to electrodeposit Li metal was also exploited by other researchers.[63,64] Carlin and Scordilis-Kelly[63] showed that the addition of protons (HCl) to the $[C_2mim][Cl]/AlCl_3$ system widened the electrochemical window allowing lithium electrodeposition with stripping efficiency reaching 80%. However, the stability of the medium is limited by the rapid loss of HCl gas. Then, Piersma *et al.*[64] replaced the use

of HCl with triethanolamine.hydrogen chloride in the system. The new proton source was found to widen the electrochemical window thus allowing the deposition of both sodium and lithium. It is also reported that the new system was stable for months.

The study of sodium electrodeposition in this type of ionic liquid has been reported.[65-68] Instead of using LiCl to control the acidity of the ionic liquids, NaCl was added to system not only to neutralise the C_2mimCl/$AlCl_3$ but also as a source of sodium. Additives such as gaseous HCl[66], triethanolamine hydrochloric[68] or $SOCl_2$[69] were introduced into the system in order for Na/Na^+ redox couple to be observed. It is thought that the additives act as a Lewis acid and weaken the interaction between Na^+ and $AlCl_4^-$ ions. The scheme below display the proposed interactions.[69]

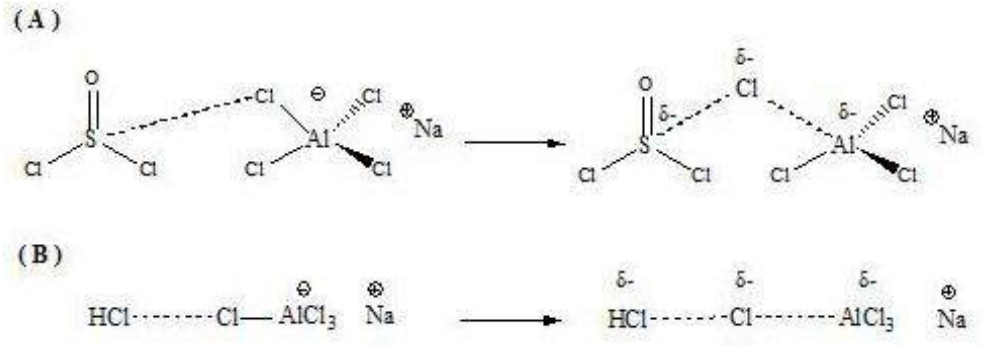

Figure 2. 1: Proposed interaction between additives and $NaAlCl_4$[69]

Although chloroaluminate based ionic liquids provide alternatives as media for electrodeposition for some reactive metals as explained before, they also have disadvantages. The main disadvantages are their corrosiveness as well as instability against air and moisture. The development in chemical synthesis has led to the preparation of air- and water-stable ionic liquids which can be applied as media for electrodeposition of some reactive metals. Howlett et. al.[26] reported that [$C_n$mpyrr][NTf_2] ionic liquids (where n = 3 and 4) allow the lithium to be cycled with a

high degree of reversibility and high (99%) stripping efficiency was achieved. The morphology of the deposit was also found to be uniform at moderate current densities. Various phosphonium ionic liquids with $[NTf_2]^-$ anion also have been demonstrated to allow the deposition and stripping of lithium metal on a nickel electrode.[70] The cathodic and anodic peaks for Li/Li^+ couple were observed at approximately -3.1 V versus Fc/Fc^+. The results were compared when corresponding tertiary ammonium ionic liquids were used. It is found that the stripping efficiency of lithium deposition dissolution process in phosphonium based ionic liquids is higher than that in corresponding ammonium ionic liquids. More recent and similar work has also been reported by another group.[71] Meanwhile, new family members of air and water stable ionic liquids which can support lithium deposition-stripping processes have been prepared in various laboratories.[72,73]

2.1.3.2 Unreactive Metals

Unlike reactive metals, less reactive metals can be electrodeposited from aqueous solutions. Electrodeposition of these metals can also be performed in RTILs. There are several advantages of using RTILs as media for electrodeposition over the aqueous media. RTILs is considered to be less toxic solvent compared to aqueous media for plating which usually contains poisonous additives such as cyanide. The fact that RTILs have near zero vapour pressure meaning the electrodeposition can be performed in open electrodeposition baths without releasing harmful vapours. Moreover, since the RTILs are relatively stable at high temperature, subsequent annealing can be avoided and electrodeposition process can be conducted directly. Another advantage of using RTILs is the absence hydrogen evolution which causes embrittlement on the electrodeposit.

Many publications have reported the use of RTILs in the electrodeposition of less reactive metals such as zinc[74-76], copper[77,78], chromium[79,80], silver[81-83], and tin[84,85].

2.2 Introduction to X-Ray Photoelectron Spectroscopy

X-ray photoelectron spectroscopy involves irradiating usually solid samples in *vacuo* with X-ray photons and measuring the kinetic energy of the electrons emitted. This technique is very sensitive to determine both qualitatively and quantitatively the elements at surfaces under ultra high vacuum conditions. For the development of this technique, Kai Siegbahn has awarded the Noble Price for Physics in 1981.[86] Currently, XPS is a widely utilised technique both in research as well as in industry in the areas of catalysis, microelectronics, corrosion, metallurgy as well as in polymer technology. Since ionic liquid has nearly zero vapour pressure, it is possible to conduct XPS experiments.[87-91] The combination of zero vapour pressure and wide electrochemical windows of the RTILs, makes the combined XPS-electrochemistry technique potentially powerful.[92-94]

2.2.1 Principle of X-ray Photoelectron Spectroscopy

The basic principle of XPS relies on the photoelectric effect elaborated firstly by Einstein in 1905.[95] The sample is bombarded by photons so that electrons at the core levels are ejected. Then the energy of the photoemitted electrons is analysed by the electron spectrometer. The ingoing photons penetrate the sample in the order of micrometers; the ejected electrons have a much shorter inelastic mean free path. This

makes XPS a surface sensitive technique. The emitted electrons from the uppermost few nanometres of the sample can escape the surface without energy loss. These electrons contribute the characteristic peaks in the spectrum. Meanwhile, the electrons that experience inelastic scattering and therefore lose their energy contribute to the background of the spectrum. The photoemission process is presented in Figure 2. 2

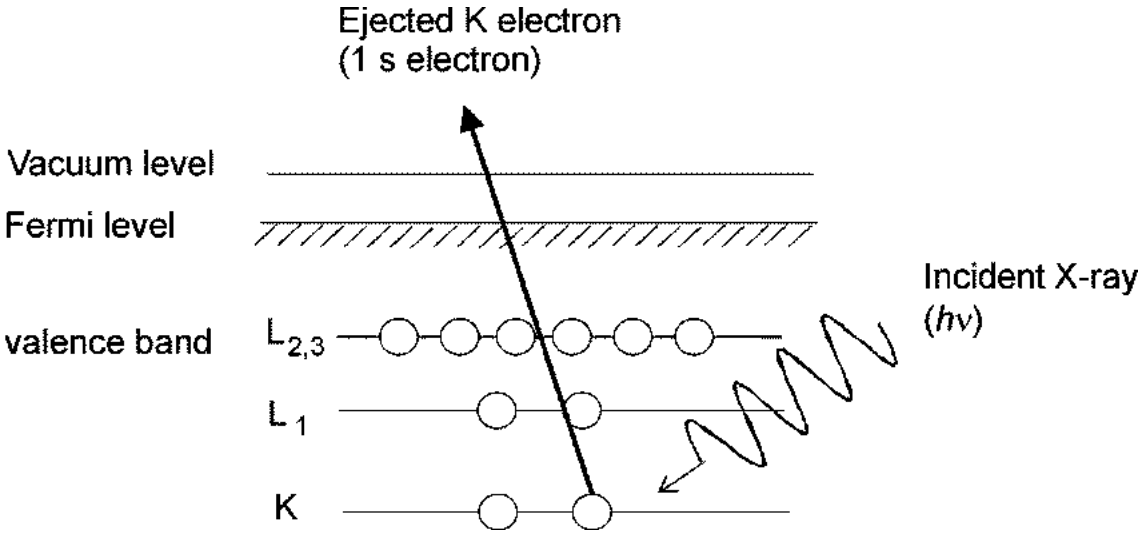

Figure 2. 2 Schematic diagram of XPS process, showing photoionisation of an atom by the ejection of a 1s electron

The emitted electrons that do not undergo inelastic scattering have characteristic kinetic energy (KE) which is defined by Einstein according to equation:

$$KE = h\nu - BE \tag{2.4}$$

where $h\upsilon$ is the energy of the incident photon and *BE* is the binding energy of the atomic orbital from which the excited electron originated. The kinetic energy of the electron is the experimental quantity measured by the spectrometer, but this is dependent on the photon energy of the X-rays used so that this is not specific to the material property. On the other hand, the binding energy is the parameter that identifies electron specifically, both the element from which it originates and the atomic energy level. Therefore the binding energy can be used for qualitative analysis of the sample.

The binding energy can also be defined as the energy difference between the initial and final state after the photoelectron has left the atom.

The technique employs X-ray for the incident irradiating photons. X-rays are produced through the bombardment of an anode material with high energy electrons which are emitted from thermal source (electrically heated tungsten filament). The most commonly used anode material for XPS are Mg and Al which yield the corresponding Mg Kα and Al Kα radiations with energy 1253.6 eV and 1486.6 eV respectively. Prior to irradiation, the x-ray must go through an appropriate monochromator to reduce the line width of the x-ray source. Radiation from synchrotron is also commonly used. Synchrotron provides a wide range of photon energies, from ultra-violet to hard X-rays. The synchrotron based XPS offers a lot of advantages such as higher energy resolution, well-defined polarisation, higher photon flux and a higher photoemission cross section.

In order for the ejected electron to be analysed, an ultra-high vacuum (UHV) environment is required. Generally, the pressure in the XPS chamber is in the range between 10^{-8} and 10^{-10} mbar. There are three reasons why an UHV environment is required. First, the ejected electron from the surface should travel to the analyser without any interference from gas phase collisions to maintain its energy. Collisions with gas phase scatter the electrons and change their energy. This is very important when analysing the low-energy electrons which are easily scattered by gas molecules leading to a decreased spectral intensity and increasing the noise. Secondly, under the UHV environment, the adsorption rate of molecules on the surface from the residual gas is very low. Consequently, a freshly cleaned surface remains at a low contamination level for a sufficient time to analyse the photoemitted electrons. Finally, under UHV conditions, dissolved impurities such as gases and water can be evacuated to a large

extent. This is very relevant in the case of RTILs where such impurities are easily removed under vacuum.

2.2.2 Qualitative Analysis

Since the binding energy parameter is an intrinsic property of the material studied, the XPS spectrum provides information for the identification of elements present at surfaces. In order the get this information, a survey scan spectrum is recorded over a region that provides strong peaks for the elements. A binding energy region between 0 and 1000 eV[96] is usually enough for this purpose. Then the binding energy of the individual peak is compared to the data in tabular form to identify the elements present in the sample.

2.2.3 Quantitative Analysis

Based on the fact that the intensity of the photoemitted electron peaks relates to the concentration of the elements present at surface, XPS spectra can also provide quantitative information regarding the surface composition. Mathematically, the intensity (I) of a photoelectron peak is given by[86,96]:

$$I = J\rho\sigma K\lambda \tag{2.5}$$

where J is the photon flux, ρ is the concentration of atom or ion in the sample, σ is the cross section for photoelectron production, K is a term which covers all the instrumental factors and λ is the electron attenuation length. In order to simplify and to use directly the equation 2.5 for quantification, a term sensitivity factor (SF) for different elements is introduced. This term includes σ, K, and λ as an approach. Actually the SF is determined empirically through experiment as developed by Wagner et. al.[97] If the X-

ray flux remains constant during the experiment the atomic concentration (in percentage) can be determined by dividing the intensity (in the form of peak area) by the SF. The atomic concentration is expressed as a fraction of the summation of all normalised intensities according to equation:

$$[A]atomic\,\% = \frac{{}^{I_A}/_{SF_A}}{\hat{a}({}^{I}/_{SF})} x100\% \tag{2.6}$$

References

(1) Malhotra, S. J. *Ionic Liquid Applications: Pharmaceuticals, Therapeutics, and Biotechnology*; American Chemical Society: Washington DC, 2010.

(2) Freemantle, M. *Itroduction to Ionic Liquids*; The Royal Society of Chemistry: Cambridge, 2009.

(3) Hapiot, P.; Lagrost, C. *Chem. Rev.* **2008**, *108*, 2238-2264.

(4) Welton, T. *Chem. Rev.* **1999**, *99*, 2071-2083.

(5) Hurley, F. H.; Wier, T. P. *J. Electrochem. Soc.* **1951**, *98*, 203-206.

(6) Zaworotko, M. J.; Wilkes, J. S. *Abstr. Pap. Am. Chem. Soc.* **1992**, *203*, 201-INOR.

(7) Shvedene, N. V.; Chernyshov, D. V.; Pletnev, I. V. *Russ. J. Gen. Chem.* **2008**, *78*, 2507-2520.

(8) Visser, A. E.; Swatloski, R. P.; Reichert, W. M.; Mayton, R.; Sheff, S.; Wierzbicki, A.; Davis, J. H.; Rogers, R. D. *Chem. Commun.* **2001**, 135-136.

(9) Bonhote, P.; Dias, A. P.; Papageorgiou, N.; Kalyanasundaram, K.; Gratzel, M. *Inorg. Chem.* **1996**, *35*, 1168-1178.

(10) Okutoro, O. O.; VanderNoot, T. J. *Journal Of Electroanalytical Chemistry* **2004**, *568*, 167.

(11) Ignat'ev, N. V.; Welz-Biermann, U.; Kucheryna, A.; Bissky, G.; Willner, H. *J. Fluor. Chem.* **2005**, *126*, 1150-1159.

(12) Sun, J.; Forsyth, M.; MacFarlane, D. R. *Journal Of Physical Chemistry B* **1998**, *102*, 8858-8864.

(13) Seddon, K. R.; Stark, A.; Torres, M. J. In *Clean Solvents: Alternative Media for Chemical Reactions and Processing*; Abraham, M. A., Moens, L., Eds.; Amer Chemical Soc: Washington, 2002; Vol. 819; pp 34-49.

(14) Del Sesto, R. E.; Corley, C.; Robertson, A.; Wilkes, J. S. *J. Organomet. Chem.* **2005**, *690*, 2536-2542.

(15) obtained from http://www.merck-chemicals.com/ionic-liquids /c_g1ib.s1Lhu4AAAEWqOEfVhTl , official merck webite for ionic liquids.

(16) Huddleston, J. G.; Visser, A. E.; Reichert, W. M.; Willauer, H. D.; Broker, G. A.; Rogers, R. D. *Green Chem.* **2001**, *3*, 156-164.

(17) *Handbook of Chemistry and Physics: 76th Edition*; Lide, D. R., Ed.; CRC Press: Boca Raton, USA, 1996.

(18) Wang, Y. D.; Zaghib, K.; Guerfi, A.; Bazito, F. F. C.; Torresi, R. M.; Dahn, J. R. *Electrochim. Acta* **2007**, *52*, 6346-6352.

(19) MacFarlane, D. R.; Meakin, P.; Sun, J.; Amini, N.; Forsyth, M. *Journal Of Physical Chemistry B* **1999**, *103*, 4164-4170.

(20) Olivier-Bourbigou, H.; Magna, L. *J. Mol. Catal. A-Chem.* **2002**, *182*, 419-437.

(21) O'Mahony, A. M.; Silvester, D. S.; Aldous, L.; Hardacre, C.; Compton, R. G. *J. Chem. Eng. Data* **2008**, *53*, 2884-2891.

(22) Bard, A. J.; Faulkner, L. R. *Electrochemical Methods: Fundamentals and Applications*; 2nd ed.; John Wiley and Sons: New York, 2001.

(23) Every, H.; Bishop, A. G.; Forsyth, M.; MacFarlane, D. R. *Electrochim. Acta* **2000**, *45*, 1279-1284.

(24) Fitchett, B. D.; Knepp, T. N.; Conboy, J. C. *J. Electrochem. Soc.* **2004**, *151*, E219-E225.

(25) Buzzeo, M. C.; Evans, R. G.; Compton, R. G. *ChemPhysChem* **2004**, *5*, 1106-1120.

(26) Howlett, P. C.; MacFarlane, D. R.; Hollenkamp, A. F. *Electrochem. Solid State Lett.* **2004**, *7*, A97-A101.

(27) Forsyth, C. M.; MacFarlane, D. R.; Golding, J. J.; Huang, J.; Sun, J.; Forsyth, M. *Chem. Mat.* **2002**, *14*, 2103-2108.

(28) MacFarlane, D. R.; Sun, J.; Golding, J.; Meakin, P.; Forsyth, M. *Electrochim. Acta* **2000**, *45*, 1271-1278.

(29) Vila, J.; Gines, P.; Rilo, E.; Cabeza, O.; Varela, L. M. *Fluid Phase Equilib.* **2006**, *247*, 32-39.

(30) Stolwijk, N. A.; Obeidi, S. *Electrochim. Acta* **2009**, *54*, 1645-1653.

(31) Tsuzuki, S.; Tokuda, H.; Hayamizu, K.; Watanabe, M. *Journal Of Physical Chemistry B* **2005**, *109*, 16474-16481.

(32) Fischer, L.; Falta, T.; Koellensperger, G.; Stojanovic, A.; Kogelnig, D.; Galanski, M.; Krachler, R.; Keppler, B. K.; Hann, S. *Water research* **2011**, *45*, 4601-14.

(33) Garcia, S.; Garcia, J.; Larriba, M.; Torrecilla, J. S.; Rodriguez, F. *J. Chem. Eng. Data* **2011**, *56*, 3188-3193.

(34) Rogers, R. D.; Seddon, K. R. *Science* **2003**, *302*, 792-793.

(35) Earle, M. J.; Esperanca, J.; Gilea, M. A.; Lopes, J. N. C.; Rebelo, L. P. N.; Magee, J. W.; Seddon, K. R.; Widegren, J. A. *Nature* **2006**, *439*, 831-834.

(36) Fraser, K. J.; Izgorodina, E. I.; Forsyth, M.; Scott, J. L.; MacFarlane, D. R. *Chem. Commun.* **2007**, 3817-3819.

(37) Jacquemin, J.; Husson, P.; Padua, A. A. H.; Majer, V. *Green Chem.* **2006**, *8*, 172-180.

(38) Dzyuba, S. V.; Bartsch, R. A. *ChemPhysChem* **2002**, *3*, 161-166.

(39) Ohno, H. in *Electrodeposition from Ionic Liquids*; Endres, F., MacFarlane, D. R., Abbott, A. P., Eds.; Wiley-VCH Verlag GmbH & Co. KHaA: Weinheim, 2008.

(40) Gu, Z. Y.; Brennecke, J. F. *J. Chem. Eng. Data* **2002**, *47*, 339-345.

(41) Suarez, P. A. Z.; Consorti, C. S.; de Souza, R. F.; Dupont, J.; Goncalves, R. S. *J. Braz. Chem. Soc.* **2002**, *13*, 106-109.

(42) Rogers, E. I.; Sljukic, B.; Hardacre, C.; Compton, R. G. *J. Chem. Eng. Data* **2009**, *54*, 2049-2053.

(43) Suarez, P. A. Z.; Selbach, V. M.; Dullius, J. E. L.; Einloft, S.; Piatnicki, C. M. S.; Azambuja, D. S.; deSouza, R. F.; Dupont, J. *Electrochim. Acta* **1997**, *42*, 2533-2535.

(44) Buzzeo, M. C.; Hardacre, C.; Compton, R. G. *ChemPhysChem* **2006**, *7*, 176-180.

(45) Howlett, P. C.; Izgorodina, E. I.; Forsyth, M.; MacFarlane, D. R. *Z. Phys. Chemie-Int. J. Res. Phys. Chem. Chem. Phys.* **2006**, *220*, 1483-1498.

(46) Xiao, L.; Johnson, K. E. *J. Electrochem. Soc.* **2003**, *150*, E307-E311.

(47) Seddon, K. R.; Stark, A.; Torres, M. J. *Pure Appl. Chem.* **2000**, *72*, 2275-2287.

(48) Cammarata, L.; Kazarian, S. G.; Salter, P. A.; Welton, T. *Phys. Chem. Chem. Phys.* **2001**, *3*, 5192-5200.

(49) Widegren, J. A.; Laesecke, A.; Magee, J. W. *Chem. Commun.* **2005**, 1610-1612.

(50) Schroder, U.; Wadhawan, J. D.; Compton, R. G.; Marken, F.; Suarez, P. A. Z.; Consorti, C. S.; de Souza, R. F.; Dupont, J. *New J. Chem.* **2000**, *24*, 1009-1015.

(51) Rogers, E. I.; Huang, X. J.; Dickinson, E. J. F.; Hardacre, C.; Compton, R. G. *J. Phys. Chem. C* **2009**, *113*, 17811-17823.

(52) Huang, X. J.; Rogers, E. I.; Hardacre, C.; Compton, R. G. *Journal Of Physical Chemistry B* **2009**, *113*, 8953-8959.

(53) Evans, R. G.; Klymenko, O. V.; Saddoughi, S. A.; Hardacre, C.; Compton, R. G. *Journal Of Physical Chemistry B* **2004**, *108*, 7878-7886.

(54) Buzzeo, M. C.; Klymenko, O. V.; Wadhawan, J. D.; Hardacre, C.; Seddon, K. R.; Compton, R. G. *Journal Of Physical Chemistry A* **2003**, *107*, 8872-8878.

(55) *Electrochemical Aspects of Ionic Liquids*; Matsumoto, H., Ed.; John Wiley & Sons: Hoboken, NJ, 2005.

(56) Evans, R. G.; Klymenko, O. V.; Price, P. D.; Davies, S. G.; Hardacre, C.; Compton, R. G. *ChemPhysChem* **2005**, *6*, 526-533.

(57) Barrosse-Antle, L. E.; Aldous, L.; Hardacre, C.; Bond, A. M.; Compton, R. G. *J. Phys. Chem. C* **2009**, *113*, 7750-7754.

(58) Aldous, L.; Silvester, D. S.; Villagran, C.; Pitner, W. R.; Compton, R. G.; Lagunas, M. C.; Hardacre, C. *New J. Chem.* **2006**, *30*, 1576-1583.

(59) Li, Z. P.; Du, Z. Y.; Gu, Y. L.; Zhu, L. Y.; Zhang, X. P.; Deng, Y. Q. *Electrochem. Commun.* **2006**, *8*, 1270-1274.

(60) Villagran, C.; Banks, C. E.; Hardacre, C.; Compton, R. G. *Anal. Chem.* **2004**, *76*, 1998-2003.

(61) Smith, E. R.; Taylor, J. K. *Journal of Research of the National Bureau of Standards (United States)* **1940**, *25*, 731-746.

(62) Lipsztajn, M.; Osteryoung, R. A. *Inorg. Chem.* **1985**, *24*, 716-719.

(63) Scordiliskelley, C.; Carlin, R. T. *J. Electrochem. Soc.* **1994**, *141*, 873-875.

(64) Piersma, B. J.; Ryan, D. M.; Schumacher, E. R.; Riechel, T. L. *J. Electrochem. Soc.* **1996**, *143*, 908-913.

(65) Gray, G. E.; Kohl, P. A.; Winnick, J. *J. Electrochem. Soc.* **1995**, *142*, 3636-3642.

(66) Gray, G. E.; Winnick, J.; Kohl, P. A. *J. Electrochem. Soc.* **1996**, *143*, 2262-2266.

(67) Gray, G. E.; Winnick, J.; Kohl, P. A. *J. Electrochem. Soc.* **1996**, *143*, 3820-3824.

(68) Riechel, T. L.; Wilkes, J. S. *J. Electrochem. Soc.* **1993**, *140*, 3104-3107.

(69) Kim, K.; Lang, C.; Kohl, P. A. *J. Electrochem. Soc.* **2005**, *152*, E9-E13.

(70) Tsunashima, K.; Sugiya, M. *Electrochem. Solid State Lett.* **2008**, *11*, A17-A19.

(71) Vega, J. A.; Zhou, J. F.; Kohl, P. A. *J. Electrochem. Soc.* **2009**, *156*, A253-A259.

(72) Ruther, T.; Huang, J.; Hollenkamp, A. F. *Chem. Commun.* **2007**, 5226-5228.

(73) Yoshizawa-Fujita, M.; MacFarlane, D. R.; Howlett, P. C.; Forsyth, M. *Electrochem. Commun.* **2006**, *8*, 445-449.

(74) Borissov, D.; Pareek, A.; Renner, F. U.; Rohwerder, M. *Phys. Chem. Chem. Phys.* **2010**, *12*, 2059-2062.

(75) Simka, W.; Puszczyk, D.; Nawrat, G. *Electrochim. Acta* **2009**, *54*, 5307-5319.

(76) Yamamoto, H.; Kinoshita, H.; Kimura, M.; Shirai, H.; Koyama, K. *Electrochemistry* **2006**, *74*, 370-373.

(77) Ben Assaker, I.; Dhahbi, M. *J. Mol. Liq.* **2011**, *161*, 13-18.

(78) Brooks, N. R.; Schaltin, S.; Van Hecke, K.; Van Meervelt, L.; Binnemans, K.; Fransaer, J. *Chem.-Eur. J.* **2011**, *17*, 5053-5058.

(79) Surviliene, S.; Eugenio, S.; Vilar, R. *J. Appl. Electrochem.* **2011**, *41*, 107-114.

(80) Abbott, A. P.; Capper, G.; Davies, D. L.; Rasheed, R. K.; Archer, J.; John, C. *Trans. Inst. Metal Finish.* **2004**, *82*, 14-17.

(81) Rogers, E. I.; Silvester, D. S.; Jones, S. E. W.; Aldous, L.; Hardacre, C.; Russell, A. J.; Davies, S. G.; Compton, R. G. *J. Phys. Chem. C* **2007**, *111*, 13957-13966.

(82) Basile, A. B. A.; Bhatt, A. I.; O'Mullane, A. P.; Bhargava, S. K. *Electrochim. Acta* **2011**, *56*, 2895-2905.

(83) Serizawa, N.; Katayama, Y.; Miura, T. *Electrochim. Acta* **2010**, *56*, 346-351.

(84) Tachikawa, N.; Serizawa, N.; Katayama, Y.; Miura, T. *Electrochim. Acta* **2008**, *53*, 6530-6534.

(85) Yang, W. Z.; Cang, H.; Tang, Y. M.; Wang, J. T.; Shi, Y. X. *J. Appl. Electrochem.* **2008**, *38*, 537-542.

(86) Briggs, D.; Grant, J. T. *Surface Analysis by Auger and X-Ray Photoelectron Spectroscopy*; IM Publication: Chichester, 2003.

(87) Qiu, F. L.; Taylor, A. W.; Men, S.; Villar-Garcia, I. J.; Licence, P. *Phys. Chem. Chem. Phys.* **2010**, *12*, 1982-1990.

(88) Hashimoto, H.; Ohno, A.; Nakajima, K.; Suzuki, M.; Tsuji, H.; Kimura, K. *Surf. Sci.* **2010**, *604*, 464-469.

(89) Smith, E. F.; Villar Garcia, I. J.; Briggs, D.; Licence, P. *Chem. Commun.* **2005**, 5633-5635.

(90) Smith, E. F.; Rutten, F. J. M.; Villar-Garcia, I. J.; Briggs, D.; Licence, P. *Langmuir* **2006**, *22*, 9386-9392.

(91) Silvester, D. S.; Broder, T. L.; Aldous, L.; Hardacre, C.; Crossley, A.; Compton, R. G. *Analyst* **2007**, *132*, 196-198.

(92) Licence, P.; Jones, R. G.; Smith, E. F.; Garcia, I. J. V. *Abstr. Pap. Am. Chem. Soc.* **2008**, *236*.

(93) Wibowo, R.; Aldous, L.; Jacobs, R. M. J.; Manan, N. S. A.; Compton, R. G. *Chem. Phys. Lett.* **2011**, *509*, 72-76.

(94) Villar-Garcia, I. J.; Smith, E. F.; Taylor, A. W.; Qiu, F. L.; Lovelock, K. R. J.; Jones, R. G.; Licence, P. *Phys. Chem. Chem. Phys.* **2011**, *13*, 2797-2808.

(95) Lovelock, K. R. J.; Villar-Garcia, I. J.; Maier, F.; Steinruck, H. P.; Licence, P. *Chem. Rev.* **2010**, *110*, 5158-5190.

(96) Watts, J. F.; Wolstenholme, J. *An Introduction to Surface Analysis by XPS and AES*; John Wiley and Sons Ltd.: Chichester, Sussex, 2003.

(97) Wagner, C. D.; Davis, L. E.; Zeller, M. V.; Taylor, J. A.; Raymond, R. H.; Gale, L. H. *Surf. Interface Anal.* **1981**, *3*, 211-225.

Chapter 3
General Experimental Methods

This Chapter presents the general experimental methods used in the thesis which includes chemicals, instrumentations and experimental procedures employed.

3.1 Chemicals

Table 3. 1 lists the chemical used in the thesis which are used as received without any further purifications.

Table 3. 1: List of chemical reagents for experiments

Name	Formula / Abreviation	Supplier	Purity
Ferrocene	$Fe(C_5H_5)_2$	Aldrich	98%
Tetra-n-butyl ammonium perchlorate	TBAP	Aldrich	>99%
Acetonitrile	MeCN	Fisher Sci.	>99.99%
Lithium hexafluoroarsenate	$LiAsF_6$	Aldrich	98%
Bis(trifluoromethylsulfonyl)imide acid	$HNTf_2$	Sigma	95%
Sodium hydroxide	NaOH	Aldrich	>97%
Potassium hydroxide	KOH	Aldrich	>95%
Rubidium hydroxide hydrate	$RbOH.H_2O$	Aldrich	>99%
Caesium hydroxide monohydrate	$CsOH.H_2O$	Aldrich	≥99.5%

The room temperature ionic liquids used in this thesis are listed in Table 3. 1and the structure of the cations and the anions are shown in Figure 3. 1. $[C_4mim][OTf]$, $[C_4mim][PF_6]$ and $[P_{14,6,6,6}][FAP]$ where kindly donated by Merck KGaA while all other ionic liquids used were obtained from Queens University Ionic Liquid Laboratry (QUILL), Belfast having been prepared using standard literature procedures.[1]

Table 3. 2 Room Temperature Ionic Liquids used in this thesis

Name	Abreviation	Supplier
N-Butyl-N-methylpyrrolidinium bis(trifluoromethylsulfonyl)imide	$[C_4mpyrr][NTf_2]$	QUILL
1-Butyl-2,3-dimethylimidazolium	$[C_4dmim][NTf_2]$	QUILL

bis(trifluoromethylsulfonyl)imide		
N-Ethyldimethylpropylammonium bis(trifluoromethylsulfonyl)imide	$[N_{2,1,1,3}][NTf_2]$	QUILL
N-Hexyltriethylammonium bis(trifluoromethylsulfonyl)imide	$[N_{6,2,2,2}][NTf_2]$	QUILL
1-Butyl-3-methylimidazolium bis(trifluoromethylsulfonyl)imide	$[C_4mim][NTf_2]$	QUILL
1-Ethyl-3-methylimidazolium bis(trifluoromethylsulfonyl)imide	$[C_2mim][NTf_2]$ $[C_4pyr][NTf_2]$	QUILL
N-Butylpyridinium bis(trifluoromethylsulfonyl)imide	$[C_4mpyrr][N(CN)_2]$	QUILL
N-Butyl-N-methylpyrrolidinium dicynamide	$[C_4mim][OTf]$	QUILL
1-Butyl-3-methylimidazolium trifluomethylsulfonate	$[N_{1,8,8,8}][OTf]$	Merck KGaA
N-methyltrioctyl trifluomethylsulfonate	$[C_4mim][PF_6]$	QUILL
1-Butyl-3-methylimidazolium hexafluorophosphate	$[C_4mim][BF_4]$	Merck KGaA
1-Butyl-3-methylimidazolium tetrafluoroborate	$[P_{14,6,6,6}][FAP]$	Merck KGaA
Tris(P-hexyl)tetradecylphosphonium tris(pentafluoroethyl)trifluorophosphate		Merck KGaA

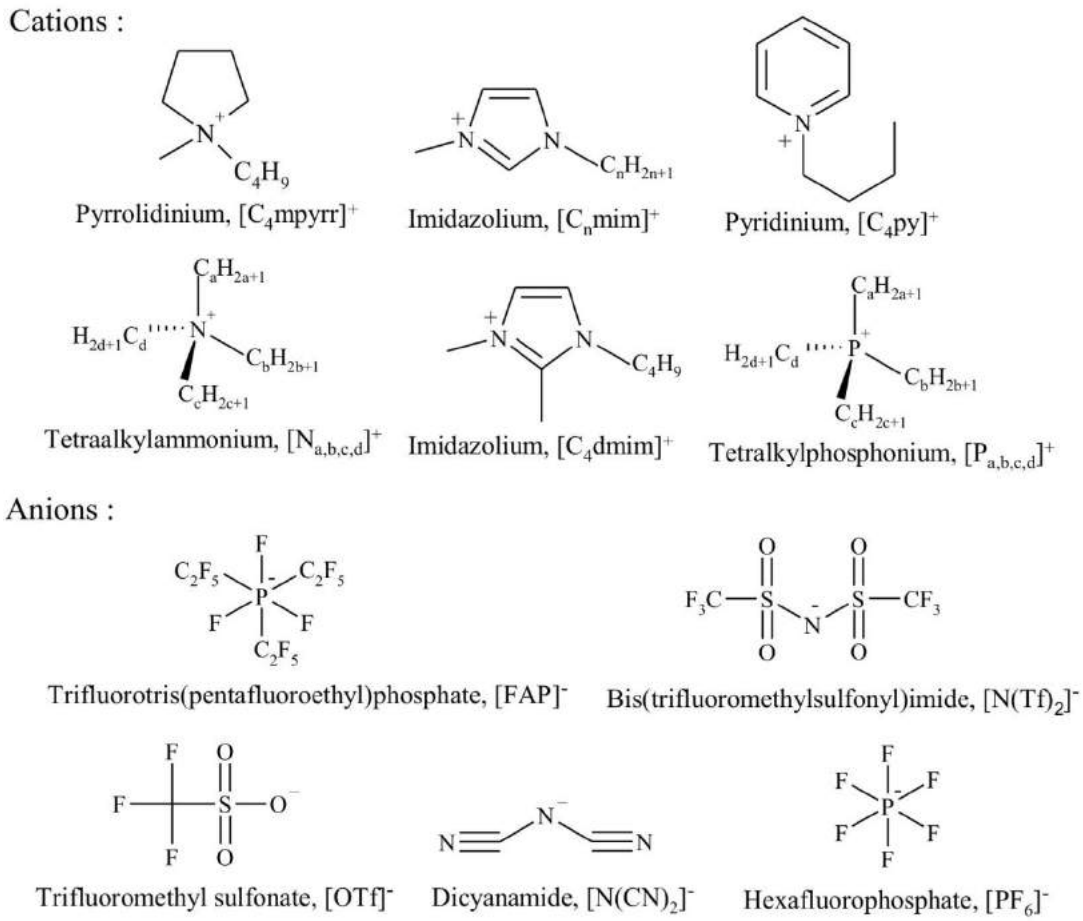

Figure 3. 1: The structure of the cations and anions of RTILs used in this thesis.

3.2 Sample preparation

The salts of alkali metal bis(trifluoromethylsulfonyl)imide (M[NTf_2] where M = Na, K, Rb and Cs) were prepared by the reaction of aqueous solutions of the appropriate metal hydroxide salt with the 5% molar excess of H[NTf_2]. After the reaction was complete, the resulting solutions were dried using a rotary evaporator and the residues were further dried under vacuum for 24 hours. In order to reach pH neutral, repeated dissolution in water then drying under vacuum treatment were performed. The resulting salts were ready to be dissolved in ionic liquids.

3.3 Instrumentations and Procedures

3.3.1 Electrochemistry

All electrochemical measurements were carried out using a computer-controlled μ-Autolab potentiostat (Eco-Chemie, Netherlands). Voltammetric measurements were conducted by applying a conventional two-electrode arrangement with either a platinum (10 μm diameter, Cypress Systems, Kansas) or a nickel (50 μm diameter, fabricated in house) microelectrode used as a working electrode. A silver wire (Advent Research Materials Ltd., UK, 99.99%) served as a quasi-reference electrode. A section of a disposable micropipette tip (Eppendorf, Germany) was placed on the top of the working electrode, into which 20μL of an ionic liquid solution containing 10 mM ferrocene and 0.1 M $LiAsF_6$ or 0.1 M $M[NTf_2]$ (where M = Na, K, Rb, Cs) was inserted. The electrodes were confined in a T-shaped cell (Figure 3. 2) as described previously.[2,3] Oxygen and water content in the RTILs were removed by purging the cell under vacuum for *ca.* 6 hours prior to and during experiments. This is done since the electrochemical reduction of oxygen[4-8] would alter the voltammetry recorded and the existence of water in RTILs limits their potential windows.[9,10] The experiments were carried out in a temperature controlled box, which also functioned as a Faraday cage (Figure 3. 3). In all electrochemical measurements, the ferrocene│ferrocenium couple, which is considered to be an almost-'ideal' reference material[11-13] was applied as an internal reference standard.

The nickel microelectrode was prepared by inserting 50 μm diameter Ni wire (Advent Research Materials Ltd., UK, 99.7%) in to thermometer glass tubing followed by melting one end of the tube in a Bunsen burner flame to seal the wire. The end of the electrode was then ground down with sandpaper so that a 50 μm diameter cross-section

of the Ni wire was reached (observed using an optical microscope). The microelectrode was then polished in turn with 1.0 μm, 0.3 μm and 0.05 μm alumina slurries (Buehler, Illinois) on a microcloth polishing pad (Buehler, Illinois) and was then further cleaned by placing the electrode in an ultrasonic bath to ensure a shiny surface was achieved before each experiment. The platinum microelectrode was polished using 3 μm, 1 μm and 0.1 μm diamond spray (Kemet Ltd, UK) on a TexMet© polishing pad (Buehler, Illinois) and then rinsed with ultrapure water (Millipore UHQ, Vivendi, UK).

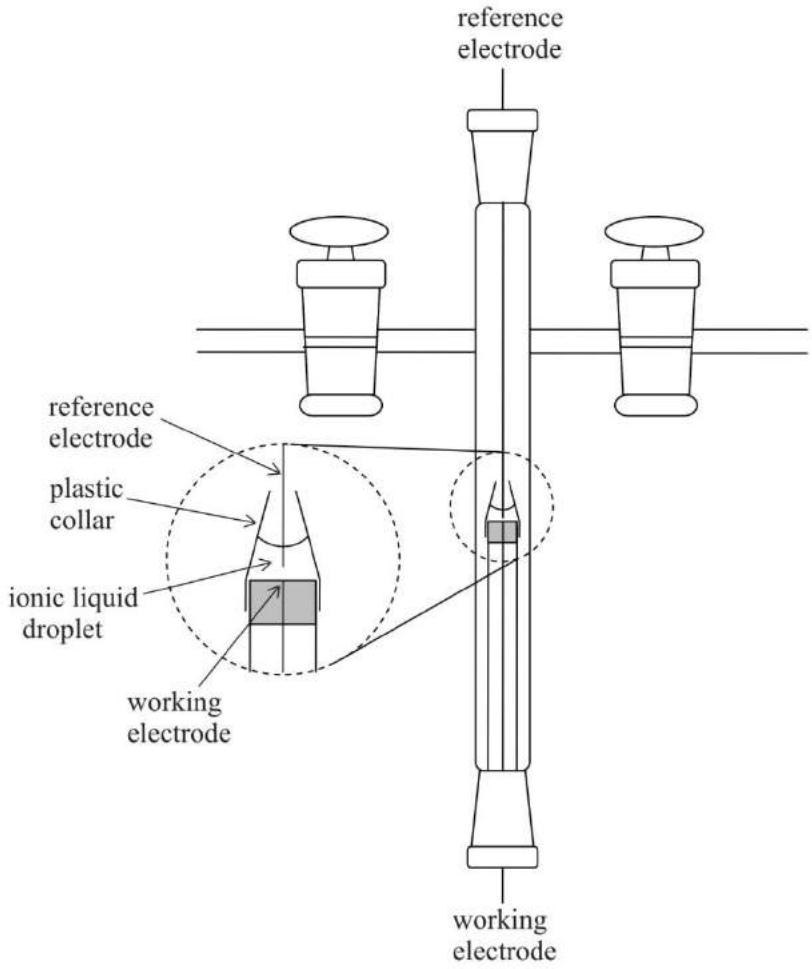

Figure 3. 2 : T- cell for electrochemical experiments

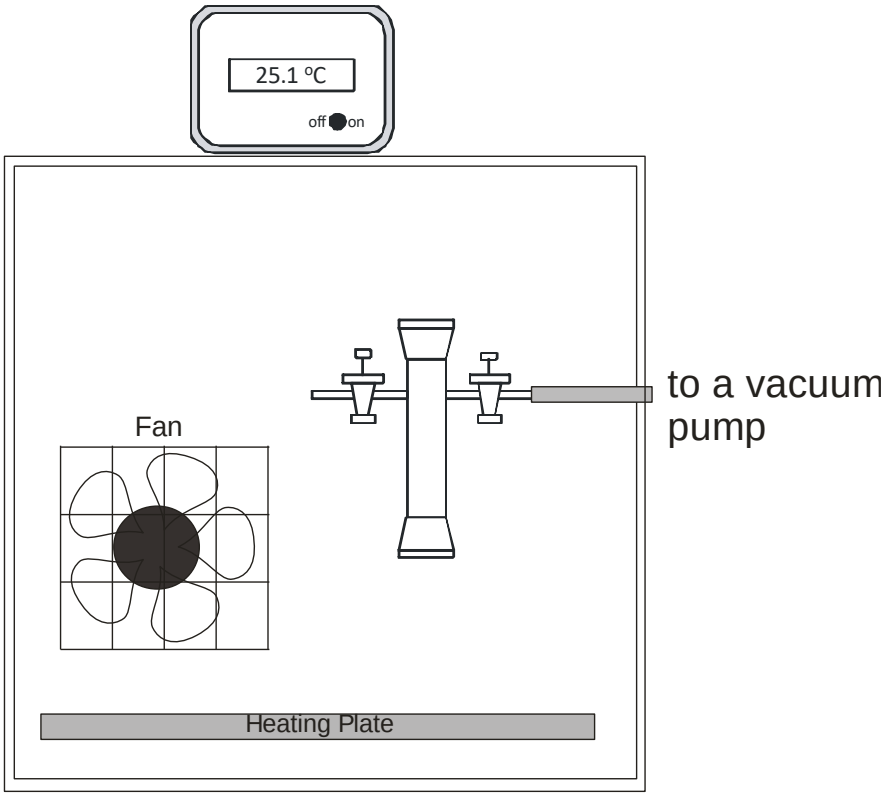

Figure 3. 3: Temperature controlled Faraday cage for electrochemical experiments

3.3.2 *In situ* Electrochemical-X-ray Photoelectron Spectroscopy

XPS measurements were performed using a VG ESCALAB MkII spectrometer equipped with a monochromatic Al Kα X-ray source (photon energy of 1486.6 eV). All XPS experiments were recorded with a constant analyser pass energy of 100 eV for survey scans and 20 eV for detailed scans. All XPS spectra were referenced to the cations C 1s peak, using a binding energy of 285.0 eV. The cell was covered with a specially fashioned lid to prevent ionic liquid loss during degassing, placed upright in a desiccator and put under high vacuum overnight before use. The cell was then rapidly transferred to the entry chamber and evacuated for a further 2 hours before being moved into the holder in sample chamber.

All electrochemical measurements were carried out using a computer-controlled PGSTAT-12 μ-Autolab potentiostat (Eco-Chemie, Netherlands). The cell and the cell holder for *in-situ* electrochemical-XPS experiment was fabricated in house by the aid of

Mr. Charlie Jones of Chemistry Department's Student Workshop and are described in detail in Chapter 7.

3.4 Double Potential Step Chronoamperometry

The diffusion coefficients of ferrocene and ferrocenium were determined using the technique of double potential step chronoamperometry employing a platinum microelectrode (10 μm) as a working electrode and a silver wire as a quasi reference electrode. The experimental transients were achieved using a sample time of 0.01 s. The RTILs solution containing 10 mM ferrocene and 0.1M $Na[NTf_2]$ was pre-treated for 20 s, after which the potential was stepped to a potential after the occurrence of the oxidative wave and the current measured for 5 s, after which the potential was stepped back to the initial value and the current measured again for a further 5 s.

The time-dependent current response obtained was analysed using the following equations, as proposed by Shoup and Szabo[14], which suffciently describe the current response, *i*, over the entire time domain, with a maximum error of less than 0.6 %.

$$i = -4\, n\, F\, D\, c\, r_d\, f(\tau) \tag{3.1}$$

$$f(\tau) = 0.7854 + 0.8863\, \tau^{-1/2} + 0.2146 \exp(-0.7823\, \tau^{-1/2}) \tag{3.2}$$

$$\tau = 4\, D\, t / r_d^2 \tag{3.3}$$

where n is the number of electrons, F is the Faraday constant, D is the diffusion coefficient, c is the initial concentration, r_d is the radius of the microdisk and t is the time. Theoretical transients were generated using a nonlinear curve fitting function available in OriginPro 8 (Microcal Software Inc.). The fit between experimental and theoretical data was optimised by inputting a value for r_d (determined previously from calibration) and instructing the software to iterate through various D, allow for the

diffusion coefficient of ferrocene to be deduced. To model the second potential step, a computer simulation (described by Klymenko et al.)[15] was employed. Having deduced the best-fit values of *D* and *nc* from Shoup and Szabo[14] analysis of the experimental data, the potential steps were analysed by the simulation procedure described previously[15] and the value of *D* for the species formed during the electrochemical process, ferrocenium, was obtained.

References

(1) Bonhote, P.; Dias, A. P.; Papageorgiou, N.; Kalyanasundaram, K.; Gratzel, M. *Inorg. Chem.* **1996**, *35*, 1168-1178.

(2) Evans, R. G.; Klymenko, O. V.; Price, P. D.; Davies, S. G.; Hardacre, C.; Compton, R. G. *ChemPhysChem* **2005**, *6*, 526-533.

(3) Schroder, U.; Wadhawan, J. D.; Compton, R. G.; Marken, F.; Suarez, P. A. Z.; Consorti, C. S.; de Souza, R. F.; Dupont, J. *New J. Chem.* **2000**, *24*, 1009-1015.

(4) Buzzeo, M. C.; Hardacre, C.; Compton, R. G. *ChemPhysChem* **2006**, *7*, 176-180.

(5) Buzzeo, M. C.; Klymenko, O. V.; Wadhawan, J. D.; Hardacre, C.; Seddon, K. R.; Compton, R. G. *J. Phys. Chem. A* **2003**, *107*, 8872-8878.

(6) Evans, R. G.; Klymenko, O. V.; Saddoughi, S. A.; Hardacre, C.; Compton, R. G. *J.Phys. Chem. B* **2004**, *108*, 7878-7886.

(7) Huang, X. J.; Rogers, E. I.; Hardacre, C.; Compton, R. G. *J. Phys. Chem. B* **2009**, *113*, 8953-8959.

(8) Rogers, E. I.; Huang, X. J.; Dickinson, E. J. F.; Hardacre, C.; Compton, R. G. *J. Phys.Chem. C* **2009**, *113*, 17811-17823.

(9) O'Mahony, A. M.; Silvester, D. S.; Aldous, L.; Hardacre, C.; Compton, R. G. *J. Chem. Eng. Data* **2008**, *53*, 2884-2891.

(10) Silvester, D. S.; Compton, R. G. *Z. Phys. Chemie-Int. J. Res. Phys. Chem. Chem.Phys.* **2006**, *220*, 1247-1274.

(11) Bond, A. M.; Oldham, K. B.; Snook, G. A. *Anal. Chem.* **2000**, *72*, 3492-3496.

(12) Rogers, E. I.; Silvester, D. S.; Poole, D. L.; Aldous, L.; Hardacre, C.; Compton, R. G. *J. Phys. Chem. C* **2008**, *112*, 2729-2735.

(13) Zhang, J.; Bond, A. M. *Anal. Chem.* **2003**, *75*, 2694-2702.

(14) Shoup, D.; Szabo, A. *J. Electroanal. Chem.* **1982**, *140*, 237-245.

(15) Klymenko, O. V.; Evans, R. G.; Hardacre, C.; Svir, I. B.; Compton, R. G. *J. Electroanal. Chem.* **2004**, *571*, 211-221.

Chapter 4

The Li/Li$^+$ Couple in Room Temperature Ionic Liquids

In this Chapter, the Li/Li$^+$ couple is investigated in the room temperature ionic liquid (RTILs), *N*-butyl-*N*-methylpyrrolidinium bis(trifluoromethylsulfonyl)imide, [C_4mpyrr][NTf_2], at a range of temperatures varying from 298 to 318 K. Experiments are conducted using both nickel and platinum microelectrodes. On nickel a single stripping peak is observed for the stripping of bulk lithium that allowed thermodynamic and kinetic parameters to be extracted via computational simulation. At 298 K the electrochemical rate constant (k^0) = 1.2 x 10^{-5} cm s^{-1}, the diffusion coefficient (D) = 4.5 x 10^{-8} cm^2 s^{-1}, the formal potential (E_f^0) = –3.250 V versus the Fc/Fc$^+$ reference couple and the transfer coefficient (α) = 0.63. On platinum multiple stripping peaks are observed due to the stripping of Li-Pt alloys in addition to the stripping of bulk lithium. The ratio of the different stripping peaks is found to change with temperature indicating that Li-Pt alloys are more thermodynamically stable than pure bulk lithium and platinum. Further experiments were conducted in other RTILs, [C_4dmim][NTf_2], [$N_{2,1,1,3}$][NTf_2], [$N_{6,2,2,2}$][NTf_2], [C_4mim][OTf], [C_4mpyrr][$N(CN)_2$], [C_2mim][NTf_2], [$P_{14,6,6,6}$][FAP], [C_4py][NTf_2], [C_4mim][PF_6], [C_4mim][NTf_2] and [$N_{1,8,8,8}$][OTf], using only Ni microelectrode. [C_4mpyrr][$N(CN)_2$], [C_2mim][NTf_2], [$P_{14,6,6,6}$][FAP], [C_4py][NTf_2], [C_4mim][PF_6], [C_4mim][NTf_2] and [$N_{1,8,8,8}$][OTf] did not have a wide enough potential window to observe the deposition and stripping of bulk lithium. In the experimental data recorded for [C_4mpyrr][NTf_2], [C_4dmim][NTf_2], [$N_{2,1,1,3}$][NTf_2], [$N_{6,2,2,2}$][NTf_2] and [C_4mim][OTf] a single stripping peak for bulk lithium is seen and kinetic data for the Li/Li$^+$ couple extracted by comparison with computational simulations. The electrochemical rate constant, k^0, is found to have values ranging from

1.3×10^{-6} to 1.2×10^{-5} cm·s^{-1}. Diffusion coefficients for the Li^+ ion in these five RTILs are also reported.

4.1 Introduction

Room temperature ionic liquids (RTILs) are typically composed of a bulk unsymmetric cation and an inorganic anion and exist in a liquid state at around 298 K.[1-4] They possess a number of attractive properties as solvents for electrochemical applications including low volatility, high thermal stability, wider potential windows and intrinsic conductivity that removes the need for a supporting electrolyte to be added. RTILs are typically 1-2 orders of magnitude more viscous than traditional solvents leading to the slower diffusion of species in the solvent which has a significant effect on the appearance of the voltammetry recorded. The Li/Li$^+$ couple cannot be studied in aqueous solutions as the potential window is not wide enough and traditional organic solvents have therefore been used instead.[5-7] There are however safety concerns when using organic solvents in such technology due to their high volatility and combustibility. Moreover there is currently much interest in the study of the Li/Li$^+$ couple in RTILs due to the importance of the Li/Li$^+$ couple in applications such as batteries, solar cells and fuel cells.[8-12] Much work has already been carried out in the study of the Li/Li$^+$ couple in ionic liquids[13-16] and more traditional solvent[17-19], however very limited research has been carried out to look at the kinetics over a range of temperatures[20,21] and the extraction of electrochemical parameters via the use of computer simulation has only been reported for the Li/Li$^+$ couple in THF.[17]

In the present Chapter we discuss the results of a study of the Li/Li$^+$ couple in the RTILs using Ni and Pt microelectrodes. The aim of this Chapter is to study the kinetics and thermodynamics of the Li/Li$^+$ couple by considering the deposition and stripping of bulk lithium using both experimental and computer simulation data. We also report the differences in the voltammetry caused by changing the working electrode between nickel and platinum microelectrodes.

4.2 Results and Discussion

4.2.1 Experimental results

4.2.1.1 Deposition on a Ni microelectrode at different temperatures

Figure 4. 1 shows the cyclic voltammetry (base line corrected) run between 0 and -3.65 V versus the Fc/Fc$^+$ reference couple for 0.1 M $LiAsF_6$ in $[C_4mpyrr][NTf_2]$ recorded on the first scan on a clean 50 μm diameter Ni electrode at 298 K. The voltammetry shows two noticeable underpotential deposition (UPD) peaks due to the energetically stable formation of lithium monolayers on the nickel surface before the main bulk deposition process begins at ca. -3.45 V. The bulk deposition region shows a characteristic "nucleation loop" where the forward and backwards current cross over. This is due to the delay in the onset and rate of deposition on the forwards scan due to the need for lithium to first nucleate on the electrode surface. On the reverse scan there is a sharp peak at ca. -3.2 V which corresponds to the stripping of bulk lithium from the electrode. The other small peaks observed on the reverse scan are due to the dissolution of the UPD layers. The UPD results in multiple peaks due to the different phases of lithium on the polycrystalline electrode. This pattern of UPD peaks of lithium on a nickel electrode

has previously been studied and reported using a nickel electrode in a lithium-based solid polymer electrolyte.[22] This system also showed the same characteristic sharp stripping peak for bulk lithium. The voltammetry in Figure 4. 1 shows the same general characteristic as shown by a previous study of the Li/Li$^+$ couple in the solvent THF on a Pt microelectrode.[17]

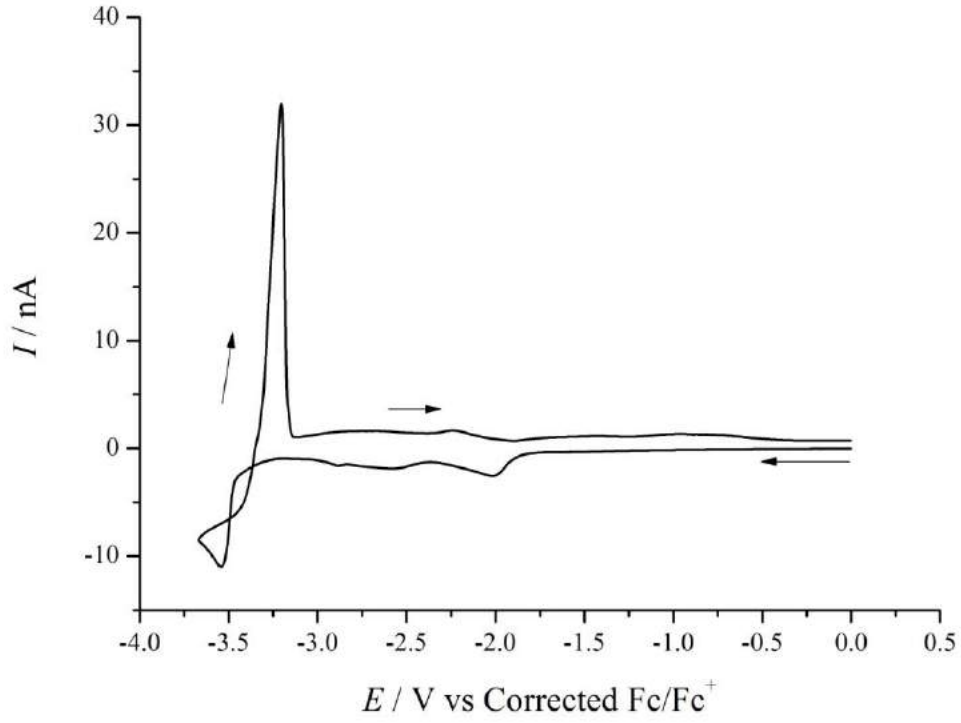

Figure 4. 1: Cyclic voltammogram of 0.1 M $LiAsF_6$ in [C_4mpyrr][NTf_2] on a 50 μm diameter Ni electrode at 298 K. Scan rate = 10 mV s^{-1}.

The charge passed during the stripping process is 2.8 x 10^{-7} C which corresponds to approximately 63 ± 5 layers of lithium, showing that the system is depositing and stripping bulk lithium. The distribution of lithium on the electrode surface will be uneven due to the presence of radial diffusion, most prominent near the microelectrode edge. 3.95 x 10^{-7} C of charge is passed during the deposition stage giving the first deposition/stripping cycle a stripping efficiency of 70 % meaning less material was stripped off than deposited. It is believed that the possible formation of dendritic

deposits which could prevent the lithium from being in contact with the electrode as well as the reactivity of the lithium might responsible for this behaviour.[20] Reactions between the deposited lithium and breakdown products of the ionic liquid may also lead to the formation of surface films that passivate parts of the electrode surface. On successive cycles the current sharply drops indicating that the electrode becomes passivated. However, extracting the kinetics and thermodynamic parameters for the Li/Li$^+$ couple by modelling the voltammogram from the first lithium deposition and dissolution cycle is feasible.

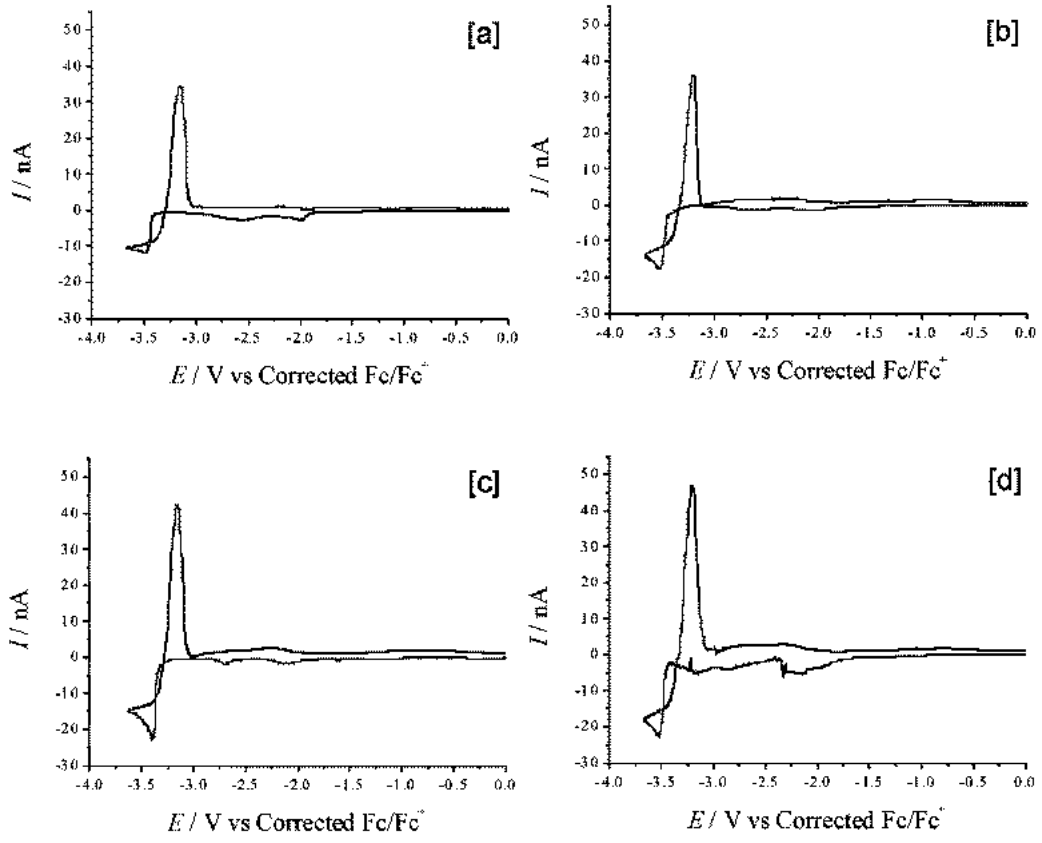

Figure 4. 2: Cyclic voltammogram (baseline corrected) of 0.1 M $LiAsF_6$ in [C_4mpyrr][NTf_2] on a 50 μm diameter Ni electrode at (a) 303 K, (b) 308 K, (c) 313 K, and (d) 318 K. Scan rate = 10 mV s^{-1}.

Figure 4. 2 shows the effects of varying the temperature between 303 and 318 K for the experiment on the voltammetry of $LiAsF_6$ in [C_4mpyrr][NTf_2] on the Ni microelectrode.

At all temperatures the same general characteristics are observed including a UPD region, a single sharp bulk stripping peak and a nucleation loop as where seen in Figure 4. 1 for the experiment at 298 K. However, there are subtle differences including the maximum deposition current increasing with temperature which is due to the increase in the diffusion coefficient of Li^+ in $[C_4mpyrr][NTf_2]$. The stripping peak height also increases indicating that the increased temperature leads to an increase in the amount of lithium deposited and stripped from the electrode. The stripping efficiency varied between 55 and 80%. The simplicity of this system means that analysis by simulation using the model described in section 1.5 in Chapter 1 is possible and is presented below in section 4.2.2.1.

4.2.1.2 Deposition on a Pt microelectrode at different temperatures

The behaviour of the Li/Li$^+$ couple at a platinum electrode was also studied. An interesting voltammogram for the lithium deposition/dissolution process on a platinum microelectrode (10 μm diameter) is shown in Figure 4. 3 Similar features, which include UPD peaks and the nucleation process, as observed on nickel can also be observed in this voltammogram. However, multiple peaks can clearly be seen on the reverse scan in addition. Peak I observed at -3.05 V *versus* Fc/Fc$^+$ is considered to be the stripping peak for the dissolution of bulk lithium as seen on nickel while peaks II, III and IV correspond to the stripping of Li-Pt alloys.

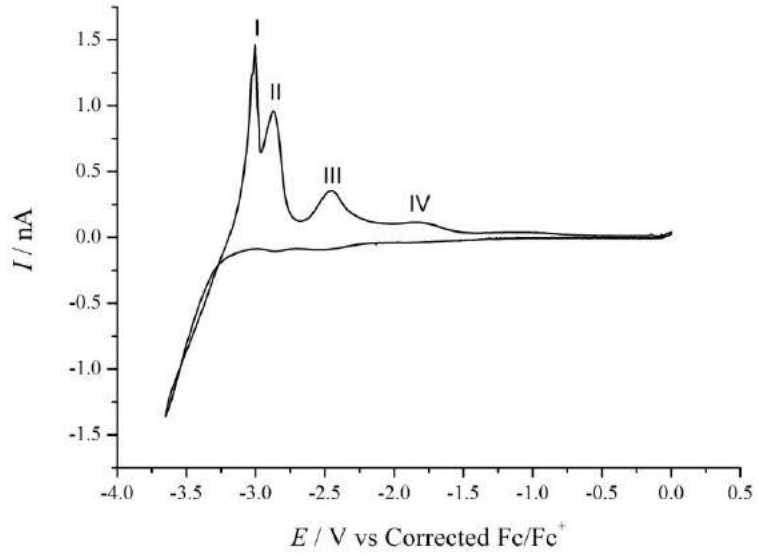

Figure 4. 3: Cyclic voltammogram of 0.1 M $LiAsF_6$ in $[C_4mpyrr][NTf_2]$ on a 10 μm diameter Pt electrode at 298 K. Scan rate = 10 mV s^{-1}.

The dissolution of bulk lithium on platinum is slightly shifted to a more positive potential compared to that observed on the nickel electrode. Evidence that lithium is able to form various different alloys with platinum can be seen from the phase diagram for Li-Pt shown in Figure 4. 4[23] Similar multiple peaks for the dissolution of lithium on a platinum electrode have also been reported by another group[13] and similar behaviour is expected when using a gold electrode due to lithium ability to form Li-Au alloys.[24,25]

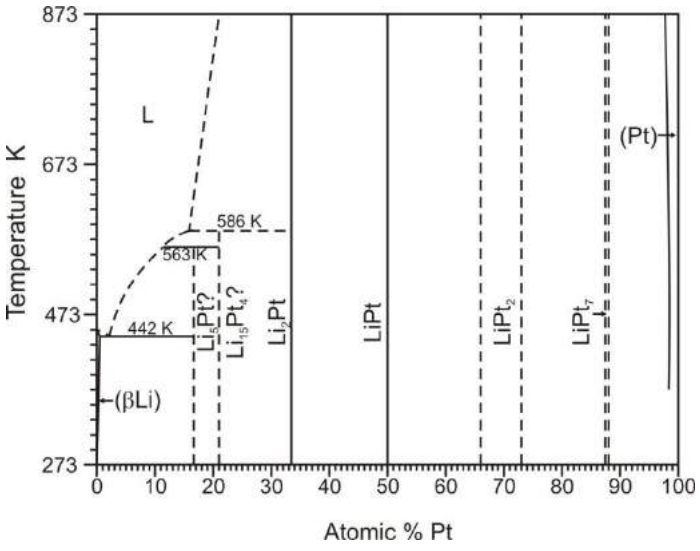

Figure 4. 4: Phase diagram of the Li-Pt system adapted from ref 23.

Figure 4. 5 shows a cyclic voltammogram for 0.1 M $LiAsF_6$ in [C_4mpyrr][NTf_2] on a Pt microelectrode at 10 mV s^{-1} confined to the potential region where underpotential deposition occurs. Three peaks are observed and these are assigned to UPD deposition on the different crystal faces of Pt as is the case for a Pt electrode in THF.[26] The peaks are spread over a similar potential range and it is therefore expected that the deposition peaks at –1.75, -2.60 and –2.85 V correspond to monolayer formation on the (111), (110) and (100) crystal faces of platinum respectively.[26]

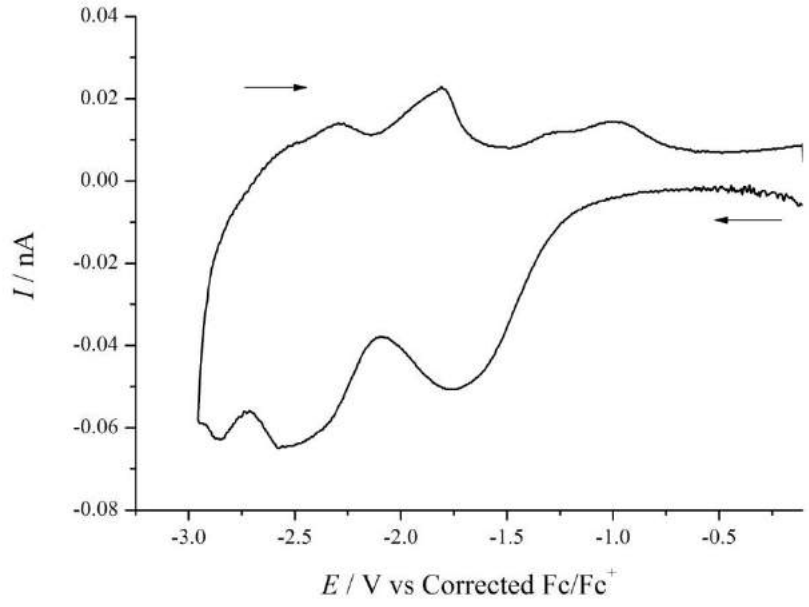

Figure 4. 5: A cyclic voltammogram of the underpotential deposition region for 0.1 M $LiAsF_6$ in [C_4mpyrr][NTf_2] on a 10 μm diameter Pt electrode at 298 K. Scan rate = 10 mV s^{-1}.

Next, the effect of temperature on the electrochemistry of lithium on a Pt microelectrode was studied. Figure 4. 6 shows the cyclic voltammogram of 0.1 M $LiAsF_6$ in [C_4mpyrr][NTf_2] at five different temperatures. At 298 K, peak I is relatively high compared to the other peaks. As the temperature was increased, peak I decreases and disappears at 313 K. In contrast, the height of peak II increases and starts to level off at 308 K. The height of peaks III and IV show significant increment from 298 to 313 K. Another feature that can be observed as the temperature increases is that the limiting

current on the forward scans increases. This can be understood since the diffusion of material to the surface of electrode increases as the ionic liquid become less viscous at higher temperature. As a consequence, more lithium will be deposited. However at higher temperature, the lithium deposits have a chance to rearrange, interacting with the platinum electrode to form Li-Pt alloys. This could explain why peak I, which corresponds to the dissolution of lithium off lithium, diminishes. Moreover the increment of other peaks at higher temperature gives an insight that the formation of Li-Pt alloys is thermodynamically favourable than pure bulk lithium and platinum.

The behaviour of the Li/Li$^+$ couple on a Pt electrode in [C_4mpyrr][NTf_2] varies from that observed on the same electrode when THF is used as the solvent where no alloy formation is seen.[17] One suggested explanation for this is that the higher rate of diffusion of Li$^+$ in THF results in faster formation of a thick stable bulk lithium layer that restricts the access of additional Li$^+$ ions to the Pt electrode whereas the slower diffusion coefficient in [C_4mpyrr][NTf_2] means that layers of Li are built up more slowly allowing some of the Li to become incorporated within the Pt electrode and to form alloys with it.

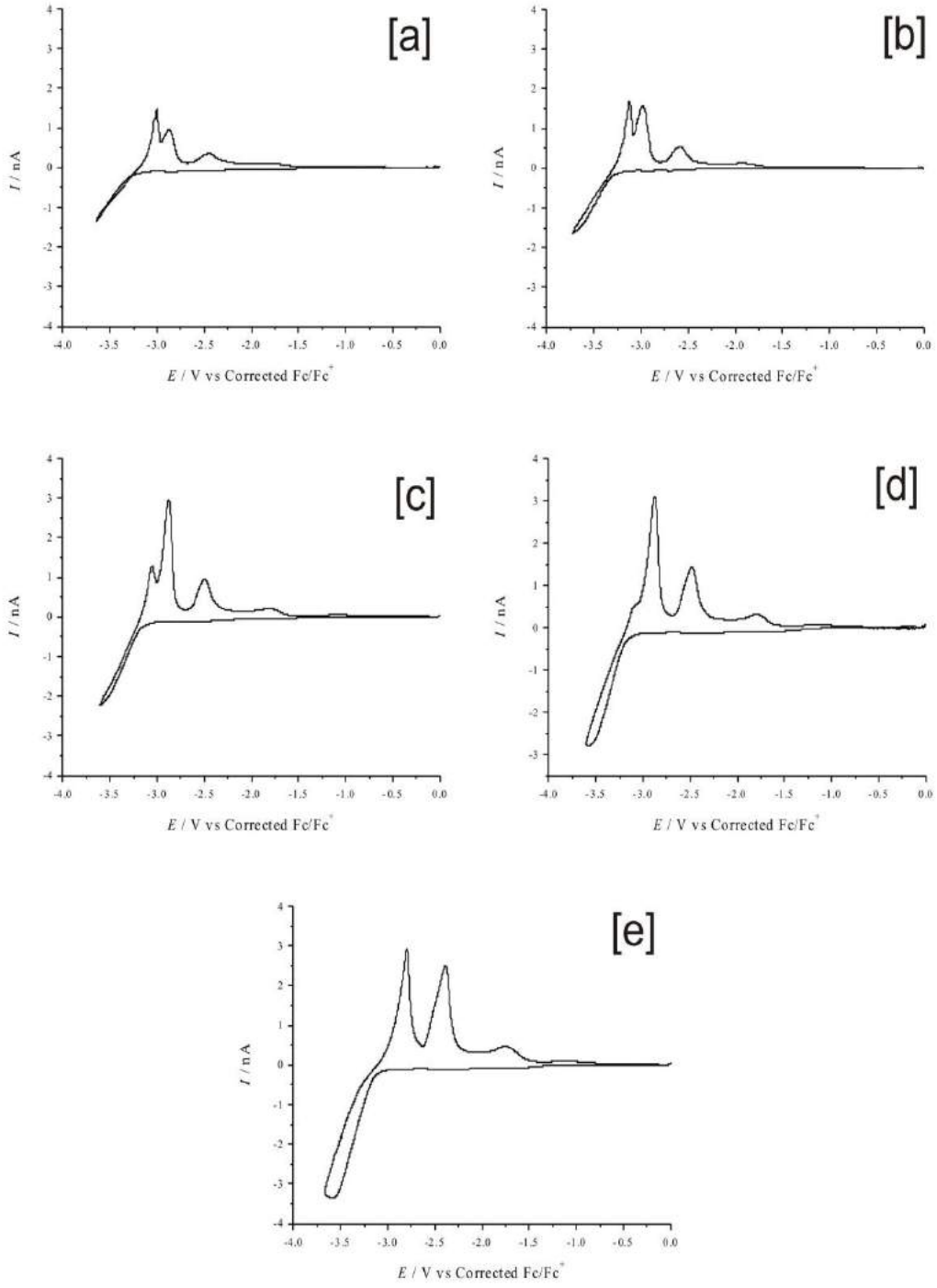

Figure 4. 6: Cyclic voltammograms of 0.1 M $LiAsF_6$ in [C_4mpyrr][NTf_2] on a 10 μm diameter Pt electrode at (a) 298 K, (b) 303 K, (c) 308 K, (d) 313 K and (e) 318 K. Scan rate = 10 mV s^{-1}.

4.2.2 Theoretical results

4.2.2.1 Simulation results from deposition on a Ni electrode

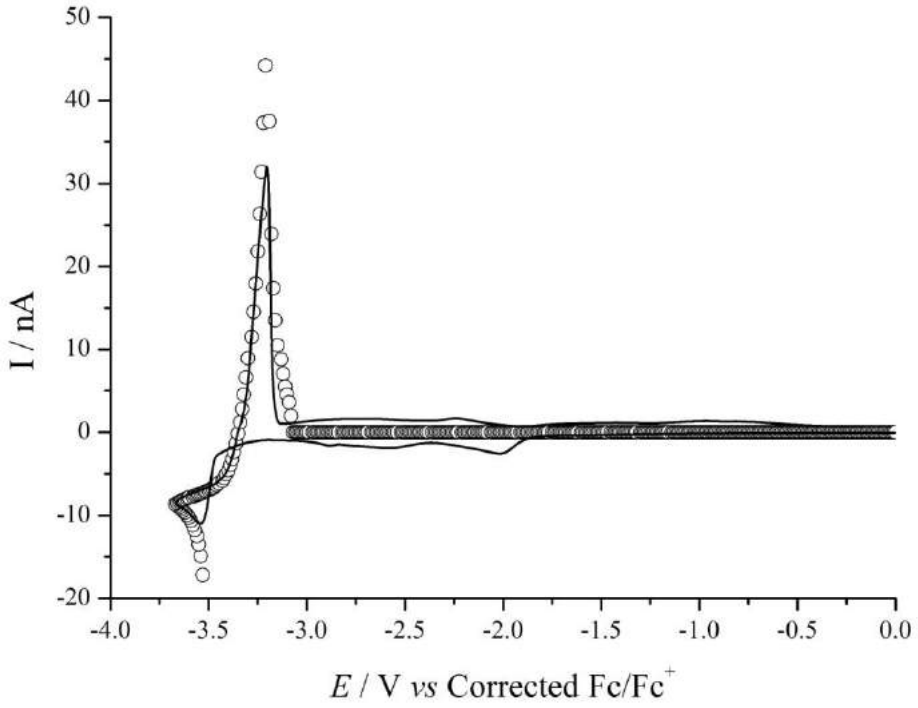

Figure 4. 7: The fit of experimental (-) and simulation (o) data for the cyclic voltammetry experiment using 0.1 M $LiAsF_6$ in $[C_4mpyrr][NTf_2]$ on a 50 μm diameter Ni electrode at 298 K. Scan rate = 10 mV s^{-1}.

The experimental data presented in Section 4.2.1 for the investigation of Li/Li$^+$ on a nickel microelectrode at a range of temperatures was simulated using the mathematical model presented in Chapter 1. Figure 4. 7 shows an example of the fit of experimental and simulation data for the voltammogram recorded at 298 K as shown in Figure 4. 1. The mathematical model is designed to simulate the bulk deposition and stripping, however it does not incorporate the process for the initial nucleation of lithium on top of the Li UPD layers. As a result the model does not cover the start of the bulk deposition process and it is therefore necessary to start the simulation after this point in order to not overestimate the amount of lithium deposited. From Figure 4. 7 it can be

seen that there is a good fit for the rest of the deposition process and for the left hand side of the stripping peak. However, the simulation stripping process continues for longer than the experimental peak and this is due to the presence of incomplete stripping in the experiment that means the stripping peak is not as big as that expected from the deposition current, while the mathematical model assumes a 100% stripping efficiency. Accurate electrochemical parameters can still be extracted as all the experimental information needed is contained in the range between the start of the reverse scan and the top of the stripping peak.

The electrochemical parameters extracted from the five different temperature experiments (shown in Figure 4. 1 and Figure 4. 2) are given in Table 4.1. From the Table it can be seen that the diffusion coefficient (D) and electrochemical rate constant (k^0) for the Li/Li$^+$ couple increase as the temperature increases from 298 to 318 K. Changes in D are due to the changes in the viscosity of the liquid as lithium ions can diffuse more easily as the liquid becomes less viscous at higher temperatures.

Table 4. 1: The electrochemical parameters for the Li/Li$^+$ couple in [C$_4$myprr][NTf$_2$] determined from the simulation for experimental data at various temperatures recorded on a Ni microelectrode.

Temperature T / K	Diffusion coefficient D / cm^2 s^{-1} ± 0.5 10^{-8}	Rate constant k^0 / cm s^{-1} ± 0.05 x 10^{-5}	Formal potential E_f^0 / V vs. Corrected Fc/Fc$^+$ ± 0.01	Transfer coefficient α
298	4.5 x 10^{-8}	1.2 x 10^{-5}	-3.250	0.63
303	7.0 x 10^{-8}	1.5 x 10^{-5}	-3.200	0.63
308	9.4 x 10^{-8}	1.8 x 10^{-5}	-3.240	0.63
313	1.1 x 10^{-7}	2.1 x 10^{-5}	-3.190	0.63
318	1.2 x 10^{-7}	2.2 x 10^{-5}	-3.240	0.63

Figure 4. 8 shows a plot of ln(*D*) *versus* T^{-1} and gives an approximate linear relationship and that suggests the diffusion coefficient of lithium in [C_4mpyrr][NTf_2] follows an Arrhenius-type temperature dependency.[27] The diffusional activation energy ($E_{a,D}$) of Li^+ in the ionic liquid calculated from the plot gives the value of 37.5 kJ mol^{-1}. This value is slightly higher than the viscocity activation energy ($E_{a,\eta}$ = 25.1 kJ mol^{-1})[28] measured for [C_4mpyrr][NTf_2] with the difference likely being the result of the very small size of the lithium ions and hence deviates from classical Stoke-Einstein behaviour.[29]

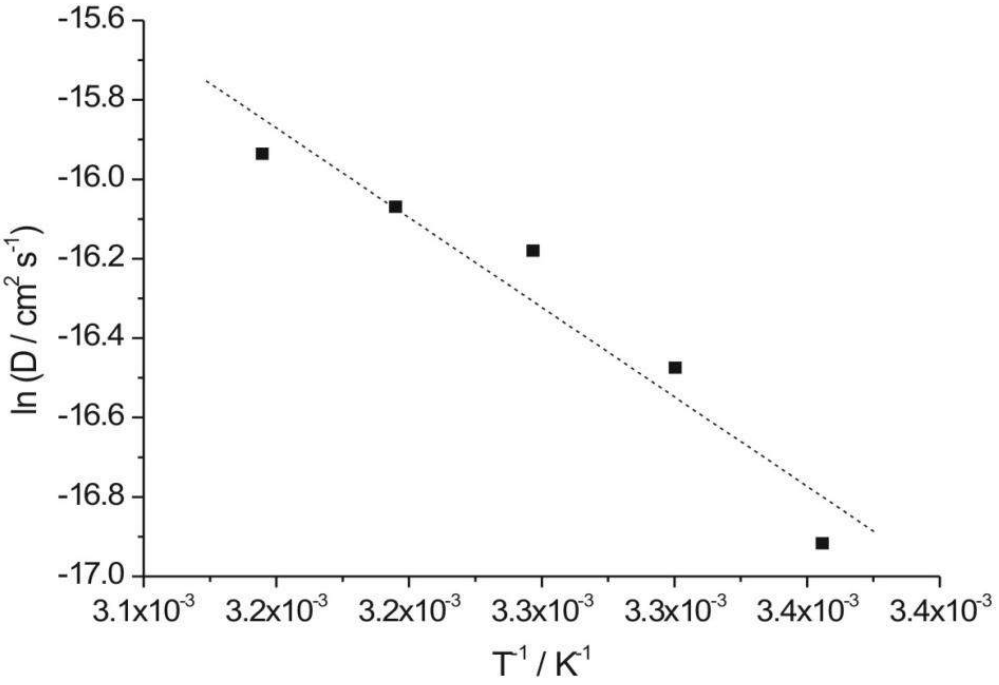

Figure 4. 8: A plot of ln(*D*) versus 1/T. From the line of best fit, d(ln(*D*)/d(1/T) = 4510 K (R^2 = 0.93).

A linear relationship is also observed in Figure 4. 9 for ln(k^0) *versus* T^{-1} which then gives the value of 23.7 kJ mol^{-1} for the activation energy for the Li/Li^+ couple in [C_4mpyrr][NTf_2]. This value is lower than that observed for the same couple with THF

as the solvent.[17] The formal potential does not vary in a consistent way suggesting that experimental error is larger than any difference due to temperature. In all cases the transfer coefficient was found to be 0.63.

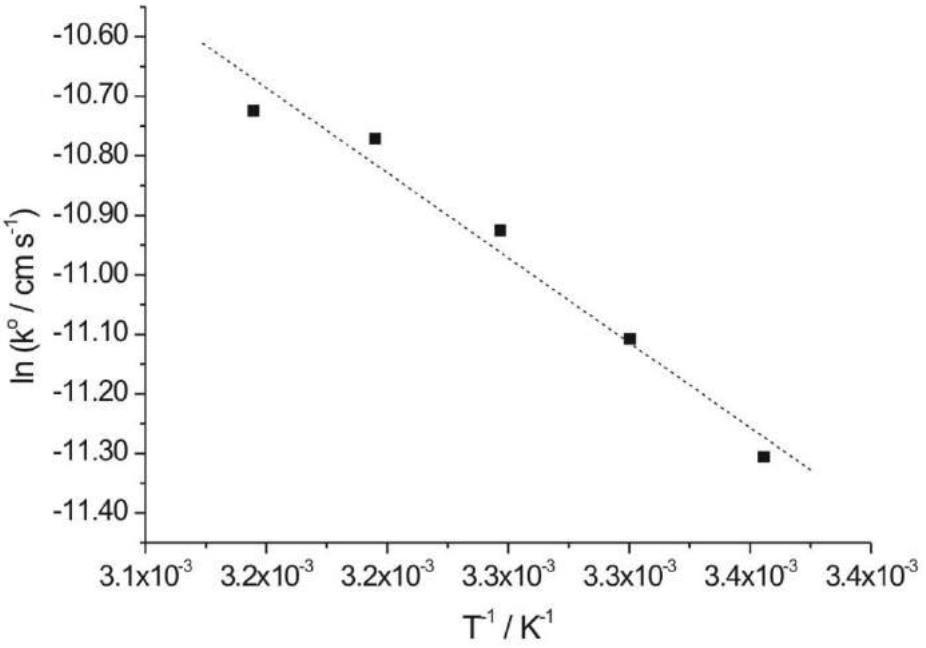

Figure 4. 9: A plot of ln(k^0) versus 1/T. From the line of best fit, d(ln(k^0)/d(1/T) = 2851 K (R^2 = 0.97).

4.2.2.2 Simulating the deposition on a Pt microelectrode

It is not possible to accurately simulate the data for the bulk deposition and stripping of lithium when recorded using a Pt electrode as the signal for deposition is due to both the formation of bulk lithium and the formation of Li-Pt alloys. It is therefore not possible to gain accurate details about the surface area of bulk lithium exposed to the solution for stripping or the amount of bulk lithium deposited. It is also difficult the separate out the process of bulk lithium stripping from the alloy stripping that occurs at only a slightly higher potential (peak II in Figure 4. 3). Attempts to model the experimental data recorded using a platinum electrode would lead to an underestimation of the electrochemical rate constant and also a difference in the transfer coefficient.

4.2.3 The Li/Li$^+$ couple in a wide range of RTILs at 296 K on Ni microelectrode

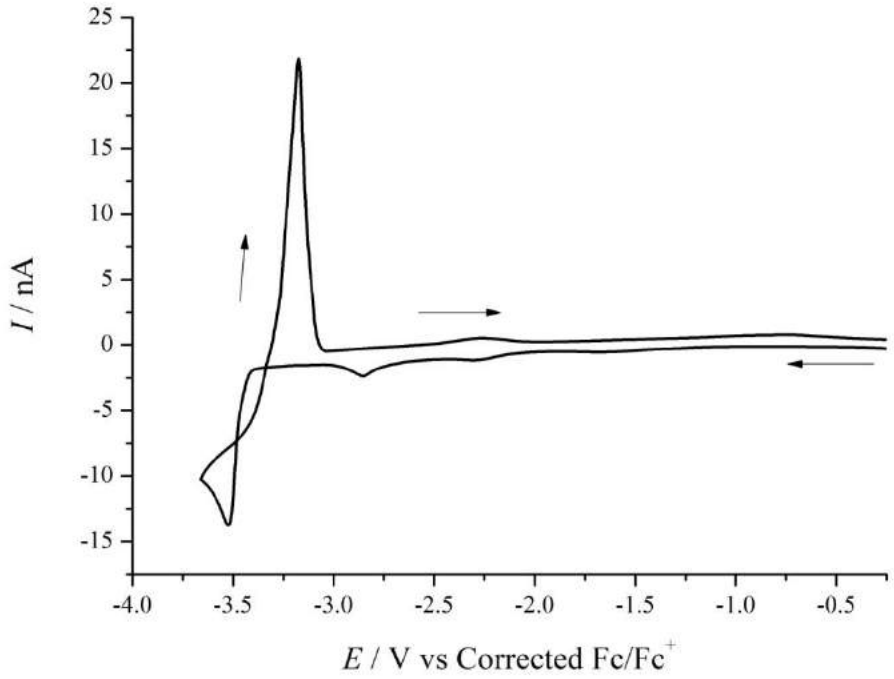

Figure 4. 10: The cyclic voltammogram recorded for a 0.1 M $LiAsF_6$ in [C_4dmim][NTf_2] solution on a 50 μm diameter Ni electrode. Scan rate = 10 mV·s^{-1}.

From the previous results described in Section 4.2.1 and 4.2.2, the nickel electrode is found to be a suitable electrode to study the electrodeposition and stripping processes for lithium in the ionic liquid [C_4mpyrr][NTf_2]. We then expand our investigation of Li/Li$^+$ couple in a wide range of RTILs. Figure 4. 10 shows an example of the voltammetry recorded on a clean electrode on the first cycle when the potential window of the RTIL is wide enough. This cyclic voltammetry was recorded by sweeping the potential from –0.2 V to –3.65 V *versus* Fc/Fc$^+$ and back with a 0.1 M $LiAsF_6$ solution in the RTIL [C_4dmim][NTf_2] at a scan rate of 10 mV·s^{-1}. The small peaks observed on the forward scan between –2 and –3 V as due to the underpotential deposition (UPD) of lithium whereas the current recorded below –3.4 V is due to bulk lithium deposition. On

the reverse scan a sharp stripping peak for bulk lithium is observed at ca. -3.2 V and the small peaks above this are due to the stripping of the UPD layers.

The potential window of a clean Ni electrode in a blank RTIL solution is smaller than that when lithium ions are present. This is due to the underpotential deposition of a lithium monolayer onto the nickel surface which changes the character of the working electrode. It is therefore not possible to judge whether the potential window of an ionic liquid is wide enough to study bulk lithium deposition without running a full cyclic voltammogram with lithium ions present.

Eleven different ionic liquids in addition to [C_4mpyrr][NTf_2] were used as supporting electrolytes to perform lithium electrochemistry and a summary of the results is provided in Table 4. 2. Five different ionic liquids (Table 4. 2) were found to be stable enough to reach the potential of the bulk Li/Li$^+$ process and showed voltammetry with the same characteristics as shown in Figure 4. 10, however the magnitude of the current recorded and amount of lithium deposited and stripped varied. Seven other ionic liquids (Table 4. 2 f-l) seem to be too unsuitable to support lithium electrochemistry as they tend to breakdown before reaching the deposition and dissolution process of bulk lithium. Therefore no observable bulk stripping signals can be seen in the voltammetry.

Table 4. 2: Experimental observations and parameters extracted by simulation for the Li/Li$^+$ couple in a range of RTILs at 298 K.

No.	**RTIL**	**Viscosity η/(cP)**	**Bulk lithium stripping observed?**	**Diffusion coefficient D /(cm^2·s^{-1}) ± 0.1 × 10^{-8}**	**Rate constant k^0/(cm·s^{-1}) ± 0.05 × 10^{-5}**	**Formal potential E_f^0/(V) vs corrected Fc/Fc$^+$ ± 0.01**	**Transfer coefficient α**
a	[C_4mpyrr][NTf_2]	89[28]	Yes	4.5 × 10^{-8}	1.2 × 10^{-5}	-3.250	0.63
b	[C_4dmim][NTf_2]	105[28]	Yes	5.0 × 10^{-8}	5.5 × 10^{-6}	-3.130	0.50
c	[$N_{2,1,1,3}$][NTf_2]	-	Yes	2.8 × 10^{-8}	1.0 × 10^{-5}	-3.234	0.50
d	[$N_{6,2,2,2}$][NTf_2]	167[30]	Yes	1.9 × 10^{-8}	5.0 × 10^{-6}	-3.158	0.50
e	[C_4mim][OTf]	90[31]	Yes	3.1 × 10^{-8}	1.3 × 10^{-6}	-3.390	0.70
f	[C_4mpyrr][$N(CN)_2$]	-	No – UPD only	-	-	-	-
g	[C_2mim][NTf_2]	34 [31]	No – UPD only	-	-	-	-
h	[$P_{14,6,6,6}$][FAP]	464 [32,33]	No	-	-	-	-
i	[C_4py][NTf_2]	60 [34]	No	-	-	-	-
j	[C_4mim][PF_6]	371 [35]	No	-	-	-	-
k	[C_4mim][NTf_2]	52 [31]	No – UPD only	-	-	-	-
l	[$N_{1,8,8,8}$][OTf]	-	No – UPD only	-	-	-	-

It is noticed however that the underpotential deposition signals can still be observed in $[C_4mpyrr][N(CN)_2]$, $[C_2mim][NTf_2]$, $[C_4mim][NTf_2]$ and $[N_{1,8,8,8}][OTf]$. The ionic liquids $[C_4mim][PF_6]$ and $[P_{14,6,6,6}][FAP]$ seem to react with $LiAsF_6$ as suggested by the observation of a color change of the solutions to blue and green respectively.

Table 4. 2 presents the electrochemical parameters for Li/Li$^+$ couple at room temperature in five different ionic liquids extracted from the experimental data using the mathematical model described in Chapter 1. $[C_4mpyrr][NTf_2]$, $[C_4dmim][NTf_2]$, $[N_{2,1,1,3}][NTf_2]$, $[N_{6,2,2,2}][NTf_2]$ and $[C_4mim][OTf]$ all show good electrochemical responses for Li/Li$^+$ and the kinetics are all within a narrow range. The combination of the $[NTf_2]^-$ anion with the butylmethylpyrrolidinium cation ($[C_4mpyrr]^+$) provides both a relatively fast rate constant and diffusion coefficient for the Li/Li$^+$ couple compared to other ionic liquids. Other $[NTf_2]^-$ salt families that indicate good performance to support lithium electrochemistry are quaternary ammonium ($[N_{2,1,1,3}]^+$ and $[N_{6,2.2,2}]^+$) and immidazolium ($[C_4dmim]^+$). These types of ionic liquid have been used to study the lithium system due to their stability upon application of extreme cathodic potentials.[36] The differences in the diffusion coefficients may result from the differences in the viscosities, which have an impact on the transport property of lithium ions to the electrode surface. However the diffusion coefficient for Li$^+$ did not scale with η^{-1} as would be expected from Stokes-Einstein behavior.[29] $[C_4mim][OTf]$ shows a slightly slower rate constant and a higher transfer coefficient than any of the $[NTf_2]^-$ salts indicating that changing the anion of the ionic liquid can make a difference to the voltammetry. However, the electrochemical rate constant, k^0, does not vary over a

significant range and the slight difference between the various RTILs probably reflects the slightly altered solvation of the Li^+.

4.3 Conclusions

The deposition and dissolution of lithium has been investigated using [C_4mpyrr][NTf_2] as a supporting electrolyte on nickel and platinum microelectrodes at various temperatures ranging from 298 to 318 K. A single stripping peak for the Li/Li^+ couple was observed on the nickel electrode showing that the bulk deposition of lithium onto lithium occurs. Thermodynamic and kinetic parameters such as the electrochemical rate constant (k^0), diffusion coefficient (D), formal potential (E_f^0) and transfer coefficient (α) have been extracted using computer simulation. When platinum was used as the working electrode multiple stripping peaks were observed due to the stripping of Li-Pt alloys. From the various temperature experiments, it is seen that the Li-Pt alloys are more thermodynamically stable than pure bulk lithium and platinum. In addition, the Li/Li^+ couple has been investigated in a range of RTILs. A number of these RTILs ([C_4mpyrr][$N(CN)_2$], [C_2mim][NTf_2], [$P_{14,6,6,6}$][FAP], [C_4py][NTf_2], [C_4mim][PF_6], [C_4mim][NTf_2], [$N_{1,8,8,8}$][OTf]) were found to break down before the onset of the deposition and stripping of bulk Li and were therefore not investigated further. For the RTILs that have potential windows wide enough to observe the bulk deposition and stripping of lithium ([C_4mpyrr][NTf_2], [C_4dmim][NTf_2], [$N_{2,1,1,3}$][NTf_2], [$N_{6,2,2,2}$][NTf_2], [C_4mim][OTf]), mathematical modelling and numerical simulation has been used to extract kinetic data for the Li/Li^+ couple. The rate constant, k^0, for the Li/Li^+ couple did not vary significantly when the [NTf_2]$^-$ anion was used with a range of cations to form

the ionic liquid however, a slight changing was observed in the voltammetry when the anion was changed to [OTf]$^-$. The slight differences in the rate constant and transfer coefficient probably reflect the different solvation of the Li^+ ions in the different RTILs. Formal potentials for the Li/Li^+ couple are also reported.

In the next chapter, the Na/Na^+ couple in some temperature ionic liquids will be studied and the result is compared to that Li/Li^+ couple.

References

(1) Silvester, D. S.; Compton, R. G. *Z. Phys. Chemie-Int. J. Res. Phys. Chem. Chem. Phys.* **2006**, *220*, 1247-1274.

(2) Buzzeo, M. C.; Hardacre, C.; Compton, R. G. *ChemPhysChem* **2006**, *7*, 176-180.

(3) Hapiot, P.; Lagrost, C. *Chem. Rev.* **2008**, *108*, 2238-2264.

(4) Endres, F.; El Abedin, S. Z. *Phys. Chem. Chem. Phys.* **2006**, *8*, 2101-2116.

(5) Hedges, W. M.; Pletcher, D. *Journal of the Chemical Society-Faraday Transactions I* **1986**, *82*, 179-188.

(6) Yang, X. L.; Wen, Z. Y.; Zhu, X. J.; Huang, S. H. *Solid State Ion.* **2005**, *176*, 1051-1055.

(7) Lee, S. I.; Jung, U. H.; Kim, Y. S.; Kim, M. H.; Ahn, D. J.; Chun, H. S. *Korean J. Chem. Eng.* **2002**, *19*, 638-644.

(8) Sakaebe, H.; Matsumoto, H.; Tatsumi, K. *Electrochim. Acta* **2007**, *53*, 1048-1054.

(9) Borgel, V.; Markevich, E.; Aurbach, D.; Semrau, G.; Schmidt, M. *J. Power Sources* **2009**, *189*, 331-336.

(10) Macfarlane, D. R.; Forsyth, M.; Howlett, P. C.; Pringle, J. M.; Sun, J.; Annat, G.; Neil, W.; Izgorodina, E. I. *Accounts Chem. Res.* **2007**, *40*, 1165-1173.

(11) Urquidi-Macdonald, M.; Castaneda, H.; Cannon, A. M. *Electrochim. Acta* **2002**, *47*, 2495-2503.

(12) Daniel, C. *Journal of Material* **2008**, *60*, 43-48.

(13) Matsumoto, H.; Sakaebe, H.; Tatsumi, K. *J. Power Sources* **2005**, *146*, 45-50.

(14) Ruther, T.; Huang, J.; Hollenkamp, A. F. *Chem. Commun.* **2007**, 5226-5228.

(15) Vega, J. A.; Zhou, J. F.; Kohl, P. A. *J. Electrochem. Soc.* **2009**, *156*, A253-A259.

(16) Yoshizawa-Fujita, M.; MacFarlane, D. R.; Howlett, P. C.; Forsyth, M. *Electrochem. Commun.* **2006**, *8*, 445-449.

(17) Paddon, C. A.; Jones, S. E. W.; Bhatti, F. L.; Donohoe, T. J.; Compton, R. G. *J. Phys. Org. Chem.* **2007**, *20*, 677-684.

(18) Takei, T. *J. Appl. Electrochem.* **1979**, *9*, 587-593.

(19) Aojula, K. S.; Pletcher, D. *J. Chem. Soc.-Faraday Trans.* **1990**, *86*, 1851-1855.

(20) Xu, J.; Farrington, G. C. *Solid State Ion.* **1994**, *74*, 125-132.

(21) Wang, X. M.; Iyoda, M.; Nishina, T.; Uchida, S. *J. Power Sources* **1997**, *68*, 487-491.

(22) Li, L. F.; Totir, D.; Gofer, Y.; Chottiner, G. S.; Scherson, D. A. *Electrochim. Acta* **1998**, *44*, 949-955.

(23) Massalski, T. B. *Binary Alloy Phase Diagrams*; 2nd ed.; ASM International: Materials Park, OH, 1990; Vol. 3.

(24) Gofer, Y.; Barbour, R.; Luo, Y. Y.; Tryk, D.; Scherson, D. A.; Jayne, J.; Chottiner, G. *J. Phys. Chem.* **1995**, *99*, 11739-11741.

(25) Aurbach, D.; Talyosef, Y.; Markovsky, B.; Markevich, E.; Zinigrad, E.; Asraf, L.; Gnanaraj, J. S.; Kim, H. J. *Electrochim. Acta* **2004**, *50*, 247-254.

(26) Paddon, C. A.; Compton, R. G. *J. Phys. Chem. C* **2007**, *111*, 9016-9018.

(27) Evans, R. G.; Klymenko, O. V.; Price, P. D.; Davies, S. G.; Hardacre, C.; Compton, R. G. *ChemPhysChem* **2005**, *6*, 526-533.

(28) Okoturo, O. O.; VanderNoot, T. J. *J. Electroanal. Chem.* **2004**, *568*, 167-181.

(29) Huang, X. J.; Rogers, E. I.; Hardacre, C.; Compton, R. G. *J. Phys. Chem. B* **2009**, *113*, 8953-8959.

(30) Sun, J.; Forsyth, M.; MacFarlane, D. R. *J. Phys. Chem. B* **1998**, *102*, 8858-8864.

(31) Silvester, D. S.; Aldous, L.; Hardacre, C.; Compton, R. G. *J. Phys. Chem. B* **2007**, *111*, 5000-5007.

(32) O'Mahony, A. M.; Silvester, D. S.; Aldous, L.; Hardacre, C.; Compton, R. G. *J. Chem. Eng. Data* **2008**, *53*, 2884-2891.

(33) Rogers, E. I.; Sljukic, B.; Hardacre, C.; Compton, R. G. *J. Chem. Eng. Data* **2009**, *54*, 2049-2053.

(34) Tokuda, H.; Tsuzuki, S.; Susan, M.; Hayamizu, K.; Watanabe, M. *J. Phys. Chem. B* **2006**, *110*, 19593-19600.

(35) Seddon, K. R.; Stark, A.; Torres, M. J. In *Clean Solvents - Alternative Media for Chemical Reactions and Processing*; Abraham, M. A., Moens, L., Eds.; Amer Chemical Soc: Washington, 2002; Vol. 819; pp 34-49.

(36) Matsumoto, H.; Kageyama, H.; Miyazaki, Y. *Chem. Lett.* **2001**, 182-183.

Chapter 5

The Na/Na^+ Couple in Room Temperature Ionic Liquids

This Chapter focuses on the deposition and stripping processes of sodium in RTILs. Cyclic voltammetry experiments were conducted using solutions of Na^+ ions in twelve different ionic liquids (RTILs) on a nickel microelectrode in order to observe the deposition and stripping of metallic sodium. In most of the liquids the potential window was insufficient to observe the formation and removal of bulk sodium, despite the enlargement of some potential windows in the presence of sodium. However, in the ionic liquids *N*-butyl-*N*-methylpyrrolidinium bis(trifluoromethylsulfonyl)imide ($[C_4mpyrr][NTf_2]$), *N*-ethyldimethylpropyl-ammonium bis(trifluoromethylsulfonyl)-imide ($[N_{2,1,1,3}][NTf_2]$) and *N*-hexyltriethylammonium bis(trifluoromethylsulfonyl)-imide ($[N_{6,2,2,2}][NTf_2]$) the deposition and stripping peaks for the bulk sodium were observed, allowing simulation of the current-voltage curves and extraction of kinetic and thermodynamic data, notably the electrochemical rate constant, k^o, and the formal potential, E_f^0, for the Na/Na^+ couple. Variable temperature measurements also gave quantitative information on the temperature dependence of E_f^0, dE_f^0/dT. Diffusion coefficients for Na^+ ions in the three RTILs are also reported. All parameters are compared and contrasted with that of the Li/Li^+ couple described in Chapter 4, demonstrating that sodium possesses a more positive E_f^0 than lithium in the investigated RTILs, although the difference is markedly less than in solvents such as water or ammonia.

5.1 Introduction

A knowledge of the electrode potentials for redox couples is essential in order to rank their relative oxidising and reducing behaviour in various solvents.[1] The alkali metals are strong reducing agents, and for the majority of systems lithium is seen to be a significantly more powerful reducing agent than sodium. The values of the standard electrode potential, E^o, in aqueous solution are detailed below.

$$Li^+(aq) + e^- \leftrightarrows Li(s) \qquad E^o = -3.04 \text{ V vs SHE}^2 \qquad (5.1)$$

$$Na^+(aq) + e^- \leftrightarrows Na(s) \qquad E^o = -2.71 \text{ V vs SHE}^3 \qquad (5.2)$$

A smaller difference has been observed in the solvent propylene carbonate[4] and dimethyl sulfoxide[5], whilst in liquid ammonia the difference increases to *ca*. 0.45 V.[6]

Room temperature ionic liquids (RTILs), which are comprised mainly of ions, are promising media for the deposition and stripping process for active metals such as lithium and sodium. Their intrinsic electrical conductivity means that no supporting electrolytes are needed in the system and less molecules involved in the solvation process of the species of interest. In addition, their chemical stability as well as their relatively wide potential windows makes the electrodeposition of many active metals possible.[7] The deposition and stripping process of lithium and sodium in chloroaluminate-based ionic liquids has been reported.[8-10] Interestingly, in these solvents the Na/Na$^+$ couple has been observed to have a slightly more negative E^o value than the Li/Li$^+$ couple.[8,10]

In Chapter 4 the Li/Li$^+$ couple in various room temperature ionic liquids and shown that cyclic voltammetry can be used to observe the deposition and stripping of bulk lithium.[11,12] Simulation of the measured current-voltage curves allows the extraction of the formal potential (E_f^0) of the couple as well as the electrode kinetic parameters, namely the electrochemical rate constant (k^o) and the transfer coefficient (α)□.[13]

In haloaluminate melts,[8,10] the formal potential of sodium has been reported to be slightly more negative than that of lithium. We are unaware of any previous reports of the observation of E^0 or E_f^0 for sodium in non-haloaluminate ionic liquids. Given the lack of previous investigation into such fundamental parameters in RTILs, it is of interest to investigate how the difference in thermodynamic reducing power between sodium and lithium in RTILs compares to that seen in water, haloaluminates and other solvents. Accordingly in this chapter we examine the voltammetry of dissolved Na$^+$ cations in a variety of RTILs, some of which allow observation of the deposition and stripping of bulk sodium. Nickel was chosen was the electrode material, as unlike conventional metals such as platinum, extensive alloy formation with Group 1 metals in not expected thus facilitating thorough analysis of the Na/Na$^+$ electrochemical parameters.

Analysis of the voltammetry has allowed us to reference the formal potential (E_f^0) of the Na/Na$^+$ couple to the formal potential of the ferrocene│ferrocenium, added as an internal reference. Comparison with our previous results demonstrates that sodium approaches lithium in its thermodynamic reducing power in RTILs, decreasing the gap observed between the two in aqueous solution, although sodium still possesses a relatively more positive formal potential than that of lithium. Temperature studies are

also described. Data relating to the electrode kinetics of the Na/Na$^+$ couple and the diffusion coefficient of Na$^+$ in various RTILs are reported in this Chapter.

5.2 Results and Discussion

5.2.1 Qualitative experiments

Cyclic voltammetry experiments were carried out by comparing the scans for four ILs ([C_4mim][NTf_2], [C_4mim][OTf], [C_4dmim][NTf_2] and [C_4mpyrr][NTf_2]) containing only 10 mM ferrocene as an internal reference, versus the same solutions containing 0.1 M Na[NTf_2]. These results are displayed in Figure 5. 1. The reversible signal due to the deposition and stripping processes of sodium can clearly be observed in the aprotic ionic liquid [C_4mpyrr][NTf_2] (Figure 5. 1a), which also has a significantly wider potential window than the other ionic liquids. This ionic liquid is also found to be suitable enough to support the Li/Li$^+$ couple as described previously.[12]

The imidazolium-based IL [C_4dmim][NTf_2] has the second widest cathodic limit, due to the absence of the relatively acidic C-2 imidazolium proton, while [C_4mim][NTf_2] and [C_4mim][OTf] possess the smallest cathodic limits, presumably due to preferential reduction of the C-2 proton.[14] The reduction of sodium can be observed in the ILs [C_4mim][NTf_2] and [C_4dmim][NTf_2], although it overlaps with reduction of the IL such that the reversible stripping of sodium cannot be observed in these ILs.

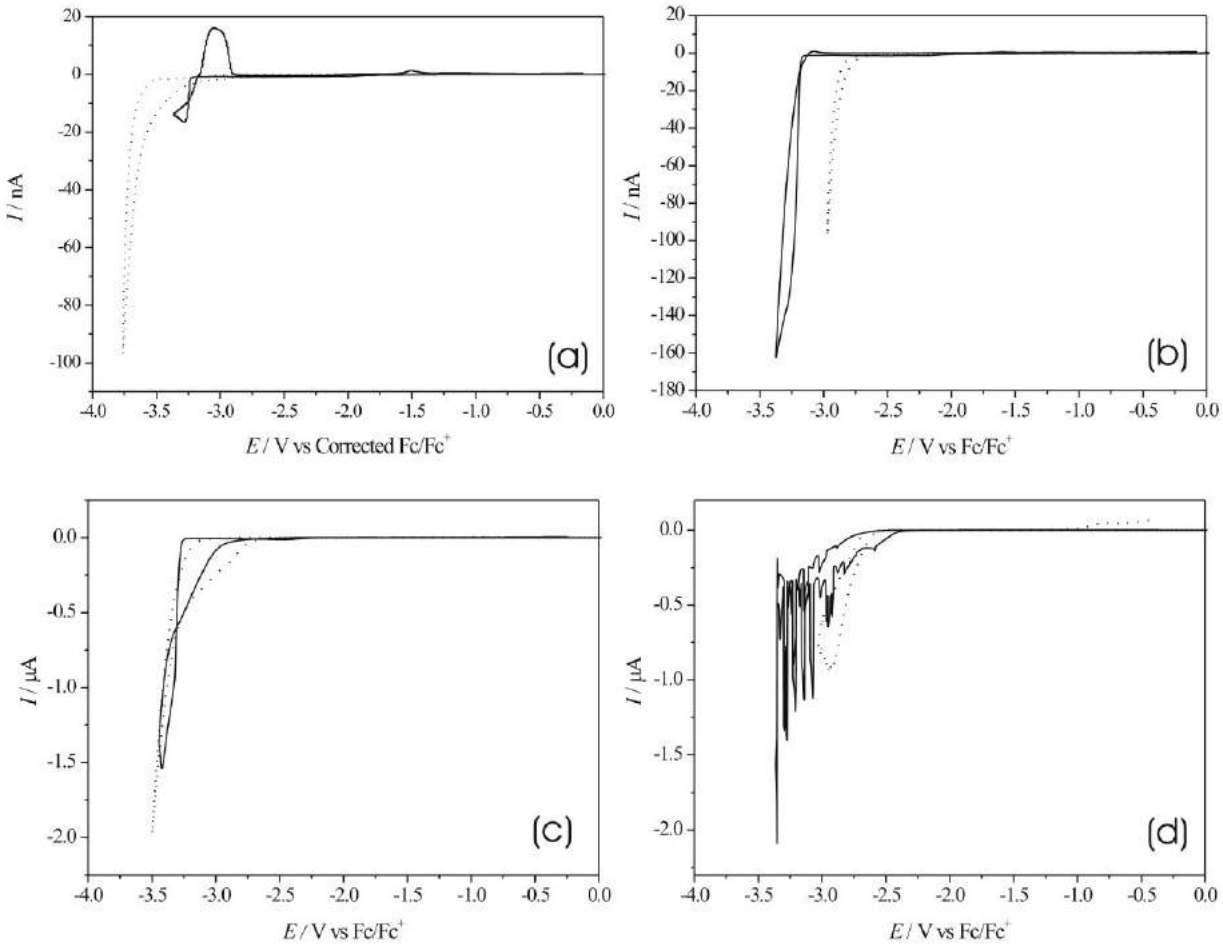

Figure 5. 1: Cyclic voltammograms of the sodium-free ionic liquid (dotted line) and the ionic liquid containing 0.1 M Na[NTf_2] (solid line) for (a) [C_4mpyrr][NTf_2], (b) [C_4dmim][NTf_2], (c) [C_4mim][NTf_2] and (d) [C_4mim][OTf]. All recorded at a 50 μm diameter Ni electrode at 296 K. Scan rate = 10 mV s^{-1}.

Interestingly, both cyclic voltammograms for sodium-free [C_4dmim][NTf_2] and sodium-free [C_4mim][NTf_2] suggest that the electrochemical window is insufficient to support the reduction of sodium, reduction of the IL occurring several hundreds of millivolts in the sodium-free ILs prior to reduction observed in the presence of 0.1 M Na[NTf_2]. This is clearly observed for [C_4dmim][NTf_2] (Figure 5. 1b), and can be observed at the low current density regions of [C_4mim][NTf_2] (Figure 5. 1c). While the figures appear to show a more significant difference between sodium-free and sodium-containing solutions for [C_4dmim][NTf_2], this is solely due to the displayed current

(please note y-axis). If the current density was increased, [C_4dmim][NTf_2] displayed a larger electrochemical window, and the displayed figures are a consequence of [C_4dmim][NTf_2] depositing significantly less sodium than [C_4mim][NTf_2]. It should be noted that all values have been referenced to the formal potential of the Fc/Fc$^+$ couple, as described in the experimental section. Therefore these observations are not due to shifting in the reference electrode.

Similar behaviour has been previously observed by Johnson *et al.* for solutions of [C_2mim]Cl in acetonitrile.[15] Addition of LiCl extended the reductive electrochemical window, with deposition of a layer of lithium being attributed to the stretch of the solvent electrochemical window.[15]

In the presence of sodium, [C_4mim][OTf] displays a reduction starting at a more positive potential than that of the breakdown of the IL itself. However, the voltammogram implies that in the presence of sodium a complicated process occurs at the electrode surface, encompassing sodium reduction overlapped with concurrent electrochemical reduction or chemical oxidation of the IL. It is quite interesting that the reversible signal for Na/Na$^+$ is not observed in [C_4dmim][NTf_2] and [C_4mim][OTf]. In our previous report,[12] both ionic liquids were found to be stable enough to support the clear, reversible deposition and stripping of bulk lithium. These results suggest that the ionic liquids [C_4dmim][NTf_2], [C_4mim][NTf_2] and [C_4mim][OTf] are less suitable for the reduction of sodium, relative to the reduction of lithium.

5.2.2 The Na/Na^+ couple in a wide range of room temperature ionic liquids at 296 K

The deposition and dissolution of the Na/Na^+ couple was investigated in twelve different ionic liquids using a Ni microelectrode (50 μm diameter). The twelve ionic liquids are listed and the observations are summarised in Table 5. 1. Three aprotic ionic liquids $[C_4mpyrr][NTf_2]$, $[N_{2,1,1,3}][NTf_2]$ and $[N_{6,2,2,2}][NTf_2]$ were found to support bulk deposition of sodium as indicated by reversible deposition/stripping signals for sodium in the voltammogram, as shown in Figure 5. 2a-c. In contrast, these signals were not seen in the nine other ionic liquids as they underwent breakdown before the bulk deposition of sodium. In the case of $[C_4dmim][NTf_2]$ and $[C_4mim][NTf_2]$ the breakdown of the ionic liquid overlapped with the deposition of sodium. However, in several ionic liquids such as $[C_4dmim][NTf_2]$, $[C_2mim][NTf_2]$, $[C_4mim][BF_4]$, $[C_4mpyrr][N(CN)_2]$ and $[N_{1,8,8,8}][OTf]$ the underpotential deposition of sodium was observed (discussed later). In addition $[P_{6,6,6,14}][FAP]$, which is known to have an extremely large electrochemical window,[16] could not be investigated due to the extremely low solubility of the $Na[NTf_2]$ salt in this ionic liquid.

Figure 5.2 shows the cyclic voltammograms for 0.1 M $Na[NTf_2]$ in $[C_4mpyrr][NTf_2]$, $[N_{2,1,1,3}][NTf_2]$ and $[N_{6,2,2,2}][NTf_2]$ on a clean Ni microelectrode. The CVs are shown from 0 to -3.4 V (*versus* the corrected Fc/Fc^+ internal reference couple) and recorded at a scan rate of 10 mV s^{-1} and 296 K. All voltammograms show similar characteristics which include underpotential as well as bulk sodium deposition/stripping processes. The primary differences were in the magnitude of the current recorded, which correlates

to different amounts of sodium being deposited and stripped on the timescale of the scan.

Table 5. 1: Experimental observations for the Na/Na$^+$ couple in a range of room temperature ionic liquids (RTILs) at 296 K.

No.	**RTIL**	**Viscosity η/(mPa·s) (T=298 K)**	**Bulk sodium stripping observed?**
a	$[C_4mpyrr][NTf_2]$	89[17]	Yes
b	$[N_{2,1,1,3}][NTf_2]$	-	Yes
c	$[N_{6,2,2,2}][NTf_2]$	167[18]	Yes
d	$[C_4dmim][NTf_2]$	105[17]	No – UPD[b] only
e	$[C_4mim][OTf]$	90[19]	No
f	$[C_4mpyrr][N(CN)_2]$	-	No – UPD[b] only
g	$[C_2mim][NTf_2]$	34[19]	No – UPD[b] only
h	$[P_{14,6,6,6}][FAP]$	464[16]	No
i	$[C_4py][NTf_2]$	60[20]	No
j	$[C_4mim][BF_4]$	-	No – UPD[b] only
k	$[C_4mim][NTf_2]$	52[19]	No
l	$[N_{1,8,8,8}][OTf]$	-	No – UPD[b] only

On the forward scan in all three RTILs displayed clear underpotential deposition (UPD) peaks before the main bulk deposition of sodium occurred. Two clear UPD peaks (at -2.10 and -2.19 V) and one broad feature (at *ca.* -2.65 V) were observed in $[C_4mpyrr][NTf_2]$. In the ionic liquids $[N_{2,1,1,3}][NTf_2]$ and $[N_{6,2,2,2}][NTf_2]$ only two UPD peaks were observed at relatively the same potential at -2.30 and *ca.* -2.60 V, the latter being a broad feature.

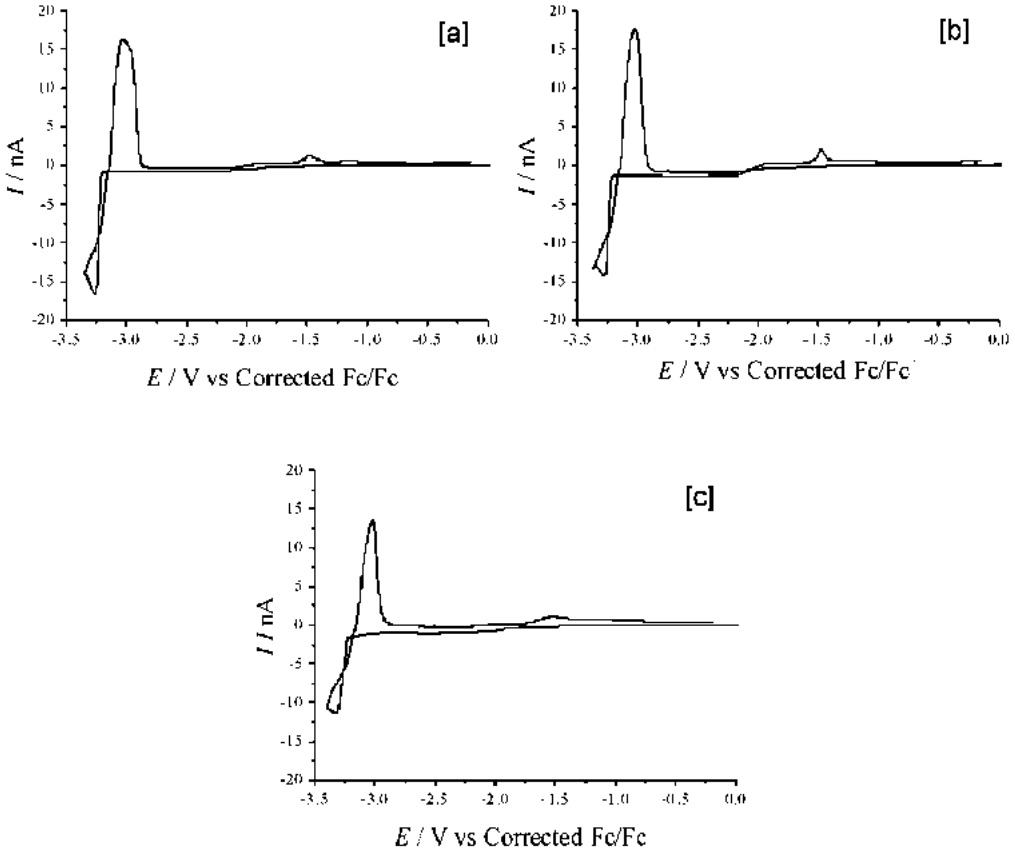

Figure 5. 2: Cyclic voltammograms of 0.1 M Na[NTf_2] in (a) [C_4mpyrr][NTf_2], (b) [$N_{2,1,1,3}$][NTf_2] and (c) [$N_{6,2,2,2}$][NTf_2] on a 50 μm diameter Ni electrode at 296 K Scan rate = 10 mV s^{-1}.

In all three ionic liquids, bulk sodium deposition was observed as a peak at *ca.* -3.2 V. As the scan was reversed to the positive direction, a characteristic 'nucleation loop' (where backward and forward currents cross over) was observed in the bulk deposition region before the stripping of bulk sodium took place. This is consistent with sodium on sodium deposition continuing even after the scan is reversed. The sharp oxidation peak at *ca.* -3.0 V corresponds to the stripping of sodium from the electrode surface while the appearance of the other three small peaks at *ca.* -1.9, -1.5 and -1.2 V are attributed to electrochemical dissolution of the UPD layers. The reversible deposition and dissolution of sodium has also been observed in the buffered haloaluminate system 1-methyl-3-ethylimidazolium chloride/aluminium chloride ([C_2mim][Cl]/$AlCl_3$) on

platinum and tungsten electrodes. However, the UPD signals were not observed in these systems.[21]

Integrating the charge passed during the stripping process for the voltamograms in Figure 5. 2a-c gives the value of 2.8 x 10^{-7} C, 2.4 x 10^{-7} C, and 1.7 x 10^{-7} C for $[C_4mpyrr][NTf_2]$, $[N_{2,1,1,3}][NTf_2]$ and $[N_{6,2,2,2}][NTf_2]$, respectively. These values correspond to approximately 96, 81 and 57 layers of sodium, demonstrating that all systems deposit and strip bulk sodium. In addition, the stripping efficiency, calculated from the ratio between the charge passed during deposition and stripping in Figure 5. 2, are less than a hundred percent in all cases. The highest first cycle stripping efficiency is given by the system in $[C_4mpyrr][NTf_2]$ with a value of 75%, with the more viscous ionic liquid $[N_{6,2,2,2}][NTf_2]$ depositing the least and showing the least stripping efficiency at 57%. Incomplete stripping of bulk sodium has also been observed in buffered 1-methyl-3-ethylimidazolium chloride and aluminium chloride ($[C_2mim][Cl]/AlCl_3$) systems.[22,23]

Various mechanisms have been proposed for incomplete stripping processes at reactive metal deposits.[23] One possibility is the electrochemical or chemical reaction of trace contaminants that are not observed on the Ni surface but can occur at Na. Another concerns the overpotential required to nucleate Na on the Ni surface, which shifts the deposition peak towards the RTIL breakdown potential (*c.f.* complete lack of reversibility for $[C_4mim][NTf_2]$ and $[C_4dmim][NTf_2]$ due to encroachment of the electrochemical window in Figure 5. 1) This results in additional reduction processes occurring, with the effect of this on the stripping efficiency being proportional to the applied charge density, scan rate and cathodic vertex potential, and as such can be

optimised. The three RTILs are similar in terms of chemical functionality, although the stripping results demonstrate that [C_4mpyrr][NTf_2] gave the highest stripping efficiency, which coincides with [C_4mpyrr][NTf_2] also possessing the largest cathodic electrochemical window.[16]

5.2.3 Simulation of the Na/Na$^+$ couple in a wide range of room temperature ionic liquids at 296 K

The CVs for 0.1 M Na[NTf_2] in the three suitable ionic liquids shown in Figure 5. 2 depict similar characteristics to CVs recorded for 0.1 M Li[AsF_6] in the same ionic liquids.[11,12] This opens the possibility for the Na/Na$^+$ couple to be simulated using the same mathematical model previously used to simulate the Li/Li$^+$.[11] Figure 5.3 displays overlays for experimental and simulation data for all voltammograms shown in Figure 5.2. The simulation starts from a region after the initial bulk deposition occurred onwards, because the model incorporates neither the UPD nor the initial nucleation processes. This results in an overestimation of the amount of sodium deposited at peak potential. It also results in larger stripping peaks as the model assumes 100 % stripping efficiency. However, electrochemical parameters can still be extracted from the voltammograms since all the desired information in the voltammogram is contained in the range between the start of the reverse scan (the most anodic data point) and the start of the stripping peak. It can be observed that for all voltammograms very good fits were observed between the experimental and simulation results in this critical region.

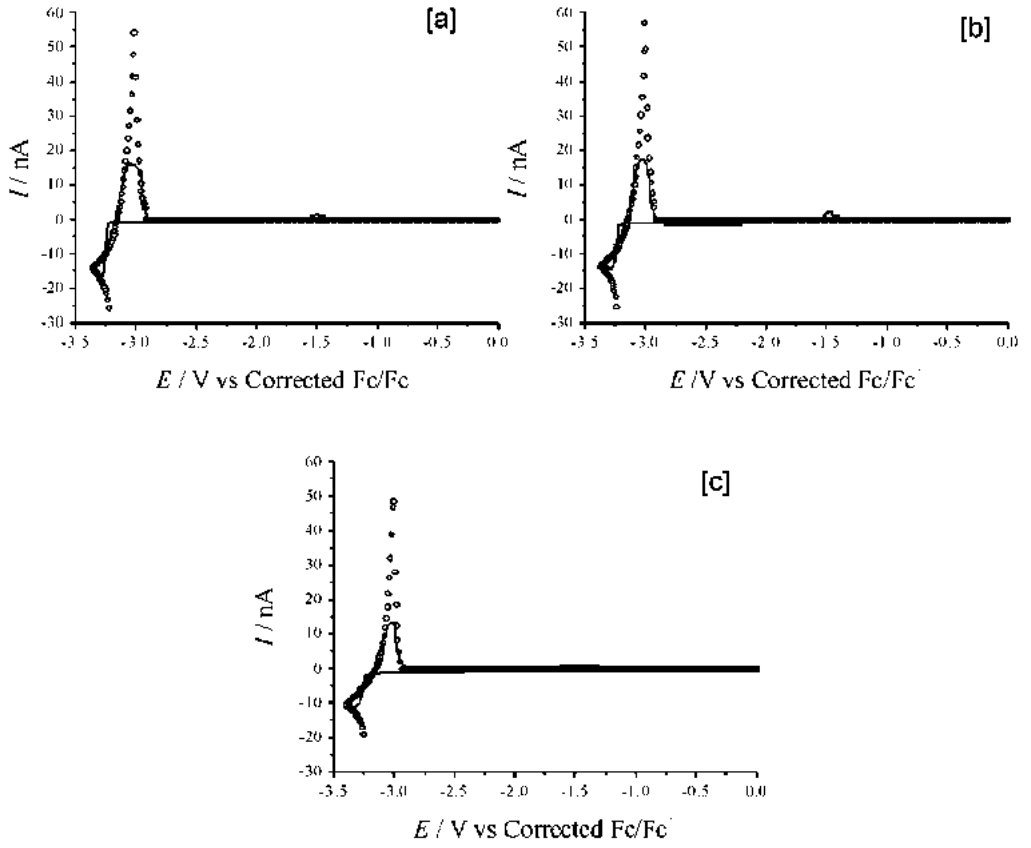

Figure 5. 3: The fit of experimental (-) and simulation (o) data for the cyclic voltammetry experiment using 0.1 M Na[NTf_2] in (a) [C_4mpyrr][NTf_2], (b) [$N_{2,1,1,3}$][NTf_2] and (c) [$N_{6,2,2,2}$][NTf_2] on a 50 μm diameter Ni electrode at 296 K Scan rate = 10 mV s^{-1}.

5.2.4 Comparison of kinetic and thermodynamic paremeters with that a Li/Li$^+$ couple

The electrochemical parameters such as diffusion coefficient (*D*), electrochemical rate constant (k^0), formal potential (E_f^0) and transfer coefficient (α) of the Na/Na$^+$ couple in [C_4mpyrr][NTf_2], [$N_{2,1,1,3}$][NTf_2] and [$N_{6,2,2,2}$][NTf_2] extracted from the experimental data using the mathematical model are presented in Table 5. 2. The table also displayed the parameters for the Li/Li$^+$ as previously reported.[11]

The E_f^0 values are in the range between *ca.* -3.04 V and -3.09 V. Comparison with the E_f^0 values for the Li/Li$^+$ couple in [C$_4$mpyrr][NTf$_2$] (*ca.* -3.26 V),[11] which indicates that in the investigated RTILs sodium approaches lithium in terms of oxidising power. This contrasts with the larger difference observed in aqueous solution, and approaches the trends observed in conventional aprotic media. The shift of the E_f^0 of the Na/Na$^+$ couple to a value more negative than that of the Li/Li$^+$ couple, as reported in haloaluminate ILs,[8,10] was not observed in the investigated RTILs.

Table 5. 2: The electrochemical parameters for the Na/Na$^+$ and Li/Li$^+$ couples in [C$_4$myprr][NTf$_2$], [N$_{2,1,1,3}$][NTf$_2$] and [N$_{6,2,2,2}$][NTf$_2$] determined from the simulation for experimental data at 296 K recorded on a Ni microelectrode.

System	RTIL	Diffusion coefficient 10^8 D/(cm^2·s^{-1})	Rate constant 10^5 k^0/(cm·s^{-1})	Formal potential E_f^0/(V *vs* Corrected Fc/Fc$^+$)	Transfer coefficient α □
Na/Na$^+$	[C$_4$mpyrr][NTf$_2$]	7.8 ± 0.4	1.15 ± 0.06	-3.066 ± 0.003	0.63 ± 0.02
	[N$_{2,1,1,3}$][NTf$_2$]	7.3 ± 0.2	1.12 ± 0.05	-3.044 ± 0.002	0.57 ± 0.03
	[N$_{6,2,2,2}$][NTf$_2$]	5.0 ± 0.2	0.69 ± 0.04	-3.093 ± 0.005	0.47 ± 0.02
Li/Li$^+$	[C$_4$mpyrr][NTf$_2$]	4.5 ± 0.1	1.20 ± 0.05	-3.250 ± 0.010	0.63 ± 0.01
	[N$_{2,1,1,3}$][NTf$_2$]	2.8 ± 0.1	1.00 ± 0.05	-3.234 ± 0.010	0.50 ± 0.01
	[N$_{6,2,2,2}$][NTf$_2$]	1.9 ± 0.1	5.00 ± 0.05	-3.158 ± 0.010	0.50 ± 0.01

The trend in the diffusion coefficients is consistent with the trend in viscosities of the pure RTILs. Since the same concentration of Na[NTf$_2$] was applied to all systems, it is assumed that the trend in viscosity of the ionic liquids containing 0.1 M Na[NTf$_2$] would match the trend in viscosities of the pure ionic liquids as reported at room temperature in Table 5. 1. This means that the viscosity of [N$_{6,2,2,2}$][NTf$_2$] containing 0.1 M Na[NTf$_2$] is still relatively higher than that of [C$_4$mpyrr][NTf$_2$] containing 0.1 M Na[NTf$_2$]. At higher viscosity, the sodium ions diffuse more slowly and this results in

less material being deposited on the electrode surface. From the calculation, it is found that approximately 21 % more material was deposited on the time scale of the scan in [C_4mpyrr][NTf_2] compared to that in [$N_{6,2,2,2}$][NTf_2]. The diffusion coefficient of sodium ions are also found to be higher compared to the diffusion coefficient of lithium ion in all three ionic liquids.[12] This is consistent with the fact that the sodium ion might be expected to have less electrostatic interaction with the [NTf_2]$^-$ anion compared to that for the lithium ion, due to sodium's relatively larger radius. As a consequence, the sodium ions are less solvated and more readily move from one [NTf_2]-solvated form to another in order to reach the electrode surface. Higher diffusivity of sodium ions compared to that of lithium ions has also been observed in chloroaluminate-based ionic liquid[24] as well as in aqueous solution.[25]

5.2.5 The Na/Na$^+$ couple in [C_4mpyrr][NTf_2] at different temperatures

Based on the fact that the Na/Na$^+$ couple performed well in the ionic liquid [C_4mpyrr][NTf_2] in terms of relatively higher stripping efficiency, we then focused on this ionic liquid to further study the sodium electrochemistry at different temperatures. Figure 5. 4 shows the voltammograms of 0.1 M Na[NTf_2] in [C_4mpyrr][NTf_2] at a Ni microelectrode recorded between 296 and 318 K and at 10 mV s^{-1}. All voltammograms show the same general characteristic, including the UPD processes, a bulk deposition, a single sharp stripping peak, and a nucleation loop. The deposition current maximum as well as stripping currents increased as the temperature increased. This is attributed to the corresponding change in the viscosity of the solution, which decreases at higher temperatures lead to an increase in the diffusivity of Na$^+$ in [C_4mpyrr][NTf_2]. The stripping efficiency varied between 56% and 75%.

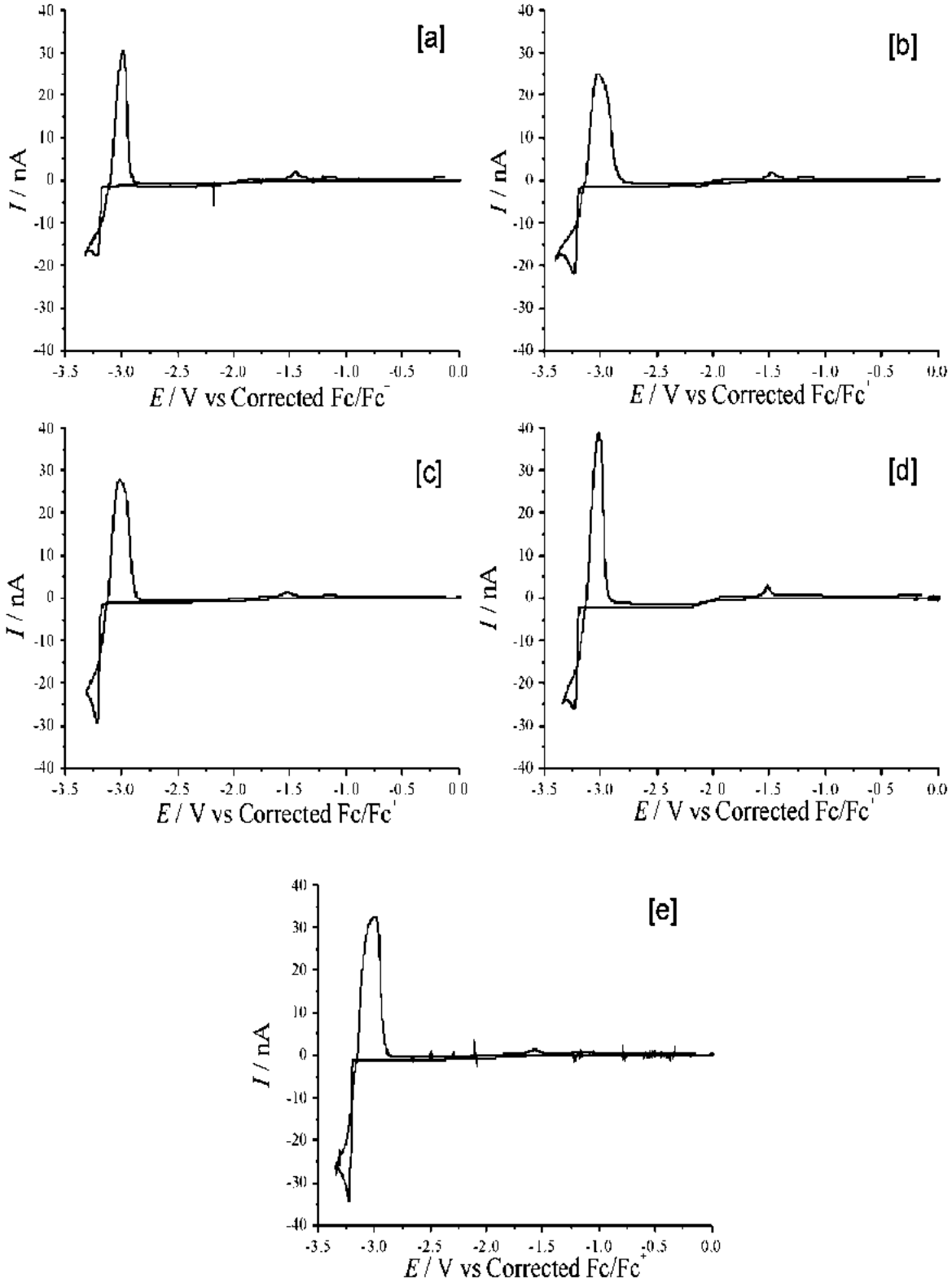

Figure 5. 4: Cyclic voltammograms of 0.1 M Na[NTf_2] in [C_4mpyrr][NTf_2] on a 50 μm diameter Ni electrode at (a) 300 K, (b) 303 K, (c) 308 K, (d) 313 K and (e) 318 K. Scan rate = 10 mV s^{-1}.

5.2.6 Simulation of the Na/Na$^+$ couple in [C$_4$mpyrr][NTf$_2$] at different temperatures

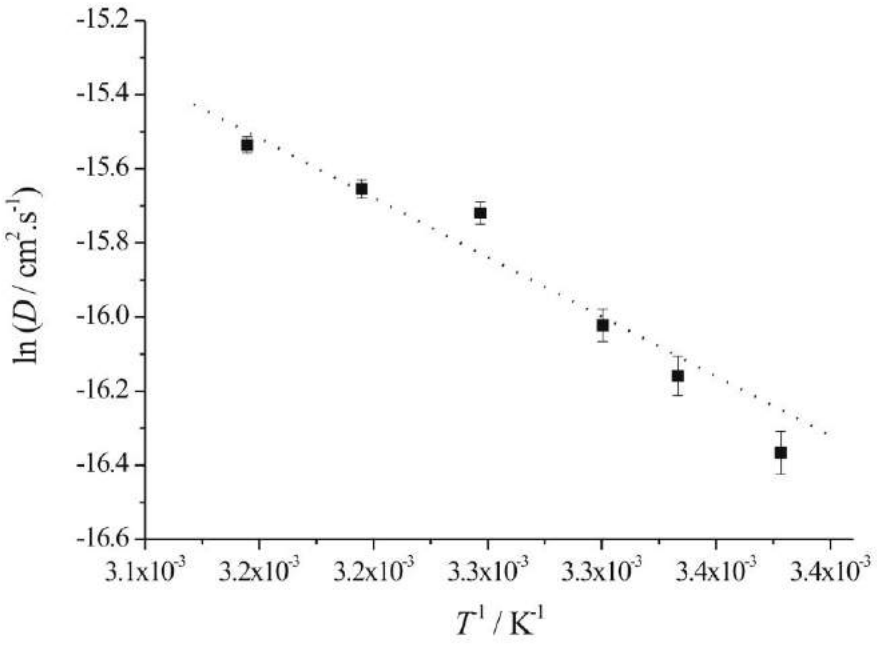

Figure 5. 5: A plot of ln(*D*) versus 1/T. From the line of best fit, d(ln(*D*)/d(1/T) = 3210 K (R = 0.965).

All voltammograms shown in Figure 5. 4 were simulated using the mathematical model described in the theory section. The experimental and simulation results display good fits, barring the typical discrepancies already discussed in Section 5.2.3. The extracted parameters are presented in Table 5. 3.

Table 5. 3: The electrochemical parameters for the Na/Na$^+$ couple in [C$_4$myprr][NTf$_2$] determined from the simulation for experimental data at various temperatures recorded on a Ni microelectrode.

Temperature T / K	Diffusion coefficient $10^7 D$ / cm^2 s^{-1}	Rate constant $10^5 k^0$ / cm s^{-1}	Formal potential E_f^0 / V vs. Corrected Fc/Fc$^+$	Transfer coefficient α
296	0.78 ± 0.04	1.15 ± 0.06	-3.066 ± 0.004	0.635 ± 0.024
300	0.96 ± 0.03	1.48 ± 0.09	-3.034 ± 0.003	0.572 ± 0.019
303	1.10 ± 0.04	1.66 ± 0.05	-3.037 ± 0.005	0.640 ± 0.016
308	1.49 ± 0.03	2.18 ± 0.06	-3.043 ± 0.002	0.615 ± 0.019
313	1.59 ± 0.02	2.45 ± 0.08	-3.051 ± 0.004	0.590 ± 0.016
318	1.79 ± 0.02	2.53 ± 0.07	-3.068 ± 0.004	0.637 ± 0.022

From the table it can be seen that the diffusion coefficient (*D*) and electrochemical rate constant (k^o) of the Na/Na$^+$ couple increase as the temperature increases from 298 to 318 K. The increase in D is due to the decrease in the viscosity of the ionic liquids. The plot of ln(*D*) against T^{-1} in Figure 5. 5 gives an approximate linearity, suggesting that an Arrhenius-type temperature dependency is followed. From the plot, the diffusional activation energy of Na^+ in [C_4mpyrr][NTf_2] can be calculated and gives the value of 26.7 ± 1.6 kJ mol^{-1}. This value is close to the viscosity activation energy ($E_{a,\eta}$ = 25.1 kJ mol^{-1}□[17] measured for [C_4mpyrr][NTf_2] and suggests that classical Stoke-Einstein behaviour is obeyed.[26]

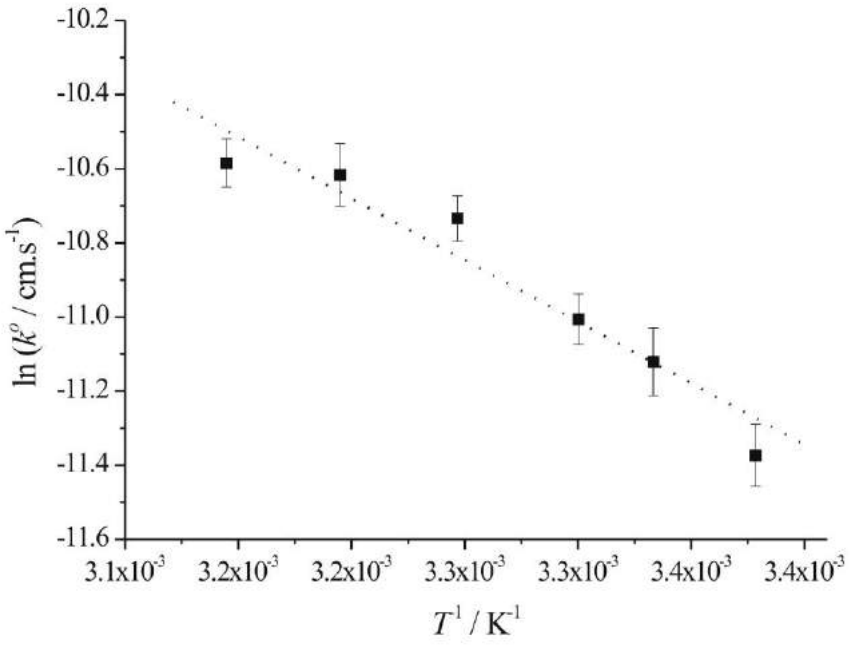

Figure 5. 6: A plot of ln(k^0) versus 1/T. From the line of best fit, d(ln(k^0)/d(1/T) = 3320 K (R = 0.960).

A linear relationship is also observed in Figure 5. 6 for ln(k^0) *versus* T^{-1}, which gives the value of 27.6 ± 3.2 kJ mol^{-1} for the activation energy for the Na/Na$^+$ couple in [C_4mpyrr][NTf_2]. This value is slighty higher compared to that for Li/Li$^+$ (23.7 kJ mol^{-1})[12] in the same ionic liquid. Figure 5.7 shows the formal potential, E_f^0 (versus Fc/Fc$^+$),

extracted from the simulation against temperature. It can be seen that there is an approximate linear relationship between E_f^0 and T which gives the temperature dependency of E_f^0, dE_f^0/dT, as -1.7 (± 0.3) mV K^{-1}. This temperature dependence is almost double than that for the Li$^+$/Li couple in THF.[27] The change in entropy for the deposition of solid sodium metal from solvated sodium ions (Equation 5.2) relative to the Fc/Fc$^+$ couple can then be calculated using Equation 5.3 which gives a value of -164 ± 29 J mol^{-1}K^{-1}.

$$\Delta S^0 = F\frac{dE_f^0}{dT} \tag{5.3}$$

The transfer coefficient (α) for the Li/Li$^+$ couple was previously found to be *ca.* 0.63 over a range of temperatures, while the average for the Na/Na$^+$ couple gave an α close

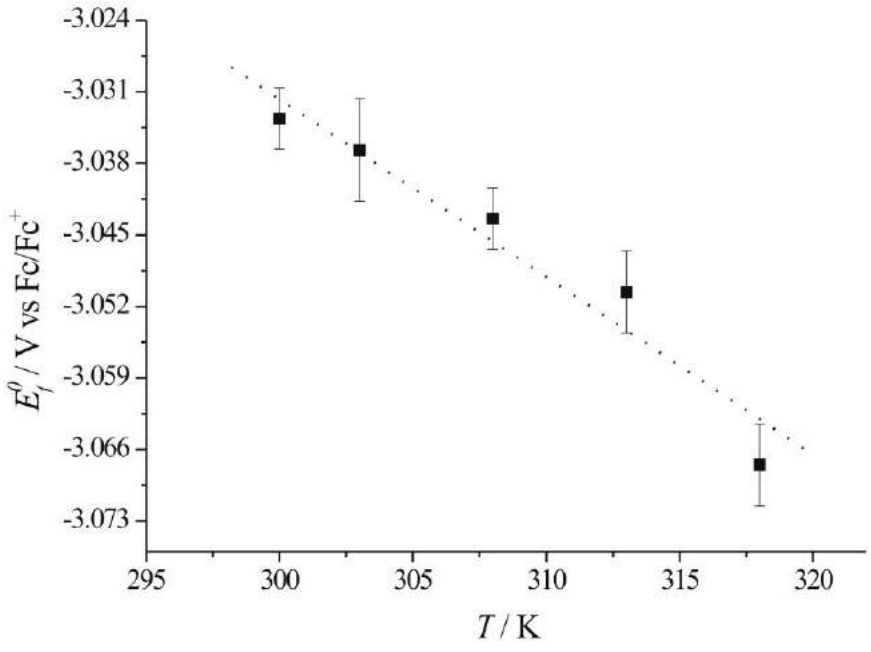

to *ca.* 0.61.

Figure 5. 7: A plot of E_f^0 versus T . From the line of best fit, dE_f^0/dT = -1.7 x 10^{-3} V K^{-1} (R = 0.969).

5.3 Conclusions

The deposition and dissolution of sodium has been investigated in a wide range of ionic liquids using a Ni microelectrode. Three different ionic liquids ($[C_4mpyrr][NTf_2]$, $[N_{2,1,1,3}][NTf_2]$ and $[N_{6,2,2,2}][NTf_2]$) were found to support observation of a reversible Na/Na^+ couple, as indicated by a single stripping peak following bulk deposition of sodium. The electrochemical parameters such as diffusion coefficient (D), electrochemical rate constant (k^o), formal potential (E_f^0) and transfer coefficient (α) for the Na/Na^+ couple observed in those ionic liquids have been extracted following computer simulation of the experimental results. The deposition and dissolution of sodium has been further studied in $[C_4mpyrr][NTf_2]$ to reveal the diffusional activation energy ($E_{a,D}$), activation energy (E_a), dE_f^0/dT and ΔS^0 for the Na/Na^+ couple.

In the next chapter, the deposition and stripping processes of rest members of the Alkali Group I metals (excluding Fr) in an ionic liquid *N*-butyl-*N*-methylpyrrolidinium bis(trifluoromethylsulfonyl)imide ($[C_4mpyrr][NTf_2]$) are discussed. The electrode potential of The Group in the ionic liquid is also presented and compared to that in other solvents.

References

(1) McCafferty, E. *Electrochimica Acta* **2007**, *52*, 5884-5890.

(2) Huston, R.; Butler, J. N. *Journal of Physical Chemistry* **1968**, *72*, 4263-42634.

(3) Smith, E. R.; Taylor, J. K. *Journal of Research of the National Bureau of Standards (United States)* **1940**, *25*, 731-746.

(4) L'Her, M.; Courtot-Coupez, J. *Bulletin de la Societe Chimique de France* **1972**, *9*, 3645-3653.

(5) Das, A. K.; Kundu, K. K. *Journal of The Chemical Society, Faraday Transactions 1: Physical Chemistry in Condensed Phases* **1974**, *70*, 1452-1460.

(6) Johnson, D. A. *Some Thermodynamis Aspects of Inorganic Chemistry* **1982**.

(7) El Abedin, S. Z.; Endres, F. *Chemphyschem* **2006**, *7*, 58-61.

(8) Scordiliskelley, C.; Carlin, R. T. *Journal Of The Electrochemical Society* **1993**, *140*, 1606-1611.

(9) Piersma, B. J.; Ryan, D. M.; Schumacher, E. R.; Riechel, T. L. *Journal Of The Electrochemical Society* **1996**, *143*, 908-913.

(10) Scordiliskelley, C.; Fuller, J.; Carlin, R. T.; Wilkes, J. S. *Journal Of The Electrochemical Society* **1992**, *139*, 694-699.

(11) Wibowo, R.; Jones, S. E. W.; Compton, R. G. *Journal of Chemical and Engineering Data* **2010**, *55*, 1374-1376.

(12) Wibowo, R.; Jones, S. E. W.; Compton, R. G. *Journal Of Physical Chemistry B* **2009**, *113*, 12293-12298.

(13) Compton, R. G.; Banks, C. E. *Understanding Voltammetry*, World Scientific, Singapore, **2007**.

(14) Suarez, P. A. Z.; Consorti, C. S.; de Souza, R. F.; Dupont, J.; Gonçalves, R. S. *Journal of the Brazilian Chemical Society* **2002**, *13*, 106-109.

(15) He, P.; Johnson, K. E. *Canadian Journal of Chemistry* **1997**, *75*, 1730-1735.

(16) O'Mahony, A. M.; Silvester, D. S.; Aldous, L.; Hardacre, C.; Compton, R. G. *Journal Of Chemical And Engineering Data* **2008**, *53*, 2884-2891.

(17) Okutoro, O. O.; VanderNoot, T. J. *Journal Of Electroanalytical Chemistry* **2004**, *568*, 167.

(18) Sun, J.; Forsyt, M.; MacFarlan, D. *Journal of Physical Chemistry B* **1998**, *102*, 8858-8864.

(19) Silvester, D. S.; Aldous, L.; Hardacre, C.; Compton, R. G. *Journal of Physical Chemistry B* **2007**, *111*, 5000-5007.

(20) Tokuda, H.; Tsuzuki, S.; Susan, M. A. B. H.; Hayamizu, K.; Watanabe, M. *Journal of Physical Chemistry B* **2006**, *110*, 19593-19600.

(21) Fuller, J.; Carlin, R. T.; Osteryoung, R. A. *Journal Of Electrochemical Society* **1996**, *143*, L145-L147.

(22) Riechel, T. L.; Wilkes, J. S. *Journal Of The Electrochemical Society* **1992**, *139*, 977-981.

(23) Gray, G. E.; Kohl, P. A.; Winnick, J. *Journal Of Electrochemical Society* **1995**, *142*, 3636-3642.

(24) Koronaios, P.; Osteryoung, R. A. *Journal Of The Electrochemical Society* **2001**, *148*, E483-E488.

(25) Leaist, D. G.; Goldik, J. *Journal of Solution Chemistry* **2001**, *30*, 103-118.

(26) Huang, X. J.; Rogers, E. I.; Hardacre, C.; Compton, R. G. *Journal Of Physical Chemistry B* **2009**, *113*, 8953-8959.

(27) Paddon, C. A.; Ward-Jones, S. E.; Bhatti, F. L.; Donohoe, T. J.; Compton, R. G. *Journal of Physical Organic Chemistry* **2007**, *20*, 677-684.

Chapter 6

The K/K^+, Rb/Rb^+ and Cs/Cs^+ Couples in *N*-butyl-*N*-methyl-pyrrolidinium bis(trifluoromethylsulfonyl)imide ($[C_4mpyrr][NTf_2]$)

This Chapter presents a continuation study of the redox couples M/M^+ (K/K^+ , Rb/Rb^+ and Cs/Cs^+) of the Group I alkali metals in ionic liquid. Cyclic voltammetric experiments in the ionic liquid *N*-butyl-*N*-methylpyrrolidinium bis(trifluoromethylsulfonyl)imide ($[C_4mpyrr][NTf_2]$) and subsequent simulation of the data has allowed the determination of the formal potential (E^0_f *vs.* ferrocene/ferrocenium), standard electrochemical rate constant (k^0) and transfer coefficient (α) for each couple in the Group. The diffusion coefficients (D) of the M^+ cation have also been estimated. The observed trends in E_f^0 in $[C_4mpyrr][NTf_2]$ are remarkably similar to the established trends in the common battery electrolyte, propylene carbonate.

6.1 Introduction

The Group I alkali metals, consisting of Lithium (Li), Sodium (Na), Potassium (K), Rubidium (Rb), Caesium (Cs) and Francium (Fr) are all extremely strong reducing agents, although their relative reducing ability depends upon which solvents they are in contact with. Their electrochemistry is of importance to a number of areas, most notably with respect to batteries and energy storage.[1,2]

Ionic liquids (ILs) generally possess extremely low volatility and inherent conductivity, and can possess good chemical robustness, non-flammability (with respect to common organic solvents) and wide electrochemical windows, amongst other desirable properties.[3,4] The IL N-butyl-N-methylpyrrolidinium bis(trifluoromethylsulfonyl)imide ([C$_4$mpyrr][NTf$_2$]), possessing the above said properties, has allowed us the investigate the electrochemical redox properties of the first five Group I metals in a non-haloaluminate IL for the first time; by necessity the radioactive and extremely rare Francium had to be excluded.

In the previous chapters, we have discussed in-depth studies on the behaviour of the Li/Li$^+$ (Chapter 4) [5,6] and Na/Na$^+$(Chapter 5) [7]redox couple in a range of ILs at Platinum (Pt) and Nickel (Ni) microelectrodes. No evidence of alloy formation between the Group I metals and Ni was observed, while [C$_4$mpyrr][NTf$_2$] gave the most defined metal deposition and stripping processes, allowing accurate determination of fundamental parameters such as E_f^0, k^0 and α. In this Chapter we complete the Group I series by investigating the K/K$^+$, Rb/Rb$^+$ and Cs/Cs$^+$ redox couples in [C$_4$mpyrr][NTf$_2$] at a Ni microelectrode. By focussing attention upon the reverse sweep of the CV, when the microelectrode has been electrodeposited with the Group I metal, the system behaves as an M/M$^+$ half-cell, yielding

fundamental values that have been accurately referenced with respect to ferrocene/ferrocenium.

6.2 Results and Discussion

6.2.1 Voltammetric Results

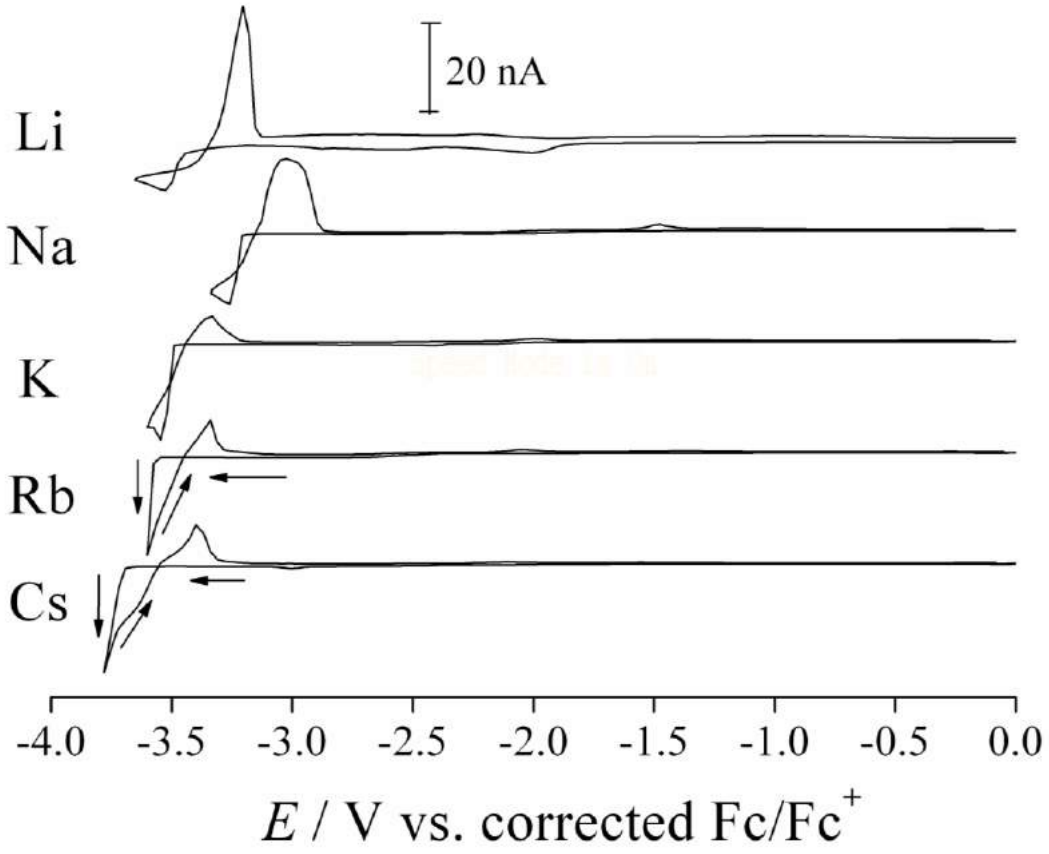

Figure 6. 1: Cyclic voltammograms recorded for a 0.1 M solution of the relevant metal-$[NTf_2]$ salt in $[C_4mpyrr][NTf_2]$ at a 50 μm diameter Ni electrode. Scan rate = 10 mV s^{-1}.

Figure 6. 1 displays a comparison of CVs for all five Group I Alkali metals, recorded for 0.1 M of the relevant metals $[NTf_2]$-salt dissolved in $[C_4mpyrr][NTf_2]$ and recorded at 10 mV s^{-1} at a Ni microelectrode. Underpotential deposition (UPD) processes[5-7] were observed for all five Group I metals in the region of -2.0 to -3.0 V, and can be observed

most clearly in Figure 6. 1 for Li^+. Relatively sharp reduction profiles were observed for all metals at potentials more negative than -3.0 V, consistent with an overpotential being required for the initial nucleation of the Group I metal to occur on Ni, followed by the rapid deposition of metal-on-metal. The local concentration of the metal ion is therefore depleted, and in the case of Li^+, Na^+ and K^+ this leads to a characteristic peak shape corresponding to a mass transport controlled region.[8] All scans also possess characteristic nucleation loops (where backward and forward currents cross over), as on the reverse scan Group I metal is still being deposited on Group I metal at potentials positive to that required for the initial nucleation of the metal on Ni. In the case of Rb^+ and Cs^+, the reduction potentials for these metals were significantly more negative than that of Li^+, Na^+ and K^+, such that nucleation occurred only a few millivolts prior the reduction process of [C$_4$mpyrr][NTf$_2$]. Therefore the scan had to be reversed shortly after nucleation, and a considerable amount of metal was instead deposited on the reverse scan (direction of the scan indicated by arrows in the Figure). The charge passed under the reduction process can be used to quantify the amount of alkali metal reduced at the electrode surface. Assuming the metal is deposited as layers with the same geometric area as that of the Ni microelectrode, the reduction charge calculated for the bulk reduction peak in the voltammograms in Figure 6. 1 indicates that approximately 63, 96, 34, 33 and 68 layers of Li, Na, K, Rb and Cs were deposited, demonstrating that all systems deposit bulk metal on the Ni electrode.

All systems also display sharp oxidation peaks which correspond to the stripping off of metal from the electrode surface. Therefore, the CV response after the bulk deposition peak and prior to the bulk stripping peak (*e.g.* where the CV crosses over the x-axis, corresponding to zero net current being passed) corresponds to the system behaving as an

M/M$^+$ interface, as opposed to Ni/M$^+$. The response of the system in this region is therefore a feature of the fundamental parameters of the M/M$^+$ couple in the IL. The CVs were simulated as described below in order to quantify the parameters.

6.2.2 Simulation Results

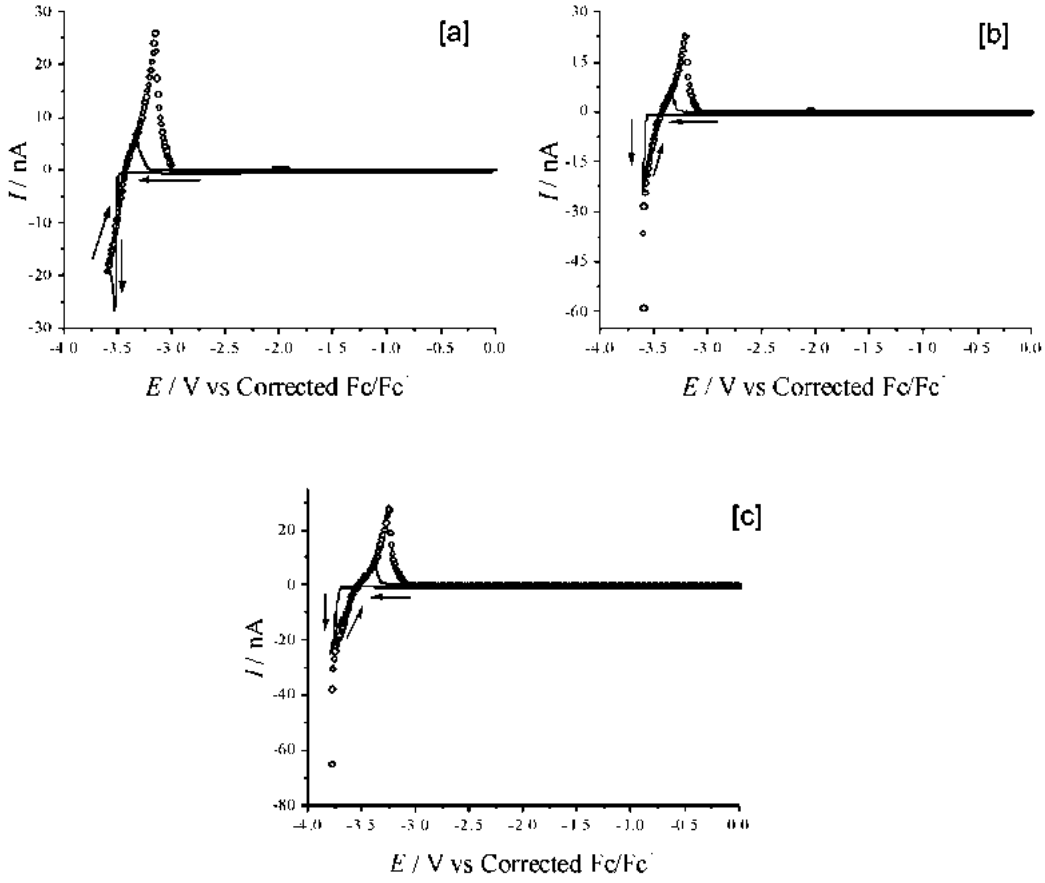

Figure 6. 2: The best fit of experimental (-) and simulation (○) data for the CV of 0.1 M (a) K[NTf$_2$], (b) Rb[NTf$_2$], and (c) Cs[NTf$_2$] in [C$_4$mpyrr][NTf$_2$] on 50 µm diameter Ni electrode. Scan rate = 10 mV·s^{-1}.

The details of the simulation were explained in Chapter 1. Full details of the development of the simulation model,[9] as well as its application to experimental results have been previously demonstrated.[5-7,10,11] The simulation model was applied to the K/K$^+$, Rb/Rb$^+$ and Cs/Cs$^+$ systems in order to extract the fundamental electrochemical parameters of the

couples. Figure 6. 2 (a-c) display overlays of the experimental results as well as best fits for the simulations for K/K$^+$, Rb/Rb$^+$ and Cs/Cs$^+$, respectively. The simulation of the Li/Li$^+$ [5] and Na/Na$^+$ [7] systems has been reported in Chapter 4 and Chapter 5 respectively.

The simulation can be split into three areas; the Alkali metal deposition peak, the Alkali metal stripping peak, and the region of zero current in between the two processes. The simulated alkali metal ion deposition peaks do not precisely match the experimental results, as shown in Figure 6. 2 (a-c). This is because the simulated results do not take into account the nucleation process, replication of which is not required for an investigation of solely M/M$^+$ parameters. The simulation was started in the region where initial nucleation was observed to occur in the experimental results. The physical parameters were put into the simulations, and the amount of metal deposited was solved. By varying the parameters a good fit could be achieved on the reverse scan, which also resulted in the simulation generating the appropriate concentration gradient for M$^+$ extending out from the electrode surface required for a good fit during the zero current cross-over region (occurring *ca.* 30 s after deposition is started).

As the shape of the reduction peak after the initial nucleation process is mass transfer controlled, it is also extremely sensitive to the diffusion coefficient, *D*, of the ion M$^+$. Fitting to the experimental reduction process for K$^+$ (as shown in Figure 6. 2a) was used to accurately determine *D*. The *D* for Li$^+$ [5] and Na$^+$ [7] have been previously reported. However, since clear mass transfer controlled regions could not be observed in the case of Rb/Rb$^+$ and Cs/Cs$^+$, the diffusion coefficient could not be independently determined. The *D* values for Li$^+$, Na$^+$ and K$^+$ were found to be linear with respect to 1/*r*, where *r* is the radius of the ion. This allowed us to extrapolate the trend and estimate *D* values for Rb$^+$

and Cs^+ based upon their known *r* values. These estimated *D* values were found to work well in the subsequent simulations.

For all of the metals the simulation displays stripping peaks significantly higher than that of the experimental result, as the simulation assumes 100 % stripping efficiency. However, the foot of the stripping peak fitted well in all cases, indicating that during the reverse scan bulk Alkali metal was present on the surface of the electrode. Therefore, in the potentials between bulk deposition and bulk stripping, the electrode is behaving as an Alkali metal electrode, M, in contact with a precisely defined local concentration of its ion, M^+. The current in the crossover region area (*ca.* ±100 mV from the x-axis crossover potential) is a function of both oxidation and reduction processes occurring appreciably at the M/M^+ interface, as defined by Butler-Volmer kinetics and is therefore sufficiently sensitive to E_f^0, α and k^0 for these values to be determined accurately by focussing on the simulation of this region. The values of E_f^0, α and k^0 were therefore varied until the best fit was obtained between simulation and experimental results for the tail end of metal deposition, the crossover region and the foot of the oxidation peak. The good fit obtained between experimental and simulation data is clearly observed in Figure 6. 2 (a-c).

Table 6. 1 presents the electrochemical parameters which include diffusion coefficient (*D*), electrochemical rate constant (k^0), formal potential ($E_f{}^0$), and transfer coefficient (α) required for the best fits shown in Figure 6. 2. The data for the Li/Li^+ [5] and Na/Na^+ [7] redox couples are those reported previously.

From the Table the increase in diffusion coefficient (*D*) down the group can clearly be observed for Li^+, Na^+, and K^+. It should be recalled that D was estimated for Rb^+ and Cs^+.

Similar trends down Group I have previously been observed in aqueous[12,13] and methanol solutions.[14] The electrochemical rate constant (k^0) was also found to decrease slightly down the Group. The transfer coefficients are all above 0.5 implying a late transition state, presumably due to the M^+ ion being largely desolvated. The formal potential (E_f^0) displays a similar trend to that reported for a variety of other solvents (discussed below). In this Table E_f^0 is reported *vs.* Fc/Fc^+, where the formal potential of Fc/Fc^+ has been carefully corrected with respect to the discrepancies in diffusion coefficients that can arise between redox couples in ILs,[15] and this correction method has been described previously.[7]

Table 6. 1: The electrochemical parameters for the Alkali metal redox couples in $[C_4myprr][NTf_2]$, extracted by simulation of the experimental data, where D is the Diffusion coefficient, k^0 is the standard electrochemical rate constants, E_f^0 is the formal potential, α is the transfer coefficient and ΔG^0_{solv} is the Gibbs energy of solvation in H_2O or $[C_4myprr][NTf_2]$.

M/M^+	$10^8 D$ / ($cm^2 \cdot s^{-1}$)	$10^5 k^0$ / ($cm \cdot s^{-1}$)	E_f^0 / (V *vs.* Corrected Fc/Fc^+)	α	$\Delta G^o_{solv(H_2O)}$ / (kJ mol^{-1}) Φ	$\Delta G^o_{solv(IL)}$ *vs.* Fc/Fc^+/ (kJ mol^{-1})
Li/Li^+ ‡	4.5 ± 0.1	1.20 ± 0.05	-3.250 ± 0.010	0.63 ± 0.01	-509	-336 ± 10
Na/Na^+ ‡	7.8 ± 0.4	1.15 ± 0.06	-3.066 ± 0.003	0.63 ± 0.02	-409	-278 ± 10
K/K^+	10.2 ± 0.5	0.3 ± 0.05	-3.359 ± 0.005	0.80 ± 0.05	-335	-157 ± 10
Rb/Rb^+	10.9 ± 0.5 §	0.3 ± 0.04	-3.367 ± 0.003	0.75 ± 0.05	-314	-132 ± 10
Cs/Cs^+	11.5 ± 0.5 §	0.2 ± 0.05	-3.472 ± 0.003	0.75 ± 0.05	-283	-86 ± 10

‡ The data for Li/Li^+ and Na/Na^+ are taken from references [5] and [7], respectively
§ D values estimated from a plot of Li^+, Na^+ and K^+ D values *vs.* $1/r$. where r is the ionic radii
Φ $\Delta G^o_{solv(H_2O)}$ values from reference [21]

The trend in formal potential of the metal redox couples has been reported for a number of solvents.[16] However, quantitative comparison is made difficult by the lack of a rigorous reference potential for ILs.[11,15,17] While extensive work aimed primarily at Lithium and energy storage applications has been reported in ILs[18-20], few quantitative values have been published that can be compared with. Wilkes *et al.* carried out a study aimed at the reduction potentials of the Alkali metals in a neutral, buffered $[C_2mim]Cl:AlCl_3$ melt,

although this was limited to the reduction potentials for amalgam formation at a Hg-film electrode, due to the electrochemical window of the melt not supporting deposition of the pure metal.[21]

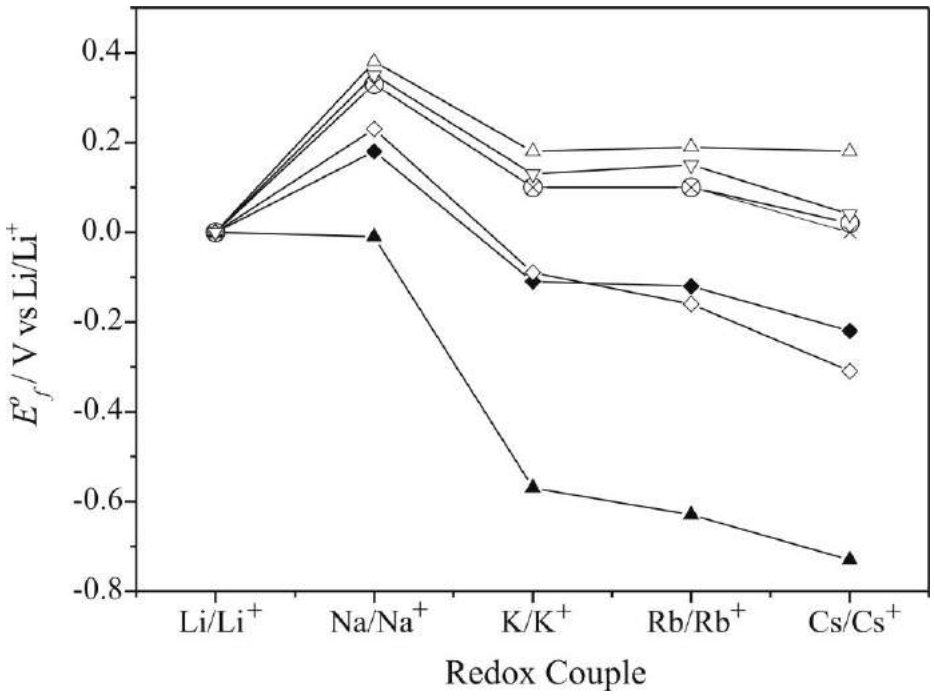

Figure 6. 3: The plot of alkali metal redox couple formal potential relative to the Li/Li$^+$ couple in (△) 60% DMSO/40% H_2O (▽) DMSO, (○) H_2O, (×) DMF, (◇) propylene carbonate, (◆) [C_4mpyrr][NTf_2] (this work) and (▲) neutral, buffered [C_4mim]Cl:$AlCl_3$ melt, at a Hg film electrode (from reference [21]). All values with hollow symbols taken from reference [16].

Figure 6. 3 displays a comparison of the trends in E_f^0 for the Group I metals relative to the E_f^0 of the Li/Li$^+$ couple in the same medium. It can be observed that the trend in formal potential in H_2O, DMSO and DMF,[16] going from most positive to negative, is Na > K > Rb > Cs > Li. In the case of amalgam formation potentials in [C_2mim]Cl:$AlCl_3$,[21] the trend goes down the group, such that Li > Na > K > Rb > Cs. In [C_4mpyrr][NTf_2] the trend in E_f^0 displays a remarkable similarity to propylene carbonate, with Na > Li > K ≈ Rb > Cs.

The trend in solvation energy can be estimated by using the obtained E_f^0 values. A Born-Haber cycle can be used to calculate the Gibbs energy of solvation, ΔG^o_{solv}, by comparison

with the known values for the Gibbs energy of ionisation and sublimation, as well as the single-electrode reduction potential.[21] Lacking a reliable single-electrode reference potential for $[C_4mpyrr][NTf_2]$, as well as knowledge of activity coefficients in the IL environment, the relative solvation energies can nevertheless be estimated *vs.* Fc/Fc^+ by using the obtained E_f^0 *vs.* Fc/Fc^+ values for the Alkali metals and assuming $E_f^0 = E^0$. Table 6. 1 displays the calculated $\Delta G^o_{solv(IL)}$ *vs.* Fc/Fc^+ for the metals in $[C_4mpyrr][NTf_2]$, as well as the literature values for $\Delta G^o_{solv(H_2O)}$ as comparison. Figure 6. 4 displays a plot of $\Delta G^o_{solv(IL)}$ *vs.* Fc/Fc^+ against $\Delta G^o_{solv(H_2O)}$, which indicates that the smaller ions are the most strongly solvated in both systems. A line of best linear fit has been included in order to guide the eye. However, it should be noted that a perfect linear fit would not be expected unless solvation behaviour is identical for the Group I ions in both H_2O and $[C_4mpyrr][NTf_2]$.

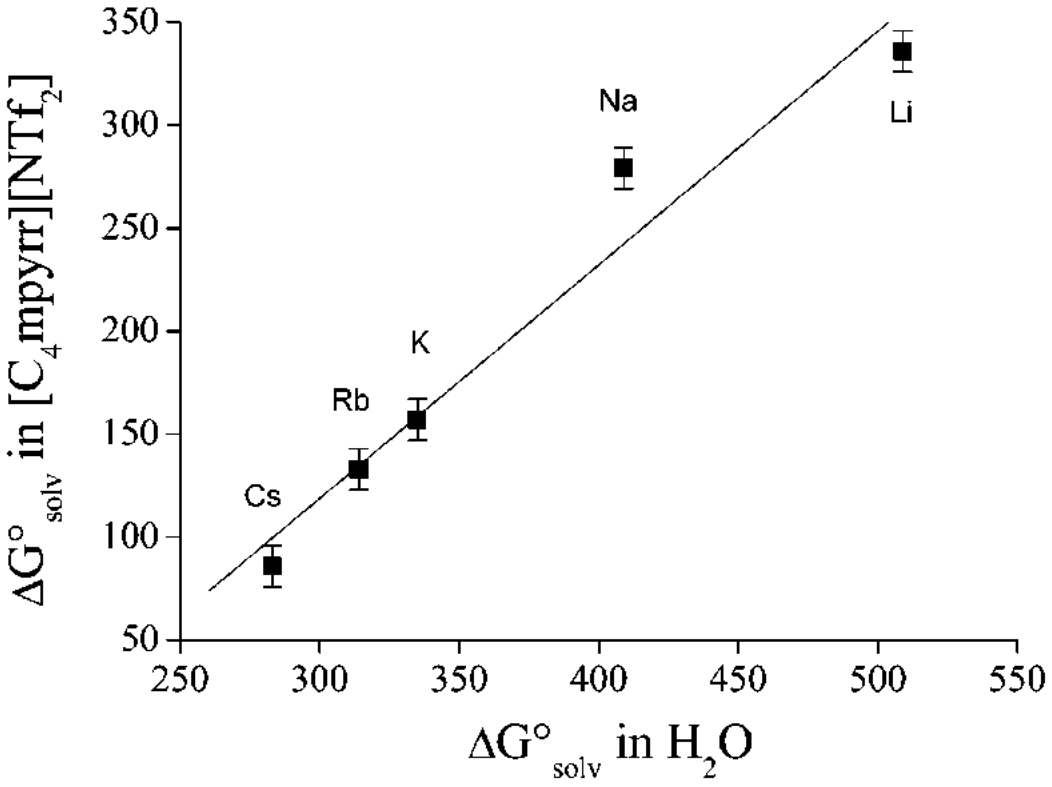

Figure 6. 4: The plot of the estimated Gibbs energy of solvation of the Alkali metal ions in $[C_4mpyrr][NTf_2]$ against the known Gibbs energy of solvation for the ions in aqueous solution.

6.3 Conclusions

In summary, the deposition and dissolution of all five Group I Alkali metal redox couples (M/M^+) have been investigated in the ionic liquid N-butyl-N-methylpyrrolidinium bis(trifluoromethylsulfonyl)imide ($[C_4mpyrr][NTf_2]$) using a Ni microelectrode. All systems displayed chemically reversible behaviour which was successfully simulated using a mathematical model and the electrochemical rate constant (k^0), formal potential (E^0_f) transfer coefficient (α) and diffusion coefficient (D) have been extracted by simulation of the CV. This constitutes the first electrochemical investigation of an entire Group in an ionic liquid. The reducing powers of the alkali metals in $[C_4mpyrr][NTf_2]$ follow the trend previously observed for propylene carbonate, with Na > Li > K ≈ Rb > Cs.

The next Chapter will discuss the *in situ* electrochemical-X-ray photoelectron spectroscopy in monitoring the electrodeposition process of potassium in an ionic liquid.

References

(1) Armand, M.; Endres, F.; MacFarlane, D. R.; Ohno, H.; Scrosati, B. *Nature Materials* **2009**, *8*, 621-629.

(2) Wishart, J. F. *Energy & Environmental Science* **2009**, *2*, 956-961.

(3) Silvester, D. S.; Compton, R. G. *Zeitschrift Fur Physikalische Chemie-International Journal Of Research In Physical Chemistry & Chemical Physics* **2006**, *220*, 1247-1274.

(4) Liu, H. T.; Liu, Y.; Li, J. H. *Physical Chemistry Chemical Physics*, *12*, 1685-1697.

(5) Wibowo, R.; Jones, S. E. W.; Compton, R. G. *Journal Of Physical Chemistry B* **2009**, *113*, 12293-12298.

(6) Wibowo, R.; Jones, S. E. W.; Compton, R. G. *Journal Of Chemical And Engineering Data* **2010**, *55*, 1374-1376.

(7) Wibowo, R.; Aldous, L.; Rogers, E. I.; Jones, S. E. W.; Compton, R. G. *Journal Of Physical Chemistry C*, *114*, 3618-3626.

(8) Compton, R. G.; Banks, C. E. *Understanding Voltammetry*, World Scientific, Singapore, 2007.

(9) Jones, S. E. W.; Chevallier, F. G.; Paddon, C. A.; Compton, R. G. *Analytical Chemistry* **2007**, *79*, 4110-4119.

(10) Paddon, C. A.; Jones, S. E. W.; Bhatti, F. L.; Donohoe, T. J.; Compton, R. G. *Journal Of Physical Organic Chemistry* **2007**, *20*, 677-684.

(11) Rogers, E. I.; Silvester, D. S.; Jones, S. E. W.; Aldous, L.; Hardacre, C.; Russell, A. J.; Davies, S. G.; Compton, R. G. *Journal Of Physical Chemistry C* **2007**, *111*, 13957-13966.

(12) Harned, H. S.; Blander, M.; Hildreth, C. L. *Journal Of The American Chemical Society* **1954**, *76*, 4219-4220.

(13) Leaist, D. G.; Goldik, J. *Journal Of Solution Chemistry* **2001**, *30*, 103-118.

(14) Chowdhuri, S.; Chandra, A. *Journal Of Chemical Physics* **2006**, *124*,

(15) Rogers, E. L.; Silvester, D. S.; Poole, D. L.; Aldous, L.; Hardacre, C.; Compton, R. G. *Journal Of Physical Chemistry C* **2008**, *112*, 2729-2735.

(16) Marcus, Y. *Pure And Applied Chemistry* **1985**, *57*, 1129-1132.

(17) Silvester, D. S.; Rogers, E. I.; Compton, R. G. In *Electrodeposition from Ionic Liquids*; Endres, F., Abbot, A. P., MacFarlane, D. R., Eds.; WILEY-VCH Verlag GmbH & Co. KGaA: Weinheim, 2008.

(18) Howlett, P. C.; MacFarlane, D. R.; Hollenkamp, A. F. *Electrochemical And Solid State Letters* **2004**, *7*, A97-A101.

(19) Katayama, Y.; Morita, T.; Yamagata, M.; Miura, T. *Electrochemistry* **2003**, *71*, 1033-1035.

(20) Endres, F.; El Abedin, S. Z.; Borissenko, N. *Zeitschrift Fur Physikalische Chemie-International Journal Of Research In Physical Chemistry & Chemical Physics* **2006**, *220*, 1377-1394.

(21) Scordiliskelley, C.; Fuller, J.; Carlin, R. T.; Wilkes, J. S. *Journal Of The Electrochemical Society* **1992**, *139*, 694-699.

Chapter 7

In situ Electrochemical-X-Ray Photoelectron Spectroscopy: Potassium Electrodeposition from an Ionic Liquid

In this Chapter, the use of simultaneous electrochemistry and X-ray photoelectron spectroscopy to monitor the electrodeposition of potassium is developed. The real time electrodeposition of potassium has been monitored for the first time in an ionic liquid using *in situ* electrodeposition-X-ray Photoelectron Spectroscopy (XPS); this advance exploits the near zero volatility of some ionic liquids so enabling voltammetry to be carried out in these solvents *in vacuo*. The ionic liquid used was *N*-butyl-*N*-methylpyrrolidinium bis(trifluoromethylsulfonyl)imide ($[C_4mpyrr][NTf_2]$), and electrodeposition occurred at a nickel mesh electrode.

The work presented in this chapter has been published in *Chemical Physics Letters*.[1]

7.1 Introduction

Ionic liquids (ILs) generally possess extremely low vapour pressures,[2] as well as inherent conductivity and the ability to support relatively reactive metal deposits.[3] These characteristics have facilitated their application in a number of unique *in vacuo* techniques,[4,5] including *in situ* X-Ray Photoelectron spectroscopy (XPS) of ionic liquids and various solutes.[4,6-23] This has recently been expanded to *in situ* electrochemical-XPS measurements, a form of *in vacuo* spectroelectrochemical measurement.[10,23-25]

Foelske-Schmitz *et al.* investigated the electrochemistry of Highly Orientated Pyrolytic Graphite (HOPG) in the ionic liquid $[C_4mim][BF_4]$, which was performed in the XPS chamber, the excess liquid removed from the carbon surface, the carbon transferred to the sample holder and XPS performed.[10] Silvester performed XPS measurements in conjunction with *ex situ* electrochemical measurements in order to probe the bromide content of $[C_4mpyrr][NTf_2]$.[21]

Licence *et al.* have carried out *in situ* electrochemical-XPS measurements using two-electrode systems containing IL droplets, and monitored the oxidation of a copper wire to Cu(I)[24], reduction of Fe(III) to Fe(II)[25] and the XPS induced charging of the IL itself.[23]

Weingarth *et al.* have also recently accomplished *in situ* electrochemical-XPS measurements, whereby the X-ray beam was focussed on the interface between the IL and a Pt electrode, a potential difference applied and spectra recorded at the polarised interface; this represented the first, and to the authors knowledge only reported

application to date of a three-electrode electrochemical set-up for *in situ* electrochemical-XPS measurements on ILs.[26]

In previous chapters, the electrodeposition of the Alkali Group I metals at Pt and Ni electrodes in the IL N-butyl-N-methylpyrrolidinium bis(trifluoromethylsulfonyl)-imide ($[C_4mpyrr][NTf_2]$) has been discussed, allowing determination of a range of fundamental kinetic and thermodynamic properties.[27-30] These metals are of particular interest with regards to energy storage devices such as batteries, and our work highlighted strong similarity in the trends within the Alkali metal group between $[C_4mpyrr][NTf_2]$ and the common battery electrolyte propylene carbonate. The tendency of these metals to form dendritic electrodeposits is of both interest and concern, as it can result in harmful short-circuiting of battery devices.[31]

In this Chapter we discuss for the first time *in situ* potassium electrodeposition-XPS measurements in an ionic liquid, achieved with a unique cell design which allowed real time measurement of potassium metal electrodeposition from $[C_4mpyrr][NTf_2]$ in *vacuo*.

7.2 Results and Discussion

7.2.1 Experimental set-up

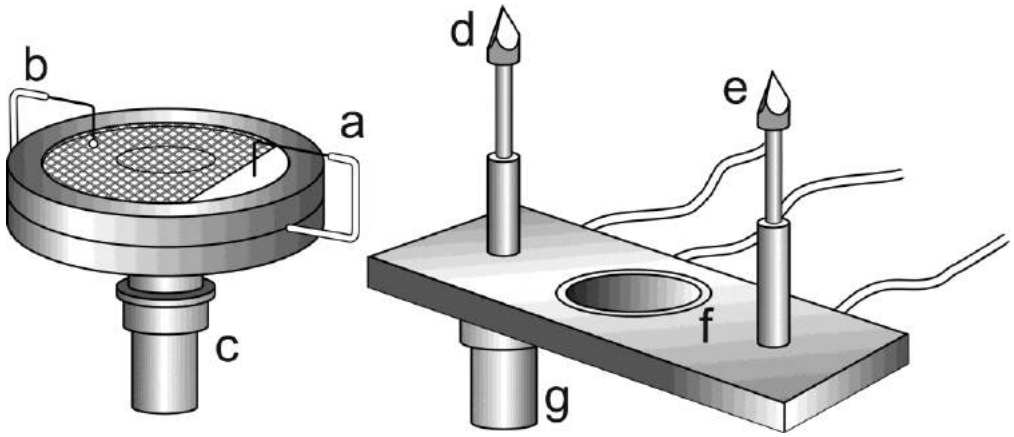

Figure 7. 1: *In situ* XPS-electrochemical cell and associated holder

A custom electrochemistry-XPS cell and cell holder were fabricated in house with the aid of Mr. C. Jones, and are depicted in Figure 7. 1. The cell consisted of two hollow cylinders of PEEK, as well as a modified stainless steel XPS stub. These pieces were precisely machined and then firmly pressed together. A shallow well *ca.* 1 mm deep was made across the surface of the top cylinder of PEEK, and the hollow cylinder and shallow well filled with IL (*ca.* 150 μl). Two pieces of copper foil were sandwiched between the two cylinders of PEEK, and two tapered holes drilled into the bottom cylinder of PEEK. One piece of foil was joined to a Pt wire, which was brought into contact with the IL to act as a *quasi*-reference electrode (depicted as 'a' in Figure 1). The second piece of foil was joined to a Ni mesh via a Pt wire to act as working electrode (b). This mesh was allowed to float on the surface of the IL, forming a three-phase boundary between the IL, Ni and vacuum. The stainless steel stub (c) was used as counter electrode. A removable lid was fashioned to prevent loss of the IL during its

vigorous bubbling when initially *in vacuo*. Electrical connection from the potentiostat to the cell was provided by a removable cell holder. This cell holder was moved around and anchored in place in a traditional cell holder by a modified XPS stub on the underside (g), allowing electrochemical measurements to be performed in addition to traditional samples. The cell was lowered from above onto two pogo spring pins (d and e), which entered the tapered holes and made electrical contact with the working and reference electrodes, respectively, via the copper foil. Much of the counter electrode (c) passed through a hole in the holder before coming to rest on a copper o-ring set in the holder (f). Three shielded wires (from d, e and f) ran from the holder to the potentiostat, via an electrical feed-through in the XPS housing.

7.2.2 XPS Measurements

XPS spectra of the electrochemical set-up was recorded, and Figure 7. 2 displays a wide scan for both 0.1 M and 0.5 M K[NTf_2] dissolved in [C_4mpyrr][NTf_2]. Clear signals were observed for the IL, corresponding to C, N, O, F and S. The stoichiometric ratios agreed well (within *ca.* 5 %) of those expected for the pure IL. Signals for K 2p and K 2s at 295 and 377 eV were not observed for solutions containing 0.1 M K[NTf_2], but could be observed for 0.5 M K[NTf_2].

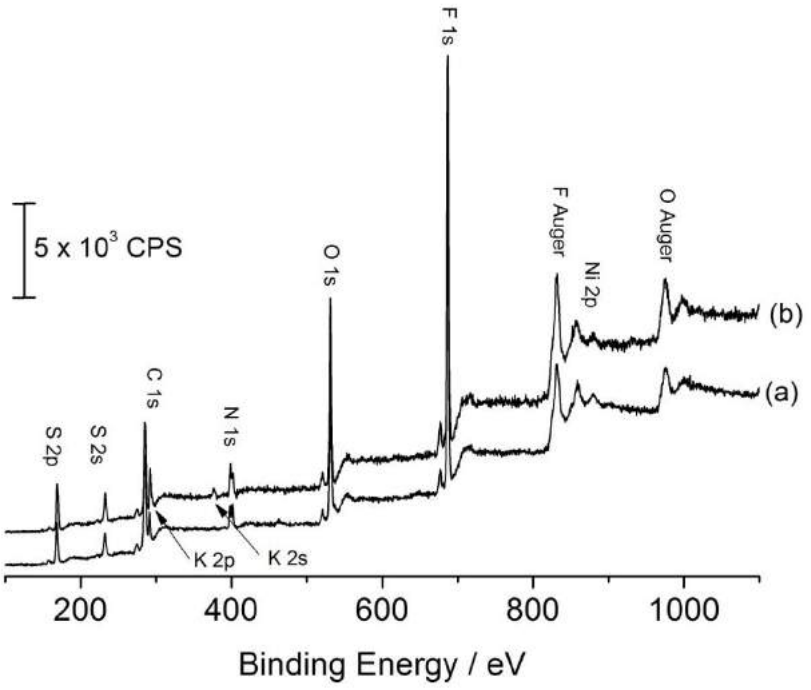

Figure 7. 2: X-ray photoelectron spectra recorded for the *in situ* electrochemistry-XPS cell when filled with (a) 0.1 M K[NTf_2] and (b) 0.5 M K[NTf_2] in [C_4mpyrr][NTf_2].

In both spectra only weak signals were observed for Ni 2p at 855 eV, despite the presence of a significant quantity of Ni in the form of the Ni mesh. The weak signal was found to be related to the angle of the sample with respect to the detector. The sample was kept horizontal when the cell contained IL, with a corresponding take off angle of 75°. This resulted in strong signals for the surface of the IL, but could only detect the top surface of the Ni mesh, emission from the side of the Ni mesh being largely unable to reach the detector. Tilting the sample to change the take off angle to 90° (*e.g.* with the mesh adhered to a carbon tab) resulted in a significant increase in the Ni signal. However, measurement at this angle was not possible when IL was present in the cell, and it is also noted that analysis of the Ni mesh was not required, interest instead being focussed on the surface of the IL in the vicinity of the Ni mesh.

7.2.3 Cyclic voltammetry performed in the XPS chamber

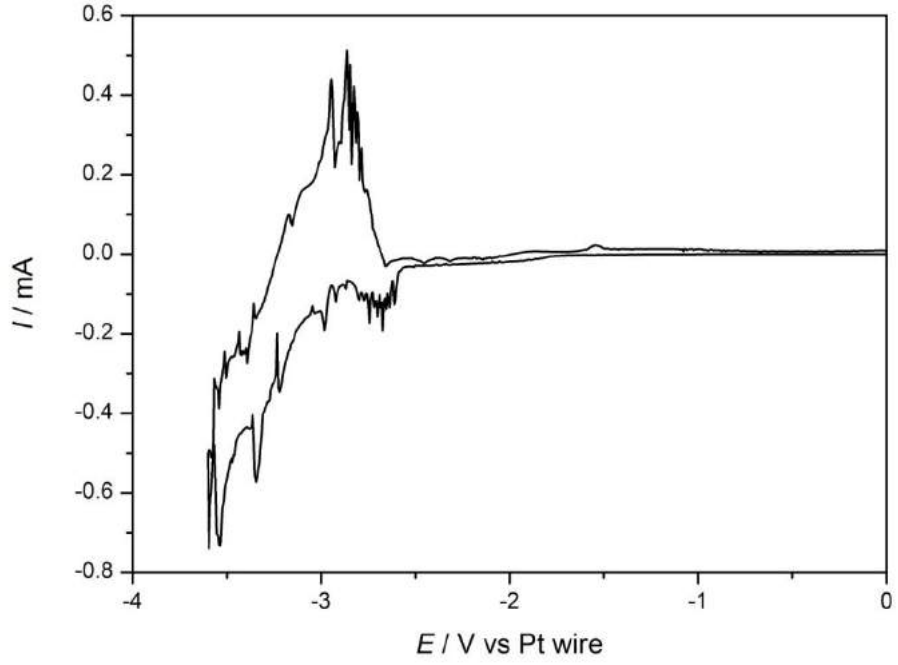

Figure 7. 3: Cyclic voltammogram recorded for 0.5 M K[NTf_2] in [C_4mpyrr][NTf_2] at a Ni mesh electrode inside the XPS chamber. Scan rate = 10 mV s^{-1}.

Figure 7. **3** displays cyclic voltammetry recorded for 0.5 M K[NTf_2] in [C_4mpyrr][NTf_2] in the *in situ* electrochemical-XPS cell, scanning at 10 mV s^{-1} between 0 and -3.6 V *versus* Pt wire. The observed response bears strong resemblance to the previously reported data recorded under similar conditions at a Ni microdisk electrode,[27] namely K underpotential deposition features occurring in the region of *ca.* -1.5 to -2.5 V with bulk electrodeposition of K metal from *ca.* -3.0 V onwards. Stripping of the bulk metal deposit is observed on the reverse scan. Stripping efficiency was less that 100 % on the Ni mesh (*ca.* 33 % efficiency in Figure 7. 3), which has been previous noted for K on Ni microdisk electrodes,[27] as well as for a range of other metals on a range of substrates.[32] If this low stripping efficiency was due to reaction of K metal with trace impurities present in the IL, stripping efficiency would decrease as the concentration of

$K[NTf_2]$ decreased (due to a higher ratio of possible reactants to K electrodeposited). However, experiments at a Ni microdisk electrode demonstrated that a maximum stripping efficiency was observed at *ca.* 0.1 M $K[NTf_2]$ and stripping efficiency decreased with increasing $K[NTf_2]$ concentration, therefore this trend can tentatively be assigned to dendritic metal deposits forming. During oxidation the material in contact with the electrode is oxidised first, and the remainder loses good electrical contact with the electrode resulting in less than 100 % stripping efficiency.[32]

7.2.4 *In situ* electrodeposition-XPS measurements

Electrodeposition of K metal at the Ni mesh was performed by holding the potential at -3.2 V *vs.* the Pt wire *quasi*-reference. XPS measurements were performed periodically, both in wide scan mode and by performing detailed scans in the K 2s region; attention was focussed on the K 2s region as the K 2p partially overlapped with the C 1s signal from the $[NTf_2]^-$ anion.

For the first *ca.* 12 hours, the K 2s region was essentially featureless (Figure 7. 4), although with extended electrolysis time (up to 36 hrs) increasing quantities of K were detected at the surface of the IL, corresponding to electrodeposited K metal. From 15 hrs onwards the quantity of K detected was found to be in an approximately linear manner with time (Figure 7. 5).

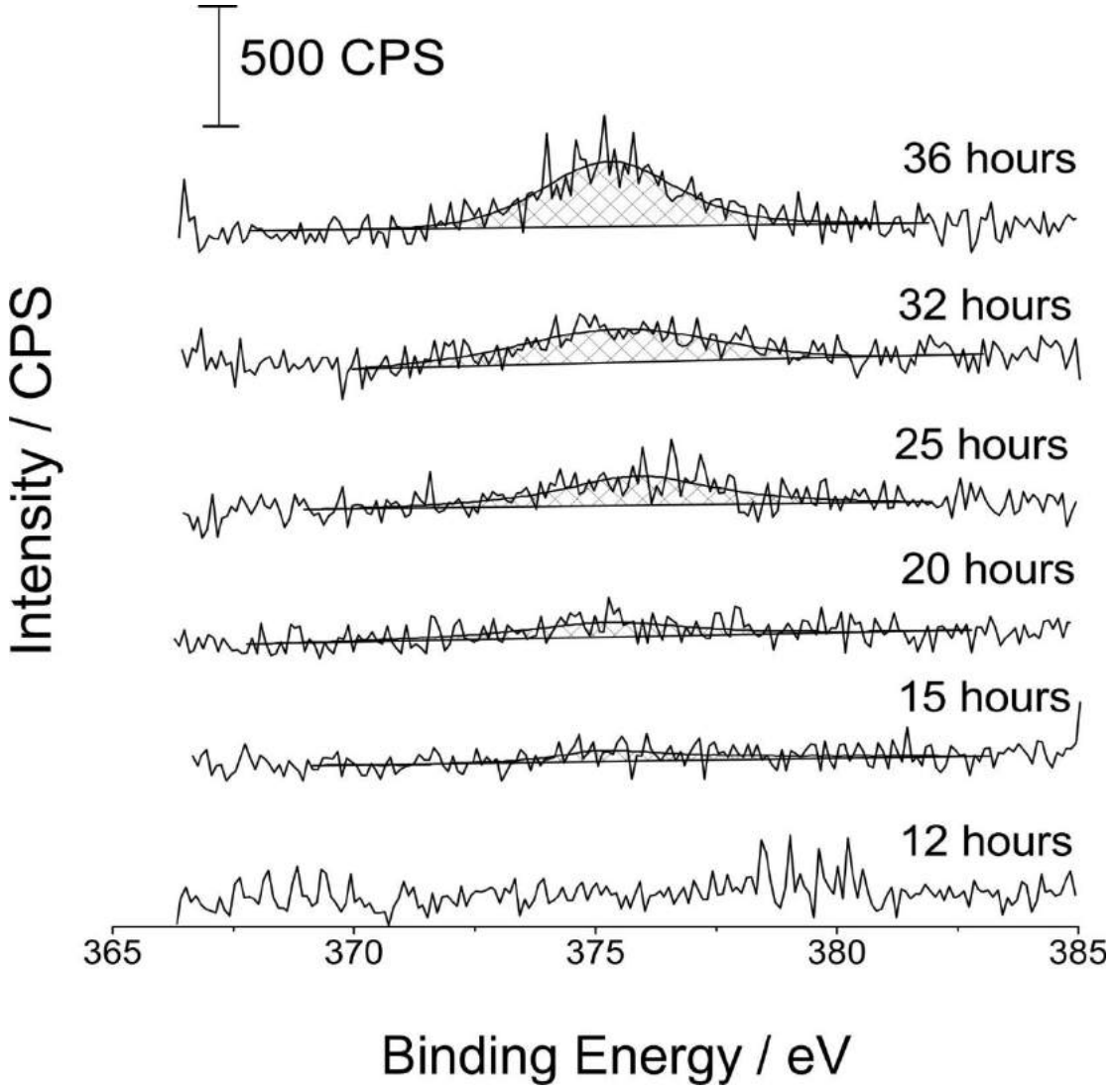

Figure 7. 4: XPS high resolution scans (pass energy of 20 eV, 10 scans) for the K 2s region taken during electrolysis at -3.2 V *vs.* Pt *quasi*-reference at a Ni mesh electrode floating on 0.1 M K[NTf_2] in [C_4mpyrr][NTf_2]. The scan were recorded after 12, 15, 20, 25, 32 and 36 hours of electolysis.

The preceding 15 hrs appeared to correspond to an induction period, likely corresponding to the formation of K electrodeposits growing on and close to the Ni surface which due to the take off angle could not be detected. After 36 hrs a total charge of 4.5 C was passed, corresponding to approximately 2 mg of K metal deposited (assuming 100 % columbic efficiency). An electrolysis extending 36 hrs is expected when dealing with IL systems, due to the relatively high viscosity and low diffusion coefficients typically experienced in IL systems. For example, the diffusion coefficient

of K^+ in [C_4mpyrr][NTf_2] (D = 1.02 x 10^{-11} m^2 s^{-1})[27] is two orders of magnitude slower than that observed in aqueous media (D = *ca.* 3 x 10^{-9} m^2 s^{-1}).[33]

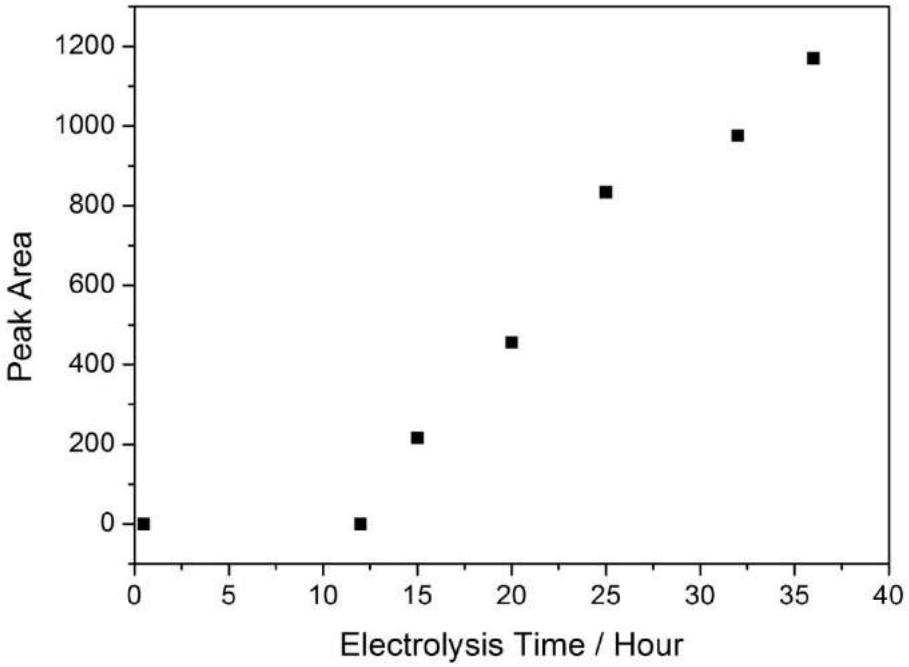

Figure 7. 5: Plot of the absolute XPS peak area recorded under the K 2s peak as a function of electrolysis time

After 36 hrs the electrolysis was ceased and all connections running from the potentiostat to the XPS unplugged. The system was allowed to remain like that for 1 hr before another XPS measurement recorded. The measurement demonstrated no significant change in the various peaks relative to that recorded before electrolysis was ceased, showing that the system was stable for this period. After this the cell was reconnected, and the K deposit oxidised at an applied potential of 0 V *vs.* Pt wire *quasi*-reference for 30 min. Figure 6 displays the XPS spectra recorded (a) after holding -3.2 V for 36 hrs and (b) after the subsequent application of 0 V for 30 min. There is clearly a significant decrease in the size of the K peak, corresponding to oxidation of K (in contact with the Ni) to K^+, with much of the resulting K^+, as well as K metal no longer adhered to the Ni surface diffusing away.

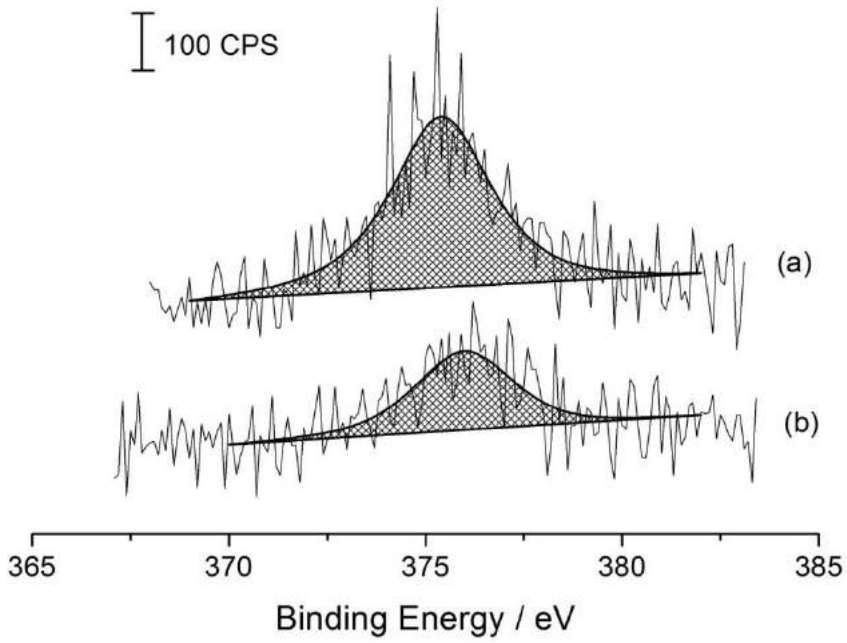

Figure 7. 6: XPS high resolution scan for K 2s taken (a) after 36 hours of electrodeposition at -3.2 V and (b) after the oxidation of the deposit for 30 min at 0 V.

7.2.5 Is it possible to distinguish between potassium metal and potassium ions?

During this work, it was observed that when the electrochemical cell was polarised between applied potentials of -2.0 V to +0.5 V *vs.* Pt *quasi*-reference (no Faradaic current passed), the binding energy of all elements shifted by -0.82 eV V^{-1} (R^2 = 0.99 for linear fit, n = 5) implying minor distortion of the IL-vacuum interface due to the polarised Ni mesh. This shift is distinct from the recently highlighted -1.0 eV V^{-1} 'electrochemical shift' experienced by IL molecules in the electrochemical double layer,[26] as our focus was extended over an area considerably larger than the double layer. However, this was accounted for by referencing all spectra to the ionic liquid C 1s peak.

It is feasible to distinguish between K^+ ions and K bulk metal using XPS as they possess distinct binding energies, *e.g.* 1.2 eV difference for the K $2p_{3/2}$ peaks, respectively.[34] However, at the start of electrolysis the K^+ ions XPS peak could not be observed. During electrolysis a potassium peak developed in the XPS spectra, although the precise binding energy determined by fitting of the peak was found to shift by up to 0.8 eV. This was largely a feature of instrumental noise resulting in some ambiguity regarding the precise position of the peak. Additionally, Villar-Garcia *et al.* have recently highlighted that the charging of the ionic liquid surfaces during X-ray irradiation, as well as day-to-day variations can lead to binding energy values shifting by at least 0.8 eV unless internal referencing to unaffected moieties is performed (*e.g.* long-chain aliphatic carbon peaks),[23] which was not possible in this current work. Therefore given the minor uncertainties present, elements can be accurately identified and quantified but detailed speciation information (such as differentiation between K and K^+) cannot be accurately assigned to the system.

7.3. Conclusions

A novel cell design designed for application in conventional XPS chambers has been presented. Using this design it has been clearly been demonstrated that the growth of (reactive) metal deposits can be monitored at the three-phase ionic liquid-electrode-vacuum boundary using in situ XPS measurements. Next Chapter, we discuss the extension of this work for monitoring rubidium electrodeposition in competition with the ionic liquid breakdown.

References

(1) Wibowo, R.; Aldous, L.; Jacobs, R. M. J.; Manan, N. S. A.; Compton, R. G. *Chem Phys Lett* **2011**, *509*, 72-76.

(2) Esperanca, J. M. S. S.; Lopes, J. N. C.; Tariq, M.; Santos, L. M. N. B. F.; Magee, J. W.; Rebelo, L. P. N. *J Chem Eng Data* **2010**, *55*, 3-12.

(3) Endres, F. P. D.; MacFarlane, D.; Abbott, A. *Electrodeposition from ionic liquids*; Wiley-VCH: Weinheim ; Chichester, 2008.

(4) Smith, E. F.; Rutten, F. J. M.; Villar-Garcia, I. J.; Briggs, D.; Licence, P. *Langmuir* **2006**, *22*, 9386-9392.

(5) Kuwabata, S.; Tsuda, T.; Torimoto, T. *J Phys Chem Lett* **2010**, *1*, 3177-3188.

(6) Bernardi, F.; Scholten, J. D.; Fecher, G. H.; Dupont, J.; Morais, J. *Chem Phys Lett* **2009**, *479*, 113-116.

(7) Chang, J. K.; Lee, M. T.; Tsai, W. T.; Deng, M. J.; Cheng, H. F.; Sun, I. W. *Langmuir* **2009**, *25*, 11955-11960.

(8) Chang, J. K.; Lee, M. T.; Tsai, W. T.; Deng, M. J.; Sun, I. W. *Chem Mater* **2009**, *21*, 2688-2695.

(9) Cremer, T.; Kolbeck, C.; Lovelock, K. R. J.; Paape, N.; Wolfel, R.; Schulz, P. S.; Wasserscheid, P.; Weber, H.; Thar, J.; Kirchner, B.; Maier, F.; Steinruck, H. P. *Chem-Eur J* **2010**, *16*, 9018-9033.

(10) Foelske-Schmitz, A.; Weingarth, D.; Kaiser, H.; Kotz, R. *Electrochem Commun* **2010**, *12*, 1453-1456.

(11) Fortunato, R.; Afonso, C. A. M.; Benavente, J.; Rodriguez-Castellon, E.; Crespo, J. G. *J Membrane Sci* **2005**, *256*, 216-223.

(12) Gottfried, J. M.; Maier, F.; Rossa, J.; Gerhard, D.; Schulz, P. S.; Wasserscheid, P.; Steinruck, H. P. *Z Phys Chem* **2006**, *220*, 1439-1453.

(13) Hashimoto, H.; Ohno, A.; Nakajima, K.; Suzuki, M.; Tsuji, H.; Kimura, K. *Surf Sci* **2010**, *604*, 464-469.

(14) Hofft, O.; Bahr, S.; Himmerlich, M.; Krischok, S.; Schaefer, J. A.; Kempter, V. *Langmuir* **2006**, *22*, 7120-7123.

(15) Krischok, S.; Eremtchenko, M.; Himmerlich, M.; Lorenz, P.; Uhlig, J.; Neumann, A.; Ottking, R.; Beenken, W. J. D.; Hofft, O.; Bahr, S.; Kempter, V.; Schaefer, J. A. *J Phys Chem B* **2007**, *111*, 4801-4806.

(16) Kwon, J. H.; Youn, S. W.; Kang, Y. C. *B Kor Chem Soc* **2006**, *27*, 1851-1853.
(17) Lockett, V.; Sedev, R.; Bassell, C.; Ralston, J. *Phys Chem Chem Phys* **2008**, *10*, 1330-1335.

(18) Lovelock, K. R. J.; Villar-Garcia, I. J.; Maier, F.; Steinruck, H. P.; Licence, P. *Chem Rev* **2010**, *110*, 5158-5190.

(19) Maier, F.; Gottfried, J. M.; Rossa, J.; Gerhard, D.; Schulz, P. S.; Schwieger, W.; Wasserscheid, P.; Steinruck, H. P. *Angew Chem Int Edit* **2006**, *45*, 7778-7780.

(20) Shigeyasu, M.; Murayama, H.; Tanaka, H. *Chem Phys Lett* **2008**, *463*, 373-377.

(21) Silvester, D. S.; Broder, T. L.; Aldous, L.; Hardacre, C.; Crossley, A.; Compton, R. G. *Analyst* **2007**, *132*, 196-198.

(22) Smith, E. F.; Villar Garcia, I. J.; Briggs, D.; Licence, P. *Chem Commun* **2005**, 5633-5635.

(23) Villar-Garcia, I. J.; Smith, E. F.; Taylor, A. W.; Qiu, F. L.; Lovelock, K. R. J.; Jones, R. G.; Licence, P. *Phys Chem Chem Phys* **2011**, *13*, 2797-2808.

(24) Qiu, F. L.; Taylor, A. W.; Men, S.; Villar-Garcia, I. J.; Licence, P. *Phys Chem Chem Phys* **2010**, *12*, 1982-1990.

(25) Taylor, A. W.; Qiu, F. L.; Villar-Garcia, I. J.; Licence, P. *Chem Commun* **2009**, 5817-5819.

(26) Weingarth, D.; Foelske-Schmitz, A.; Wokaun, A.; Kötz, R. *Electrochem Commun* **2011**, doi:10.1016/j.elecom.2011.03.027.

(27) Wibowo, R.; Aldous, L.; Jones, S. E. W.; Compton, R. G. *Chem Phys Lett* **2010**, *492*, 276-280.

(28) Wibowo, R.; Aldous, L.; Rogers, E. I.; Jones, S. E. W.; Compton, R. G. *J Phys Chem C* **2010**, *114*, 3618-3626.

(29) Wibowo, R.; Jones, S. E. W.; Compton, R. G. *J Chem Eng Data* **2010**, *55*, 1374-1376.

(30) Wibowo, R.; Jones, S. E. W.; Compton, R. G. *J Phys Chem B* **2009**, *113*, 12293-12298.

(31) Park, H. E.; Hong, C. H.; Yoon, W. Y. *J Power Sources* **2008**, *178*, 765-768.

(32) Hyde, M. E.; Banks, C. E.; Compton, R. G. *Electroanal* **2004**, *16*, 345-354.

(33) Lee, S. H.; Rasaiah, J. C. *J Phys Chem-Us* **1996**, *100*, 1420-1425.

(34) Li, S.; Kang, E. T.; Neoh, K. G.; Ma, Z. H.; Tan, K. L.; Huang, W. *Appl Surf Sci* **2001**, *181*, 201-210.

Chapter 8

In situ Electrochemical-X-Ray Photoelectron Spectroscopy: Rubidium Metal Deposition from an Ionic Liquid in Competition with Solvent Breakdown

Having been successfully demonstrated monitoring potassium electrodeposition from an ionic liquid by using *in situ* electrochemical-X-ray Photoelectron Spectroscopy (XPS) as described in Chapter 7, the experiments are now extended for another Group I metal using the same approach. This Chapter discusses the electrodeposition of rubidium from an ionic liquid (IL) *N*-butyl-*N*-methylpyrrolidium bis(trifluoromethylsulfonyl)imide ($[C_4mpyrr][NTf_2]$) performed and monitored at a Nickel mesh electrode by using *in situ* electrochemical-X-ray Photoelectron Spectroscopy (XPS) measurements. At extremely high current values during the deposition of the metal, XPS signals revealing the solvent breakdown were also observed. By choosing suitable low current values, electrodeposition of Rb can occur without IL degradation. IL degradation was characterised by carbonisation of the electrode-IL-vacuum interface, with the loss of fluorine being relatively pronounced, consistent with reduction of the $[NTf_2]^-$ anion.

The work presented in this chapter has been submitted to *Chemical Physics Letters*.

8.1 Introduction

Rubidium is one of the Group I alkali metals, which are characteristically strong reducing agents. The formal potential (E_f^0) of the Rb/Rb^+ couple in aqueous solution is -2.94 V (*vs.* SHE)[1], while the E_f^0 for Rb/Rb^+ in the ionic liquid $[C_4mPyrr][NTf_2]$ has recently been measured as -3.37 V (*vs.* Fc/Fc^+)[2]. This property makes Rb a potential candidate for use in solid batteries[3] as well as energy storage devices[4]. Rubidium cannot be electrodeposited from aqueous solution or many organic solvents as their potential windows are not wide enough.

Room temperature ionic liquids (RTILs or ILs), which are typically comprised entirely of ions, are promising media for the deposition for active metals such as Rubidium.[2,5] Their intrinsic ionic conductivity, chemical stability as well as wide electrochemical windows makes the electrodeposition of many active metals possible.[6] Moreover, another important property of ILs is that they possess near zero vapour pressure. The combination of these properties has facilitated novel spectroelectrochemical techniques under high vacuum conditions, including *in situ* electrochemical-X-ray spectroscopy. A number of publications are available regarding the use of *in situ* electrochemical-XPS measurements in conjunction with ILs, probing the oxidation of Cu to Cu(I)[7], reduction of Fe(III) to Fe(II)[8], the intercalation of $[C_2mim][BF_4]$ into HOPG,[9] and the XPS induced charging [10] and electrochemical shift in binding energy [11] of ionic liquids. The diverse range of other (non-electrochemical) studies relating to combined IL-XPS studies has recently been reviewed.[12]

In Chapter 4 to 6, we have discussed the electrodeposition of Group I alkali metals from the ionic liquid *N*-butyl-*N*-methylpyrrolidinium bis(trifluoromethylsulfonyl)imide ([C_4mpyrr][NTf_2]) on Pt and Ni electrodes.[2,13-15] The fundamental kinetic and thermodynamic properties have been determined by means of simulation.[2,13-15] In addition, in Chapter 7 we discussed the *in situ* electrochemical-XPS measurements to monitor the electrodeposition of potassium in the ionic liquid of [C_4mpyrr][NTf_2] using *in situ* electrochemical-XPS measurements.[16] Unlike potassium, rubidium electrodeposition is close to the reductive breakdown of [C_4mpyrr][NTf_2]. In this Chapter, we discuss the use of *in situ* electrochemical-XPS to explore the breakdown of the solvent in competition with the electrodeposition of rubidium.

8.2 Results and Discussion

8.2.1 Experimental set-up

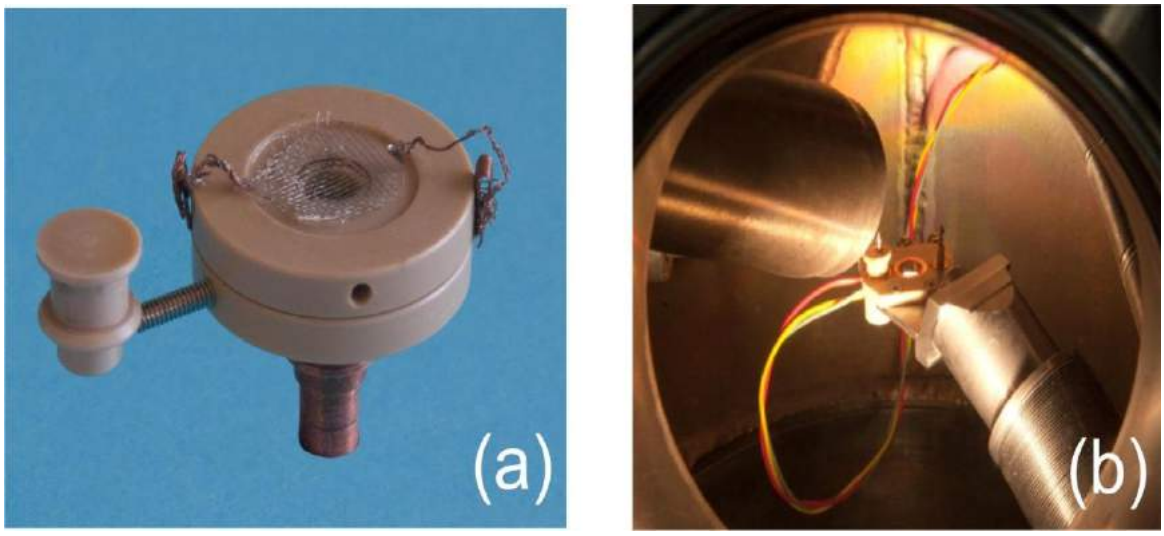

Figure 8. 1 *In situ* electrochemical-XPS cell (a) and associated holder inside the XPS chamber (b).

The *in situ* electrochemical-XPS cell (Figure 8. 1(a)) and holder (Figure 8. 1(b)) used in this study were fabricated in-house and are modifications of the electrochemical setup reported in the previous chapter.[16] Briefly, the cell holder was a previously described

mobile cell holder [16] that had been fixed permanently onto the end of an extendable and retractable manipulator arm which was inserted into the XPS chamber through a high vacuum flange. The sample-holding cell consisted of two parts, namely two hollow cylinders of PEEK with the bottom of one sealed by a modified copper XPS stub, which were manufactured and joined as previously detailed elsewhere.[16] An arm was placed on the side of the cell in order to allow movement of the cell with a standard manipulator arm. The cell was lowered from above onto two pogo spring pins emerging from the holder which entered tapered holes in the cell and made electrical contact with the working and reference electrodes, respectively, via copper foil. Much of the counter electrode passed through a hole in the holder before coming to rest on a copper o-ring set in the holder. Three shielded wires ran from the holder to the potentiostat via an electrical feed-through in the XPS housing. Once the cell was secured on top of the holder, the standard XPS holder was retracted and the entire assembly extended until the sample was in line with the X-ray source.

8.2.2 XPS Spectrum of the ionic liquid

Figure 8. 2 depicts the XPS survey scan of 0.1 M Rb[NTf_2] in [C_4mpyrr][NTf_2] recorded in the XPS-electrochemistry cell but prior to any electrochemical experiments. No Rb signals were observed, although this is easily explained by the relatively dilute nature of the solution (in terms of atomic % values). Signals were observed corresponding to C, N, O, F and S. Analysis of these signals were similar to those expected based upon the stoichiometric ratio for the pure ionic liquid (deviation less than 5%), using the widely available and frequently used standard atomic sensitivity

factors by Wagner *et al.*[17] Minor differences between measured and known atomic ratios during XPS measurements of ILs have been reported before, and have been attributed to system-dependant deviations which require the development of system-specific atomic sensitivity factors using 'ultrapure' ILs.[12,18] In this work the sensitivity factors of Wagner *et al.*[17] were found to provide a sufficient degree of accuracy. No impurities were detected in the [C_4mpyrr][NTf_2], either by XPS or cyclic voltammetry.

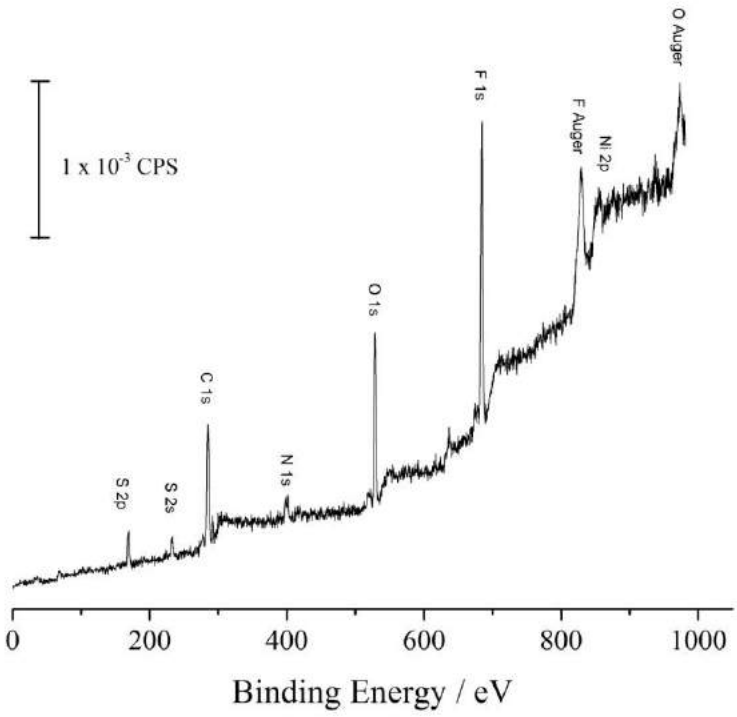

Figure 8. 2 The XPS measurement of [C_4mpyrr][NTf_2] containing 0.1 M Rb[NTf_2] in the *in situ* electrochemistry-XPS cell

Weak signals were also observed corresponding to the Ni mesh electrode (Ni 2p3/2 at 855 eV). This relatively weak signal (compared to the quantity of Ni present) was due to the take-off angle of 75 ° employed on the curved Ni wires of the mesh, *e.g.* if the sample was rotated to give a take-off angle of 90 ° a significantly stronger Ni peak was observed, although measurements could not be performed at this angle when the cell contained a liquid sample.

8.2.3 *In situ* electrodeposition-XPS measurements

Galvanostatic electrolysis was performed by passing a constant current at a Ni mesh electrode in the electrochemistry-XPS cell containing 0.1 M $Rb[NTf_2]$ in $[C_4mpyrr][NTf_2]$.[1] The progress of the electrolysis was monitored periodically by XPS, using both wide survey scans as well as detailed scans in the Rb 3d region.

Figure 8. 3 displays the survey scans recorded before and during electrolysis at a fixed current of -5 x 10^{-4} A. It can be clearly observed that after 1 h of electrolysis a significant Rb 3d signal was present, due to accumulation of Rb by its electrodeposition at the Ni-IL-vacuum three-phase boundary. The signal increased when the electrolysis was extended to 6 h, indicating increasing quantities of Rb metal. In addition to the growth of the Rb features, it was also observed that the stoichiometric ratio of the constituent IL elements (C, N, O, F and S) gradually changed with the atomic percentage of C increasing from *ca.* 44 % to *ca.* 69 % after 1 h electrolysis, indicating significant carbonisation of the ionic liquid was occurring in conjunction to Rb electrodeposition. After 6 h the N features were also observed to merge to form one single feature, rather than the two features expected for the different N present in the anion and cation.[12] Weingarth have previously monitored the reductive decomposition of $[C_2mim][BF_4]$ at a Pt electrode by XPS, where as an increasingly negative potential was applied a minor N feature (shifted by 2.5 eV relative to the imidazolium N) was observed and was attributed to a decomposition product of the cation.[11]

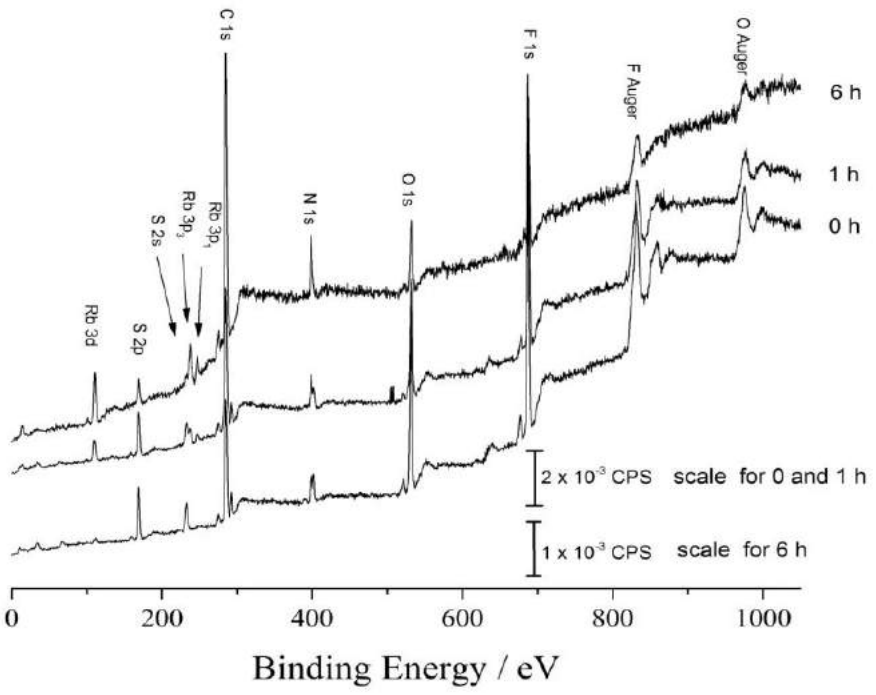

Figure 8. 3 XPS survey scans (pass energy 100 eV, 5 scans) recorded during electrolysis at -5x10^{-4} A at a Ni mesh electrode floating on a [C_4mpyrr][NTf_2] containing 0.1 M Rb[NTf_2]. The scan were recorded after 0, 1 and 6 h of electolysis.

A furthur experiment was performed by decreasing the current by a factor of 50, to -1 x 10^{-5} A. Figure 8. 4 shows detailed scans recorded in the Rb 3d region during electrolysis. From the figure it can clearly be seen that a Rb signal was observed after 1 hour of electrolysis, and that the Rb signal increased as the electrolysis time was extended. The quantity of Rb detected was found to increase in an approximately linear manner with time (Figure 8. 5), and after 26 hour a total of 0.94 C was passed, corresponding to approximately 0.8 mg of Rb metal deposited (assuming 100% columbic efficiency).

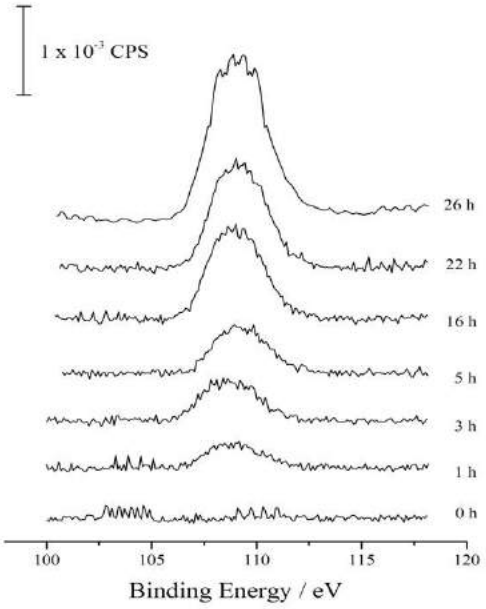

Figure 8. 4 XPS high resolution scans (pass energy 20 eV, 30 scans) for the Rb 3d region taken during electrolysis at -1x10^{-5} A at a Ni mesh electrode floating on [C_4mpyrr][NTf_2] containing 0.1 M Rb[NTf_2]. The scan were recorded after 1, 3, 5, 16, 22 and 26 h of electolysis.

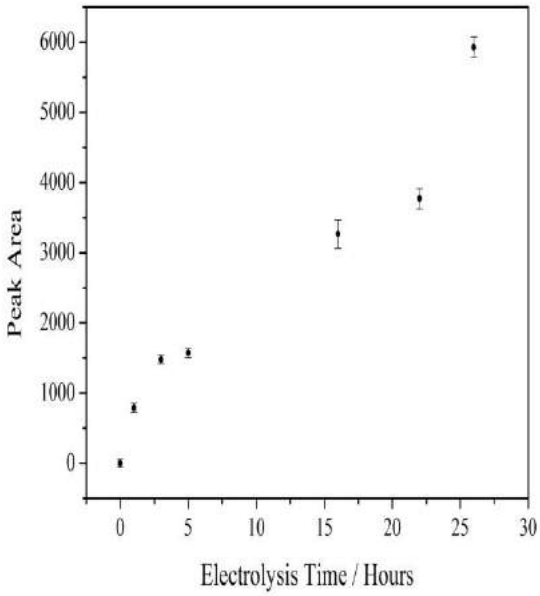

Figure 8. 5 Plot of Rb peak area detected at the Ni-IL-vacuum interface as a function of electrolysis time, as measured by XPS.

After 26 hrs the electrolysis was ceased and all connections running from the potentiostat to the XPS unplugged. The system was allowed to remain like that for 1 h before another XPS measurement recorded. There were no significant differences before and after the system was allowed to rest for 1 h, indicating that the Rb electrodeposit was stable. After this the cell was reconnected, and the Rb deposit oxidised at an applied potential of 0 V *vs.* Pt wire *quasi*-reference for 30 min. Figure 8. 6 displays the detailed XPS scans for Rb 3d taken (a) after 26 hours of electrodeposition and (b) after the subsequent application of 0 V for 30 min. The decrease in the size of the Rb peak corresponds to the oxidation of Rb to Rb[NTf_2], some of which diffused away on the timescale of the oxidation.

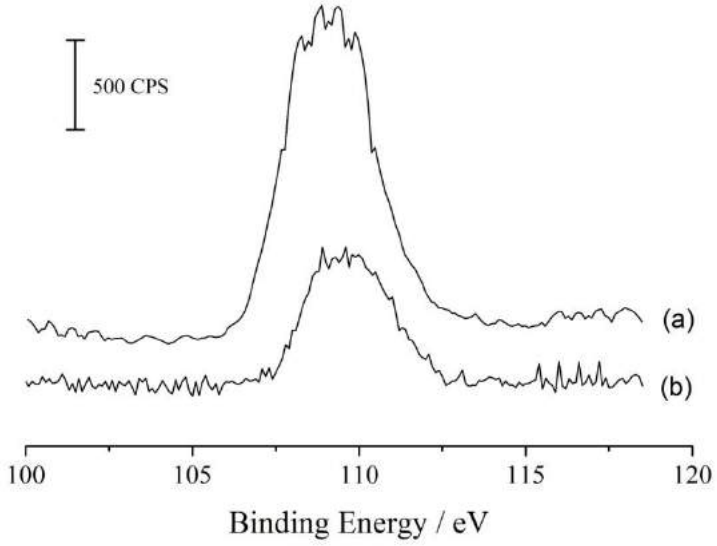

Figure 8. 6 XPS high resolution scans for Rb 3d recorded (a) after 26 hours of electrodeposition and (b) after oxidation of the deposit for 30 min at 0 V.

Detailed analysis of the composition of the IL at the Ni-IL-vacuum interface was performed by examining the IL signals from a range of survey scans (Figure 8. 7). The corresponding atomic % of each IL element obtained from the survey scans as a function of electrolysis time has been displayed in Figure 8. 8, as well as solid lines representing the expected values for the IL based upon stoichiometric calculations. Minor discrepancies between measured and expected elemental compositions at short times are associated with non-optimised atomic sensitivity factors, as described by Kolbeck *et al.*[19] The IL composition was observed to stay essentially constant within the first three hours of electrolysis. However, from 5 hours onwards deviation consistent with the carbonisation of the ionic liquid was observed, likely due to the exhaustion of Rb^+ near the electrode surface after extended electrolysis. The C signal was observed in increase from *ca.* 44 % to *ca.* 58 % over 22 h, while the N signal was

observed to remain constant, S and O decreased slightly and the F signal decreased significantly.

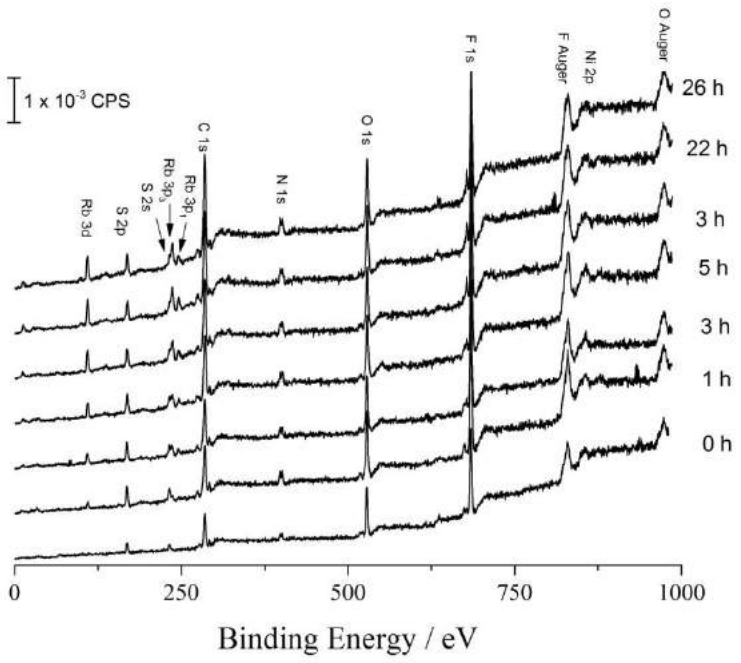

Figure 8. 7 XPS survey scans (pass energy 100 eV, 5 scans) recorded during electrolysis at -1x10^{-5} A at a Ni mesh electrode floating on [C_4mpyrr][NTf_2] containing 0.1 M Rb[NTf_2]. The scans were recorded after 0, 1, 3, 5, 16, 22 and 26 h of electolysis.

This could be consistent with the reduction of the pyrrolidinium cation at the Ni electrode (likely through cleavage of an N-C bond to form methylpyrrolidine and a butyl radical or ring opening to a dibutylmethylamine radical, based upon quantum chemical calculations,[20] followed by subsequent reduction and/or polymerisation of the reduced tertiary amine), and concurrent lost of the $[NTf_2]^-$ anion at the counter electrode. Alternatively, findings by other researchers have pointed towards the possibility of electrochemical reduction of the $[NTf_2]^-$ anion,[21-23] with the major gaseous product having been identified as trifluoromethane.[22] The reductive loss of

trifluoromethane appears to agree with the XPS monitored degradation of the $[C_4mpyrr][NTf_2]$, namely the rapid loss of F in comparison with the other elements.

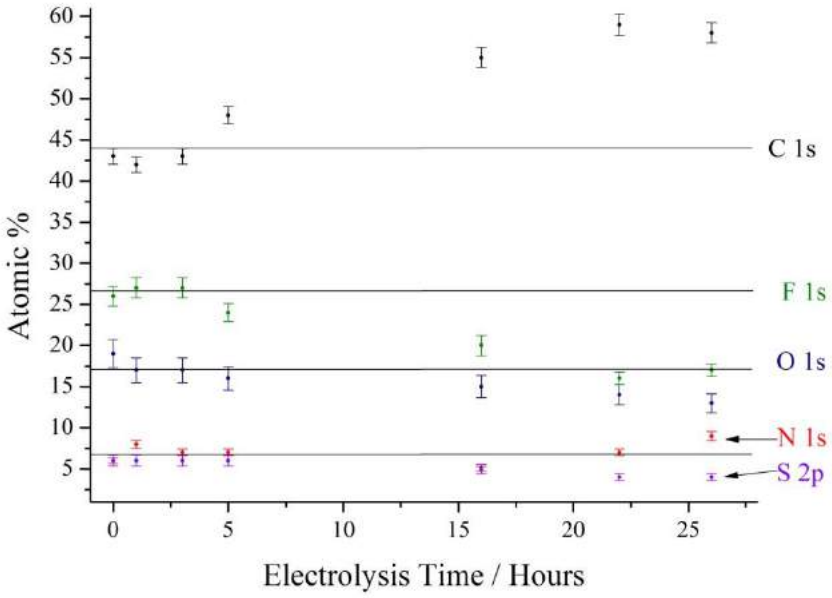

Figure 8. 8 The atomic percentages of C, N, O, F and S calculated from the XPS high resolution scan (excluding Rb and Ni signals) recorded during electrolysis at $-1x10^{-5}$ A. The solid line represents the theoretical value of the atomic percentage. Error bars are associated with the peak fitting and instrumental error.

8.3 Conclusions

The electrodeposition of rubidium has been performed by *in situ* electrodeposition-XPS employing a novel cell design. The *in situ* electrochemical-XPS technique allows monitoring of the progress of Rb electrodeposition as well as the competing decomposition of the ionic liquid during the electrodeposition. Passing a high cathodic current for the electrodeposition resulted in rapid decomposition of the ionic liquid in addition to Rb electrodeposition. On the other hand, lowering the current for electrodeposition slows down the decomposition during the electrodeposition process.

References

(1) Marcus, Y. *Pure And Applied Chemistry* **1985**, *57*, 1129-1132.

(2) Wibowo, R.; Aldous, L.; Jones, S. E. W.; Compton, R. G. *Chemical Physics Letters* **2010**, *492*, 276-280.

(3) Pawar, D. V.; Magdum, T. S.; Rasal, S. P.; Chavan, S. H. *Bulletin of Electrochemistry* **1995**, *11*, 294-296.

(4) Angelino, G.; Invernizzi, C. *Solar Energy* **2008**, *82*, 637-647.

(5) Endres, F. P. D.; MacFarlane, D.; Abbott, A. *Electrodeposition from ionic liquids*; Wiley-VCH: Weinheim ; Chichester, 2008.

(6) El Abedin, S. Z.; Endres, F. *Chemphyschem* **2006**, *7*, 58-61.

(7) Qiu, F. L.; Taylor, A. W.; Men, S.; Villar-Garcia, I. J.; Licence, P. *Physical Chemistry Chemical Physics* **2010**, *12*, 1982-1990.

(8) Taylor, A. W.; Qiu, F. L.; Villar-Garcia, I. J.; Licence, P. *Chemical Communications* **2009**, 5817-5819.

(9) Foelske-Schmitz, A.; Weingarth, D.; Kaiser, H.; Kotz, R. *Electrochemistry Communications* **2010**, *12*, 1453-1456.

(10) Villar-Garcia, I. J.; Smith, E. F.; Taylor, A. W.; Qiu, F. L.; Lovelock, K. R. J.; Jones, R. G.; Licence, P. *Physical Chemistry Chemical Physics* **2011**, *13*, 2797-2808.

(11) Weingarth, D.; Foelske-Schmitz, A.; Wokaun, A.; Kotz, R. *Electrochemistry Communications* **2011**, *13*, 619-622.

(12) Lovelock, K. R. J.; Villar-Garcia, I. J.; Maier, F.; Steinruck, H. P.; Licence, P. *Chemical Reviews* **2010**, *110*, 5158-5190.

(13) Wibowo, R.; Aldous, L.; Rogers, E. I.; Jones, S. E. W.; Compton, R. G. *Journal of Physical Chemistry C* **2010**, *114*, 3618-3626.

(14) Wibowo, R.; Jones, S. E. W.; Compton, R. G. *Journal of Physical Chemistry B* **2009**, *113*, 12293-12298.

(15) Wibowo, R.; Jones, S. E. W.; Compton, R. G. *Journal of Chemical and Engineering Data* **2010**, *55*, 1374-1376.

(16) Wibowo, R.; Aldous, L.; Jacobs, R. M. J.; Manan, N. S. A.; Compton, R. G. *Chemical Physics Letters* **2011**, *509*, 72-76.

(17) Wagner, C. D.; Davis, L. E.; Zeller, M. V.; Taylor, J. A.; Raymond, R. H.; Gale, L. H. *Surface and Interface Analysis* **1981**, *3*, 211-225.

(18) Maier, F.; Gottfried, J. M.; Rossa, J.; Gerhard, D.; Schulz, P. S.; Schwieger, W.; Wasserscheid, P.; Steinruck, H. P. *Angewandte Chemie-International Edition* **2006**, *45*, 7778-7780.

(19) Kolbeck, C.; Killian, M.; Maier, F.; Paape, N.; Wasserscheid, P.; Steinruck, H. P. *Langmuir* **2008**, *24*, 9500-9507.

(20) Kroon, M. C.; Buijs, W.; Peters, C. J.; Witkamp, G. J. *Green Chemistry* **2006**, *8*, 241-245.

(21) Howlett, P. C.; Izgorodina, E. I.; Forsyth, M.; MacFarlane, D. R *Zeitschrift Fur Physikalische Chemie-International Journal of Research in Physical Chemistry & Chemical Physics* **2006**, *220*, 1483-1498.

(22) Markevich, E.; Sharabi, R.; Borgel, V.; Gottlieb, H.; Salitra, G.; Aurbach, D.; Semrau, G.; Schmidt, M. A. *Electrochimica Acta* **2010**, *55*, 2687-2696.

(23) Ong, S. P.; Andreussi, O.; Wu, Y. B.; Marzari, N.; Ceder, G. *Chem.Mat.* **2011**, *23*, 2979-2986.

Chapter 9

Overall Conclusions

The work in this thesis has generated fundamental understanding of the electrodeposition of Alkali Group I metals from room temperature ionic liquids. RTILs that have a wide enough potential window as well as electrochemical stability have been shown to support the deposition and stripping of the metals. Experimental data have been simulated using a computer programme developed by the Group allowing fundamental kinetics and thermodynamic parameters such as the electrochemical rate constant (k^0), diffusion coefficient (D), formal potential (E_f^0) and transfer coefficient (α) to be extracted. This has lead to deducing the trend in the electrode potential down the Group in one RTIL solvent; this information that is valuable in respect of energy storage as well as in battery application. Specifically, the trend in electrode potentials for Alkali Group I metals (excluding Fransium due to its reactivity) in the ionic liquid [C_4mpyrr][NTf_2] is similar to that in propylene carbonate which is commonly used as an electrolyte in batteries.

In addition, the near zero vapour pressure property of this group of solvent has been exploited to enable the development of a novel spectroelectrochemical technique noatably *in situ* electrochemical-X-ray photoelectron spectroscopy; a powerful technique that can be applied to monitor the electrodeposition of metals in real time. *In situ* electrochemical-XPS also shows the ability to observe changes in the chemical composition of the solvent during the electrodeposition process among from decomposition of the RTIL.